

FREIE UNIVERSITÄT BERLIN

Migration Patterns of Injection- and
Postinjection-Induced Seismicity:
Applications to Local and Regional Scales

Dissertation
zur Erlangung des akademischen Grades
Doktor der Naturwissenschaften

Fachbereich Geowissenschaften
Freie Universität Berlin

Vorgelegt von:
Lisa Johann

September 2020

Ich erkläre hiermit an Eides statt, dass ich die vorliegende Dissertation selbstständig und nur unter Verwendung der angegebenen Quellen und Hilfsmittel angefertigt habe.

Berlin, 22. September 2020

Erstgutachter: Prof. Dr. Serge A. Shapiro
Zweitgutachter: Prof. Dr. Marco Bohnhoff

Tag der Disputation: 7. Dezember 2020

"Just living is not enough," said the butterfly, "one must have sunshine, freedom and a little flower."

Hans Christian Andersen

Summary

In many cases, fluid injections into the subsurface have been recognised to cause seismic activity. Understanding the driving physical processes of these man-made earthquakes and their occurrence in time and space is of significant scientific and public interest. Not only does a deeper insight into the physics of fluid-induced seismicity yield fundamental knowledge on seismogenic processes in the brittle Earth's crust but it is also a crucial point for reservoir characterisation and injection performance. In the end, these are inevitable steps towards seismic hazard assessment and risk mitigation.

The focus of this thesis is on spatio-temporal migration patterns of fluid-induced seismicity at different scales. In a first study, I work with seismicity induced by the rather local effect of single-borehole, high-pressure fluid injections. This part is followed by two studies on earthquakes caused by the regional impact of large-volume injections through numerous wells under gravity. Whereas high-pressure, single-borehole injections are typically used for hydraulic fracturing operations to enhance shale gas recovery from unconventional reservoirs and for hydraulic stimulations of geothermal heat production sites, gravity-driven, large-volume injections are part of wastewater disposal which has been performed throughout the last decade in the central U.S. In the context of this work, wastewater is a saline fluid, co-produced with natural oil and gas, which is re-injected into the subsurface at a later stage. Apart from the actual injection phase, I also consider seismic events that occur in the postinjection interval of high-pressure fluid injections and in times of decreasing wastewater disposal volumes. I assess the governing question which parameters and physical processes control features of fluid-induced seismicity in time and space by joining different methods.

By means of analytical solutions, I derive a novel scaling law for postinjection-induced seismicity in the first study. My findings suggest that the spatio-temporal evolution of the seismically active zone depends on the index of non-linearity and the Euclidean dimension of pore-fluid pressure diffusion. I combine these results with numerical modelling of non-linear pore-fluid pressure diffusion in 3D. Based on the numerical pressure solutions, I generate catalogues of synthetic seismicity to validate the novel scaling relation. The subsequent successful application to different borehole injection case studies demonstrates that the relation can be used to estimate the two driving parameters of spatio-temporal features of seismicity induced by high-pressure fluid injections.

An analytical approach, combined with numerical modelling, also forms the basis of the second study. Using known relations for reservoir-induced seismicity, I present a new first-principle model for wastewater disposal-induced earthquakes observed in the crystalline basement in Central Oklahoma, U.S., called *underground reservoir-induced seismicity* (URIS). The model consists of the following

physical mechanisms; a normal stress acting on the seismogenic basement induced by the mass of the disposal fluid added to the pore-space of the target injection formation, the diffusion of pore-fluid pressure in the basement, and poroelastic coupling which contributes to pore-fluid pressure- and stress changes in the basement. I implement the novel conceptual model in a numerical finite element model, solving for poroelastic pressure- and stress changes. The obtained values are then used to calculate failure criterion stress changes and to generate synthetic clouds of seismicity. My findings demonstrate that the URIS model captures the observed time- and depth-distribution of earthquakes located in the study area both during constant and in times of declining injection volumes.

In the third study, I combine results from a time-dependent 2D cross-correlation with numerical modelling solutions to explain spatio-temporal patterns of wastewater disposal-induced seismicity in southern Kansas which seems to migrate away from the high-volume disposal area with time. The cross-correlation reveals that the majority of earthquakes preferably occurs towards the east-northeast of the disposal wells. This feature may be explained by the directional migration of poroelastic stresses and pore-fluid pressure diffusion, probably caused by a large-scale, fault-induced anisotropic character of the basement permeability. Two-dimensional numerical modelling of poroelastic pressure- and stress changes for the study area suggests that the observed shift of the seismically active zone is guided by the high permeability of the injection formation and that the depth-migration of pore-fluid pressure and poroelastic stresses is driven by the basement permeability. In general, the presented study verifies that poroelastic fluid-rock interaction may be crucial to explain seismic activity far away from large-volume disposal wells. Furthermore, it proposes that a volume reduction lowers seismicity rates only locally and that a state-wide reduction of the seismicity may require many more years.

Overall, the findings of the three works contribute to a general understanding of driving processes and parameters of fluid-induced seismicity across different scales. Thus, the presented novel model approaches may ultimately be used in future studies to assess and mitigate the risk posed by anthropogenic earthquakes.

Zusammenfassung

Es ist bekannt, dass das Einbringen von Fluiden in den Untergrund seismische Aktivität hervorrufen kann. Das Verständnis der physikalischen Prozesse, die zu diesen vom Menschen verursachten Erdbeben führen, sowie ihres zeitlichen und räumlichen Auftretens ist von großer wissenschaftlicher und gesellschaftlicher Bedeutung. Ein tieferer Einblick in die Physik der induzierten Seismizität führt nicht nur zu fundamentalem Wissen über seismogene Prozesse in der Erdkruste, sondern ist auch wichtiger Bestandteil zur Reservoir-Charakterisierung und für den Ablauf von Fluidinjektionen in den Untergrund. Schlussendlich sind dies unumgängliche Schritte in Richtung der seismischen Gefährdungsabschätzung und der Risikominimierung.

Den Schwerpunkt dieser Arbeit bilden zeitlich-räumliche Migrationsmuster von fluidinduzierter Seismizität in unterschiedlichen Dimensionen. In einer ersten Studie arbeite ich mit Seismizität, die durch den lokalen Effekt von Fluidinjektionen unter hohem Druck durch ein einzelnes Bohrloch induziert werden. Diesem Teil der Arbeit folgen zwei Studien über Erdbeben, ausgelöst durch den regionalen Effekt von zahlreichen Bohrlöchern, durch die enorme Fluidvolumen unter der Wirkung der Schwerkraft in den Untergrund eingebracht werden. Während die Fluidinjektion durch ein einzelnes Bohrloch häufig bei dem sogenannten *hydraulic fracturing* für die Schiefergas-Förderung sowie für die hydraulische Stimulierung von geothermalen Systemen eingesetzt wird, ist die Verpressung großer Fluidvolumen unter Wirkung der Schwerkraft Teil der sogenannten Brauchwasserverpressung (*wastewater disposal*), das seit dem letzten Jahrzehnt in großem Maßstab in den zentralen U.S. durchgeführt wird. Im Kontext dieser Arbeit ist Brauchwasser ein salines Fluid, das bei der Öl- und Gasproduktion mitgefördert und zu einem späteren Zeitpunkt wieder in den Untergrund eingebracht wird. Neben der Seismizität, die während der eigentlichen Injektionsphase auftritt, stehen auch Erdbeben im Fokus dieser Arbeit, die nach dem Stopp von Hochdruckinjektionen und in Zeiten reduzierter Brauchwasservolumen auftreten. Mit Hilfe verschiedener Methoden näherte ich mich vor allem der Frage, welche Parameter und physikalischen Prozesse die beobachteten zeitlichen und räumlichen Muster der fluidinduzierten Seismizität kontrollieren.

Basierend auf analytischen Lösungen leite ich in der ersten Studie ein neues Gesetz zur Skalierung postinjektions-induzierter Seismizität her. Meine Ergebnisse weisen darauf hin, dass die zeitlich-räumliche Entwicklung der seismogenen Zone nach dem Injektionsstopp durch den Index der Nichtlinearität und die euklidische Dimension der Porendruckdiffusion beeinflusst wird. Ich kombiniere diese Ergebnisse mit numerischen Modellierungen von nicht-linearer Porendruckdiffusion in 3D. Mit den berechneten Porendruckwerten generiere ich synthetische Kataloge von Seismizität, um das neue Skalierungsgesetz zu validieren. Die nachfolgende erfolgreiche Anwendung auf Fallbeispiele von durch Bohrlochinjektionen

induzierte Erdbeben demonstriert, dass die Skalierung verwendet werden kann, um die beiden Parameter abzuschätzen, die die zeitlich-räumliche Ausbreitung der Seismizität beeinflussen.

Analytische Lösungen und numerische Modellierungen bilden auch die Grundlage der zweiten Studie. Unter Verwendung bekannter analytischer Zusammenhänge sogenannter reservoirinduzierter Seismizität, stelle ich ein neues Grundsatzmodell für durch Brauchwasserverpressung hervorgerufene Erdbeben vor. Dieses Modell basiert auf Beobachtungen aus Oklahoma, U.S., wo Erdbeben im kristallinen Grundgebirge unterhalb der Injektionszone auftreten. Das neue Modell nenne ich *underground reservoir-induced seismicity* (URIS). Die Physik des Modells beruht auf einer Kombination von Mechanismen; der Masse des in den Porenraum der Zielformation eingebrachten Brauchwassers, die als Normalspannung auf das Grundgebirge wirkt, der Diffusion des Porendrucks im Grundgebirge, sowie poroelastischen Druck- und Spannungsänderungen im Grundgebirge. Ich implementiere das neue Modell in einem numerischen Finite-Elemente-Modell unter Annahme poroelastischer Druck- und Spannungsänderungen. Die erhaltenen Druck- und Spannungswerte verwende ich, um kritische Spannungsänderungen (*failure criterion stress changes*) zu berechnen und um Kataloge synthetischer Seismizität zu erzeugen. Die Ergebnisse demonstrieren, dass das URIS Modell die Zeit-Tiefen-Verteilung der im Untersuchungsgebiet beobachteten Erdbeben sowohl während konstanter als auch in Zeiten abnehmender Injektionsvolumen aufflöst.

In der dritten Studie kombiniere ich Ergebnisse einer zeitabhängigen 2D Kreuzkorrelation mit numerischen Modellierungen, um zeitlich-räumliche Muster von Erdbeben im Süden von Kansas, U.S., zu erklären. Dort entfernt sich die seismogene Zone mit der Zeit von dem Gebiet hoher Brauchwasser-Injektionsvolumen. Die Kreuzkorrelation weist darauf hin, dass die Mehrzahl der Erdbeben präferiert im Ostnordost der Injektoren auftritt. Eine denkbare Erklärung für dieses Muster ist die gerichtete Migration der poroelastischen Spannungen und der Porendruckdiffusion, möglicherweise hervorgerufen durch eine großmaßstäbliche, durch Störungszonen verursachte, Permeabilitätsanisotropie des Grundgebirges. Die Ergebnisse einer numerischen 2D Modellierung von poroelastischen Druck- und Spannungsänderungen im Untersuchungsgebiet deuten darauf hin, dass die Verlagerung der seismisch aktiven Zone durch die hohe Permeabilität der Injektionszone geleitet wird und dass die anisotrope Permeabilität des Grundgebirges die Tiefenmigration des Porendrucks und der poroelastischen Spannungen hervorruft. Damit verifiziert die präsentierte Studie die Beobachtung, dass poroelastische Gesteins-Fluid-Interaktionen notwendig sind, um Seismizität in großen Entfernungen von Injektoren, die große Volumen Brauchwasser verpressen, auszulösen. Des Weiteren lassen die Ergebnisse darauf schließen, dass verringerte Injektionsvolumen zunächst nur lokal zu abklingender Seismizität führen. Die staatenweite Reduktion der Seismizitätsrate könnte noch viele Jahre andauern.

Im Gesamten tragen die drei Arbeiten zu einem generellen Verständnis der führenden Prozesse und Parameter von fluidinduzierter Seismizität in verschiedenen Dimensionen bei. Die präsentierten neuartigen Modellierungsansätze können so in zukünftigen Studien letztlich dazu dienen, die Gefährdung durch anthropogene Erdbeben besser abzuschätzen und möglicherweise zu reduzieren.

Contents

1	Introduction	1
2	Theory of Fluid-Induced Seismicity	7
2.1	Geomechanical Introduction	11
2.2	Failure Theory	13
2.3	Pore-Fluid Pressure Diffusion as a Triggering Mechanism	17
2.4	Poroelastic Stress Changes	21
3	Scaling of Seismicity Induced by Nonlinear Fluid-Rock Interaction after an Injection Stop	25
4	The Surge of Earthquakes in Central Oklahoma Has Features of Reservoir-Induced Seismicity	47
5	Understanding Vectorial Migration Patterns of Wastewater-Induced Earthquakes in the U.S.	83
6	Conclusions and Outlook	115
	Bibliography	119
	Curriculum Vitae	127
	Publications and Conference Abstracts	129
	Acknowledgements	131

CHAPTER 1

Introduction

Earthquakes associated with human activity, also referred to as *induced seismicity* (National Research Council, 2013; Ellsworth, 2013), have become a widely discussed topic in recent years. This is not only due to their potential risk of causing damage to people, environment and infrastructure, but also because the seismicity controlling processes remain controversial. Even though it is generally accepted that the main mechanism of induced seismicity is the destabilisation of critically stressed, pre-existing faults in the brittle Earth's crust due to pressure- and/or stress perturbations, various details are still not understood. Hence, comprehensive hydro-geomechanical studies are inevitable. However, these analyses are frequently limited by the availability of injection data and hydrological- as well as geological field reports. To date, it is known that different industrial activities may lead to induced seismic events (McGarr et al., 2002; Ellsworth, 2013). These are for example mining operations (Cook, 1976; Gibowicz and Kijko, 1994), the filling of surface reservoirs, known as reservoir impoundment (Simpson, 1976; Gupta, 1992), the extraction of hydrocarbons from conventional reservoirs (van Eck et al., 2006), the subsurface disposal of wastewater (Ellsworth, 2013) as well as high-pressure fluid injections into the subsurface for shale gas extraction (Atkinson et al., 2020) and geothermal heat production (Häring et al., 2008; Deichmann and Giardini, 2009).

Provoked by the lack of knowledge as well as by the deep socioeconomic impact, the scientific interest in induced seismicity is growing. This led to an increased number of publications of studies on the physics and controlling parameters of

fluid-induced seismicity in recent years (Grigoli et al., 2017). Although the physics strongly depend on the injection site and the specific fluid operation, a valuable universal tool is the comparison of observed induced earthquakes and modelled synthetic seismicity. For this purpose, various approaches have been proposed and discussed in literature. Generally, they are based on the analytical- and/or numerical computation of pressure- and stress changes. The obtained solutions may then be used for the generation of synthetic seismicity and for the comparison of spatio-temporal features of both synthetic and observed earthquakes. However, depending on input parameters, the model geometry, boundary conditions, the effect of poroelastic coupling, and statistical considerations regarding the generation of synthetic event clouds, the obtained findings may differ from case to case and from author to author. Some examples that demonstrate this are given in the following paragraphs.

Let us consider high-pressure fluid injections. Commonly, they are used for hydraulic fracturing of shale gas reservoirs and for the hydraulic stimulation of geothermal systems. According to Talwani and Acree (1984), the spatio-temporal evolution of a seismic event cloud can be described by the diffusive relaxation of a pore-fluid pressure perturbation. Additionally, Langenbruch and Shapiro (2010) demonstrated that the return to an equalised pressure state after the injection stop may also be described by such a mechanism. The pore-fluid pressure diffusion may be linear, thus controlled by a constant hydraulic diffusivity (Shapiro et al., 1997, 1999), or non-linear with a hydraulic diffusivity that depends on the pore-fluid pressure (Shapiro and Dinske, 2009; Hummel and Müller, 2009). In contrast to pressure diffusion-based approaches, there are also works claiming that poroelastic coupling, i.e. accepting that pore-fluid pressure changes induce stress changes and vice versa, should be taken into account for the modelling of fluid-induced seismicity. Schoenball et al. (2010) applied numerical poroelastic 2D modelling to explain principal features of injection-induced events in pre-stressed rocks and Segall and Lu (2015) used hydro-mechanical modelling for a point-like fluid injection into a poroelastic half-space, showing that poroelastic stress changes have a significant effect at large distances from the injector. More recently, Zbinden et al. (2020) performed poroelastic modelling for the Deep Geothermal Project in St. Gallen, Switzerland. However, they found that poroelastic stressing plays a minor role in inducing seismicity compared to the fast effect of pore-fluid pressure diffusion through the highly fractured reservoir rock.

As a second example, let us consider wastewater disposal-induced earthquakes. Unlike high-pressure fluid injections, wastewater disposal frequently continues over months to years, injecting tremendous fluid volumes at rates of up to several thousands of cubic meters per month at low injection pressures (Goebel et al., 2017). Unlike in the case of short-term high-pressure injections, it remains a challenging task to clearly link seismic activity to large-scale wastewater disposal. In the central U.S., especially in the states of Oklahoma and Kansas, it is not just

one single well but the impact of thousands of disposal wells (Langenbruch and Zoback, 2016; Walsh and Zoback, 2015), the seismically active zone lies deep below the injection formation in the fractured crystalline basement (Schoenball and Ellsworth, 2017a), and earthquakes frequently occur over extensive areas, far from disposal wells (Goebel et al., 2017; Peterie et al., 2018). Aiming at explaining observed spatio-temporal signatures of the observed seismicity, various works have been published to date. Keranen et al. (2013, 2014) attribute seismic activity in Oklahoma to the increased pore-fluid pressure which causes critical pressure changes at seismogenic depth of 2 km to 5 km at horizontal distances of up to 35 km from wastewater disposal wells. Langenbruch et al. (2018) generate hazard maps for the central U.S. based on the assumption of pore-fluid pressure diffusion. In contrast, Chang and Segall (2016) perform 2D poroelastic modelling of a fluid injection into a permeable sandstone reservoir, taking into account the presence of (reservoir intersecting) permeable faults in the crystalline basement. Their results demonstrate that poroelastic coupling plays a major role in inducing stress changes large enough to produce seismicity along basement faults. Goebel et al. (2017) focus on the 2016 M_w 5.1 Fairview earthquake sequence in Oklahoma which was most likely induced by massive wastewater disposal in this area. They propose that the direct effect of pore-fluid pressure diffusion controls near-injection seismicity, whereas poroelastic stress changes may dominate these pressure changes at distances of up to 50 km from high-rate injectors, and thus are the driving mechanism of far-field seismicity.

To assess the question which physical processes and parameters control fluid-induced seismicity, the comparison of spatio-temporal features of synthetic event clouds and observed seismicity is frequently performed. However, different approaches are proposed regarding the method to generate catalogues of synthetic seismicity. Assuming pressure diffusion as the main triggering mechanism, Rothert and Shapiro (2003, 2007) describe the spatio-temporal distribution of induced events based on a *seed model*. In this context, seed points represent locations in the medium that are close to failure, i.e. possible pre-existing fractures and faults. The points are randomly distributed in the medium and each point is assigned a critical stress value, statistically distributed between a minimum and a maximum. The model is defined such that the higher this value, the more stable the corresponding location. It follows that a seismic event occurs if the pressure perturbation at a certain location exceeds its critical value (see also Hummel and Müller, 2009; Langenbruch and Shapiro, 2010; Johann et al., 2016, 2018). In contrast, an approach called rate-and-state friction model has been introduced by Dieterich (1994). Here, changes in the seismicity rate are linked to changes in the Coulomb failure stress. It is assumed that the seismicity rate remains constant as long as stress changes are absent and that earthquake sources are controlled by rate and state friction (see eg. Segall and Lu, 2015).

These works, to provide a few examples, demonstrate the variety and sometimes

even opposing nature of publications on fluid-induced seismicity. The availability of seismic monitoring systems and injection data as well as knowledge about geological structures and rock parameters of the involved formations further influence the set-up of precise geophysical models. This increases the complexity of published works even more. In turn, the above-mentioned points contribute to the seismic hazard assessment and are fundamental for the consideration of possible consequences for the public, the industry and regulators (Ellsworth, 2013). Ultimately, the risk of induced earthquakes may only be mitigated if advances in model techniques are combined with field data such as knowledge of pre-existing faults and in situ stress- and pressure conditions as well as with reports on regional tectonic seismic activity.

In this thesis, I work with fluid-induced seismicity, focusing on (typically small-magnitude microseismic) earthquakes induced by the rather local effect of high-pressure fluid injections through a borehole in the context of shale gas exploration and geothermal heat production as well as on (overall larger magnitude, possibly felt) earthquakes linked to the regional impact of large-volume wastewater disposal through thousands of wells under the force of gravity into a deep aquifer in the central U.S.

Motivated by the large number of unknowns in the field of fluid-induced seismicity, the main goal of this thesis is the achievement of a deeper understanding of seismicity driving physical mechanisms and the evaluation of governing parameters on both local (high-pressure fluid injections) and regional (wastewater disposal) scale. Even though many studies have been published on the physics of fluid-induced seismicity and applied to cases such as hydraulic fracturing or wastewater disposal, the discussed approaches tend to become increasingly complex. Not only does this require higher computational expenses but it also introduces errors due to parameter uncertainties. Therefore, another goal of the presented works is to develop minimum-complexity models which are still able to capture principal features of the recorded seismicity and to provide a reasonable parameterisation of the observed spatio-temporal patterns.

By means of analytical solutions and numerical models, I assessed the key question *Which parameters and physical mechanisms control observed spatio-temporal signatures of different types of fluid-induced seismicity?*. Please note that I do not distinguish between the terms *induced* and *triggered* earthquakes. McGarr et al. (2002) proposed to use the terms with regard to the source of the seismic stress change. While the term *triggered* should be used to refer to an earthquake that releases mainly tectonic stresses, the term *induced* refers to events that release primarily stresses of industrial origin. Here, I follow other works (e.g. Ellsworth, 2013) and use the terms interchangeably without implications for the stress origin.

Chapter 2 embeds my work into the state of the art of research on fluid-induced

seismicity and provides an introduction to necessary geomechanical theory. Thereby, this chapter frames the three works presented in the subsequent chapters.

Chapters 3 to 5 are published, peer-reviewed journal articles, referenced to as Johann et al. (2016), Johann et al. (2018) and Johann and Shapiro (2020). Although each of the articles presents an independent work and the presented cases of fluid-induced seismicity differ in their cause (high-pressure fluid-injection versus wastewater disposal), the thesis as a whole yields a deeper understanding of physical processes and parameters controlling seismicity induced by various fluid-injection operations. Therefore, the study of spatio-temporal features of the observed seismicity forms a linking element of this thesis, fundamental for future studies.

The work presented in chapter 3 investigates the controlling parameters of postinjection-induced events. Seismicity which occurs after the injection stop shows two significant characteristics: The triggering front enveloping the farthest induced events, and the back front which forms the lower boundary to the seismic cloud, representing the growing aseismic zone. Based on the assumption of non-linear pore-fluid pressure diffusion, a novel scaling relation for the two fronts is derived, suggesting that the spatio-temporal evolution of the seismic cloud depends on the Euclidean dimension of the pressure diffusion, and thus on the dominant growth direction of the seismically active zone, as well as the non-linearity of the diffusion. Subsequent numerical modelling verifies the scaling law that was then applied to case studies of seismicity induced by fluid operations in shale gas- and geothermal heat reservoirs. The results show that the scaling relation can be applied to estimate the seismicity controlling parameters. Therefore, it is of great advantage for future studies on postinjection-induced seismicity and reservoir characterisation.

Thereafter I present two chapters on earthquakes induced by wastewater disposal in the central U.S. Chapter 4 deals with spatio-temporal features of seismicity in Oklahoma, focusing on their depth migration. I introduce a novel model based on the theory of reservoir-induced seismicity, called *underground-reservoir induced seismicity* (URIS). Considering the fill-up of the underpressured, highly porous injection aquifer and the resulting build-up of an effective water layer on top of the basement, the work demonstrates that induced poroelastic pressure- and stress changes at seismogenic depth are large enough to cause earthquakes along pre-existing faults. Furthermore, the URIS model is capable to resolve the observed seismicity rate during both constant and declining injection rates. Chapter 5 complements the study on wastewater disposal-induced earthquakes with an analysis of spatio-temporal features of seismicity in southern Kansas. In this region, it has been observed that the seismogenic zone in Kansas shifts towards the northeast with time, away from large-volume disposal wells. I analyse horizontal migration patterns by developing a comprehensive approach that

combines results from a time-dependent two-dimensional cross-correlation technique with numerical finite element modelling of poroelastic pressure- and stress changes. The work validates the observation that earthquakes preferably occur towards the north-east of disposal wells, it suggests that this feature is provoked by a large-scale hydraulic anisotropy of the seismogenic basement, and that poroelastic fluid-rock interaction plays a major role for the induced seismicity in the study area.

I finalise the thesis with chapter 6, giving a summary of the main findings presented in chapters 3 to 5 and addressing possible future research directions.

CHAPTER 2

Fluid-Induced Seismicity - Integration into Ongoing Research and Basic Theories

Between 1962 and 1967, an unusual series of earthquakes occurred at the Rocky Mountain Arsenal wastewater disposal site near Denver, Colorado, U.S. As earthquake magnitudes were up to $M5.5$, the seismic activity was of major public concern and attracted scientific interest (Hsieh and Bredehoeft, 1981). Shortly after this observation, Healy et al. (1968) connected the seismicity to the fluid injection at the disposal site. The authors assumed that the earthquakes were a direct response to the perturbation of the in situ pore-fluid pressure. Such a mechanism had already been proposed earlier by Rubey and Hubbert (1959) and Nur and Booker (1972) attributed the occurrence of aftershocks to the delayed effect of pore-fluid pressure diffusion.

Ever since these early works on fluid-induced seismicity and its controlling mechanisms, further research has been conducted in this field. Simpson (1976) studied the occurrence of seismicity at reservoir impoundment sites worldwide. He evaluated numerous cases of earthquakes, ranging in magnitude from small microseismic events to large, damaging earthquakes, and concluded that their occurrence is most likely due to water level fluctuations in the reservoirs. Additionally, it has been observed in some cases that the seismically active zones migrated away from the reservoir sites with time. According to Talwani and Acree (1984), this is caused by the pressure diffusion as proposed by Rubey and Hubbert (1959).

By now it is understood that fluid-induced seismicity is a direct consequence of

pore-fluid pressure- and stress changes, initiated at the fluid source. If perturbations of the initial stress- and pressure field are large enough, pre-existing faults are destabilised, resulting in shear failure along the fault planes.

Even though the fundamental works on fluid-induced seismicity have been conducted on the basis of wastewater disposal sites (Healy et al., 1968) and reservoir impoundment (Simpson, 1976), it is now understood that various types of fluid operations have the potential to induce earthquakes (e.g. McGarr et al., 2002; Ellsworth, 2013; Grigoli et al., 2017). The magnitudes of these events may vary from small, unnoticeable seismicity (referred to as *microseismicity* with $M \leq 2$) to large, destructive earthquakes (Suckale, 2009). The Human-Induced Earthquake Database (*HiQuake*) currently lists 1174 projects that may be linked to anthropogenic seismic activity (Foulger et al., 2018). Some types of fluid operations linked to seismicity are briefly addressed in the following paragraphs.

One well-known cause of induced seismicity is the hydrocarbon production from conventional reservoirs (Suckale, 2009). A leading example are earthquakes observed at the Groningen gas field, the Netherlands. Located in the north of the country in an area considered tectonically stable, it is Europe's largest onshore gas field and has been in production since 1963 (Bourne et al., 2014). Concurrently with subsurface subsidence, seismicity started in 1991 when the depletion of the reservoir was approximately 28% (Foulger et al., 2018). Ever since the first cases of seismic activity in 1991, eight earthquakes with a magnitude larger than three have been recorded in the Groningen gas field until 2014 (Van Wees et al., 2014). To date, the largest of these events is the August 2012 M_w 3.6 Huizinge earthquake in the province of Groningen. It caused a lot of damage, especially to the old brick buildings (Dost and Kraaijpoel, 2013), and led to the set-up of a large microseismic monitoring network. Yet, magnitudes of the Groningen earthquakes are not atypical for hydrocarbon production related events which are frequently in the range of $3 \leq M < 4$ (Foulger et al., 2018).

With the discovery of unconventional gas reservoirs throughout the last decades, a new origin of public concern arose: hydraulic fracturing, also known as *fracking* (Figure 2.1). This is not only due to environmental aspects but also because of seismic events which frequently accompany these high-pressure subsurface fluid injections. Developed in the 1940s (Hubbert and Willis, 1957; Montgomery and Smith, 2010; Warpinski et al., 2012), hydraulic fracturing is not a new technique. Yet, it is the large-scale application in the hydrocarbon industry which has made it popular. Hydraulic fracturing is described as the injection of fluids, often water-sand mixtures, into a (low permeable) subsurface rock formation. Due to a high injection pressure, usually larger than the minimum principal tectonic stress, new fractures and cracks are created. This increases the in situ permeability and facilitates fluid flow through the medium. Used in the hydrocarbon industry, the oil and gas recovery from low-permeable hydrocarbon-rich source rocks such as

shales (e.g. Atkinson et al., 2020) may be enhanced by this technique. According to the *HiQuake* project, largest magnitudes of hydraulic fracturing related earthquakes vary between $2 \leq M < 3$ (Foulger et al., 2018). Nevertheless, some felt-events above $M3$ have also been recorded in recent years (Atkinson et al., 2020). To date, the largest event associated with hydraulic fracturing is the December 2018 $M_w 5.3$ earthquake in the Sichuan Basin, China (Lei et al., 2019). It occurred close to a shale gas field and caused economic damage and some injuries.

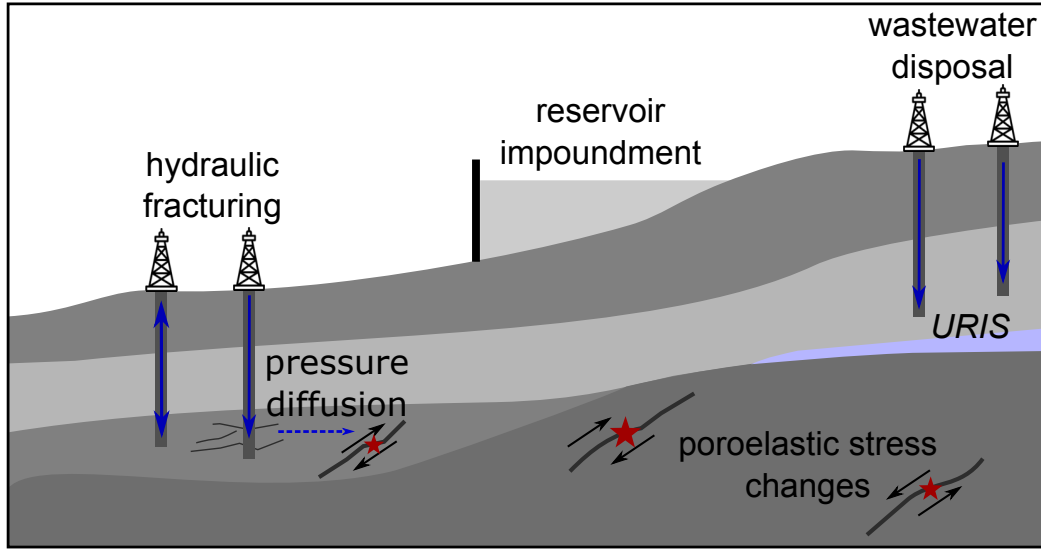


Figure 2.1. Different causes of fluid-induced seismicity addressed in this thesis. Due to pore-fluid pressure- and stress perturbations of the in situ stress state, pre-existing faults may be activated, resulting in seismic events. In this work, hydraulic fracturing (left part) is addressed in the context of shale gas exploration and geothermal heat production. In this case, the diffusion of pore pressure is assumed to be the dominant mechanism for fault destabilisation. In contrast, reservoir impoundment (middle part) may cause poroelastic stress changes at greater depth due to the weight of the water column as well as the pressure at the bottom of the artificial lake. If these changes are large enough along pre-existing faults, earthquakes may occur. I applied the fundamentals of reservoir-induced seismicity (RIS) to earthquakes linked to wastewater disposal (right part), introducing a new conceptual model called underground reservoir-induced seismicity (URIS).

Another source of fluid-induced seismicity is the exploitation of geothermal heat, especially from so-called Enhanced Geothermal Systems (EGS). In EGS, the rock is hydraulically stimulated by large injection pressures to enhance the natural fracture network of a deep, low-permeable rock formation such as granite. As a consequence, the circulation of fluids between two (injection and production) wells, drilled to produce the geothermal heat, is facilitated (e.g. Grigoli et al., 2017; Atkinson et al., 2020). Well-studied cases of induced seismic activity are

the Fenton Hill site in New Mexico, U.S., being constructed in the 1970s with massive fluid injections in later years (e.g. Fehler, 1989; Shapiro, 2015), and the 1987 Soultz-sous-Forêts project in the Upper Rhine Graben in eastern France (Baisch et al., 2010; Shapiro, 2015). Further examples are the Basel EGS in Switzerland, put into operation in 2006 (Häring et al., 2008), and the Cooper Basin EGS in Australia, with injections between 2003 and 2012 (Asanuma et al., 2005; Baisch et al., 2015). Apart from microseismic activity, which frequently accompanies EGS operations, larger magnitude events are observed every now and then. One case is the $M_L2.6$ earthquake that occurred at the EGS in Basel at the peak of the injection, leading to the injection stop. However, after the shut-in of the well, an even bigger, $M_L3.4$ event occurred in December 2006 (Häring et al., 2008). This finally caused the suspension of the EGS project. Other noteworthy earthquakes were recorded at the Soultz ($M_L2.9$) and Cooper Basin EGS ($M_w3.7$, Foulger et al., 2018).

Recently, the massive disposal of large volumes of wastewater in the central U.S. arouse public and scientific interest. In this case, wastewater is a saline fluid co-produced with gas from unconventional reservoirs that is re-injected into a highly porous aquifer overlying the crystalline basement (Figure 2.1). As a consequence, numerous earthquakes have occurred since 2009 in a usually seismically quiet area in the states of Oklahoma and Kansas (see e.g. Ellsworth, 2013; Keranen et al., 2013; Yeck et al., 2017). Compared to the examples of induced seismicity addressed above, it is understood that massive wastewater disposal may also potentially induce larger magnitude earthquakes. Throughout the central U.S., numerous widely felt $M \geq 4$ events have been reported (Ellsworth, 2013; Walsh and Zoback, 2015; Langenbruch and Zoback, 2016), some of which caused minor to severe damage. The strongest earthquake to date ($M_w5.8$) occurred in September 2016 close to the city of Pawnee, Oklahoma (Chen et al., 2017).

Overall, the largest magnitudes may be linked to earthquakes induced by reservoir impoundment, so-called reservoir-induced seismicity (RIS, Figure 2.1, Grigoli et al., 2017; Foulger et al., 2018). In December 1967, a deadly $M6.3$ earthquake happened close to the Koyna-Warna dam, India, probably caused by seasonal lake level changes. Ever since this event, seismicity in the Koyna-Warna region has been continuing (Talwani and Acree, 1984; Talwani, 1995, 1997; Gupta, 2002; McGarr et al., 2002). Another, yet controversial case is the May 2008 $M_w7.9$ earthquake which struck a seismically active area in the Sichuan province in China, around 20 km from the Zipingpu Dam (Klose, 2011; Lei et al., 2008; Gahalaut and Gahalaut, 2010; Tao et al., 2015). In principal, it is understood that RIS is a consequence of the additional weight of the water column as well as the pore-fluid pressure at the bottom of the artificial lake that cause stress- and pressure changes below the reservoir. These changes perturb the in situ stress field and may cause shear failure along pre-existing faults (Talwani and Acree, 1984; Simpson et al., 1988; Gupta, 1992).

The above examples demonstrate that the occurrence of fluid-induced earthquakes and its profound effects are of great public and economic interest. Understanding spatio-temporal patterns of the induced events is therefore fundamental for safe fluid operations and the assessment as well as the mitigation of the seismic hazard. Even though fluid-induced seismicity has received considerable attention in recent years due to its socioeconomic impact, scientific interest in this topic also arose when studies revealed that spatio-temporal patterns of microseismicity may contribute to reservoir characterisation (Shapiro et al., 1997, 1999, 2002; Hummel and Shapiro, 2012). Therefore, controlled fluid injections and advanced seismic monitoring are a valuable research tool.

However, governing processes are complex and controlling parameters are not fully understood, making fluid-induced seismicity a challenging subject. The three works presented in this thesis contribute to the ongoing research on fluid-induced seismicity, aiming at achieving a deeper understanding of the seismicity controlling physics and crucial parameters: From the local effect of high-pressure, single-borehole fluid injections to the regional impact of high-volume wastewater disposal through a vast number of wells. While chapter 3 addresses seismicity occurring in the postinjection phase of high-pressure fluid injections into shale gas reservoirs and at EGS sites, chapters 4 and 5 focus on spatio-temporal features of wastewater disposal-induced earthquakes in the central U.S.

A concise overview over geomechanical- and hydrogeological theories necessary to study spatio-temporal patterns of fluid-induced seismicity is given in the following sections. It is based on fundamental works by Wang (2000); Jaeger et al. (2007); Shapiro (2015). Further equations and theory relevant for chapters 3 to 5 can be found in the corresponding chapters.

2.1 Geomechanical Introduction

The description of the physics of fluid-induced seismicity dates back to the 17th century, when the British physicist Robert Hooke formulated the well-known *Hooke's law*. With the assumption of a linear elastic material and small deformation, it links the stress tensor σ_{ij} to the strain tensor ϵ_{kl} :

$$\sigma_{ij} = C_{ijkl}\epsilon_{kl}. \quad (2.1)$$

Here, the fourth-rank tensor C_{ijkl} denotes the elastic stiffness tensor.

Assuming symmetry of the strain and stress tensors, the stiffness tensor will be symmetric as well in (i, j) and (k, l) . Moreover, $C_{ijkl} = C_{klij}$ (Jaeger et al., 2007). Following these symmetries, the stiffness tensor for an isotropic medium is defined

in Aki and Richards (2002) as:

$$C_{ijkl} = \lambda \delta_{ij} \delta_{kl} + G(\delta_{ik} \delta_{jl} + \delta_{il} \delta_{jk}), \quad (2.2)$$

where λ and G denote the Lamé parameters under drained conditions. Note that G is frequently referred to as the shear modulus. Using this expression, Hooke's law (equation (2.1)) can be reformulated for an isotropic medium:

$$\sigma_{ij} = \lambda \delta_{ij} \epsilon + 2G \epsilon_{ij}. \quad (2.3)$$

Considering an elementary volume V of a cuboid with side lengths l_x , l_y and l_z , ϵ is the volumetric strain (dilatation) dV/V given by $\epsilon = \epsilon_{xx} + \epsilon_{yy} + \epsilon_{zz}$.

As can be seen from equation (2.3), two elastic constants define Hooke's law for an elastically isotropic medium. These are the Lamé parameters λ and G . Other elastic moduli for isotropic elastic solids under drained conditions are connected to these parameters by:

$$K = \lambda + \frac{2}{3}G, \quad (2.4)$$

$$E = G + \frac{3\lambda + 2G}{\lambda + G}, \quad (2.5)$$

$$\nu = \frac{\lambda}{2(\lambda + G)}, \quad (2.6)$$

where K and E denote the bulk- and Young's modulus, respectively, and ν is the Poisson's ratio.

The elastic parameters basically control the elastic deformation of a medium. If elastic deformation occurs, the medium is brought from one state of equilibrium to another by the propagation of elastic waves. In terms of Hooke's law, elastic equilibrium can be written as (Shapiro, 2015):

$$\frac{\partial \sigma_{ij}}{\partial x_j} = 0. \quad (2.7)$$

Therefore, knowledge of the elastic constants is fundamental to describe the propagation of elastic waves from a source through a medium.

One special case of elastic waves are seismic waves which travel through the Earth after an earthquake (see e.g. Shearer, 2009; Shapiro, 2015, and references therein). Earthquakes typically occur along faults and fractures which are zones of weakness in the brittle Earth's crust, inherently weaker than the surrounding rock (Lay and Wallace, 1995). Due to tectonic stresses or human activities, the shear strength of such a pre-existing fault may be exceeded. This causes quick, spontaneous shear motion along the fault plane, resulting in an earthquake.

In terms of tectonic stresses, it is reasonable to introduce a coordinate system in which the traction vectors acting on the coordinate planes are parallel to the plane normals. These vectors are also referred to as *principal tectonic stresses*, σ_1 , σ_2 and σ_3 . In this thesis, I follow the standard continuum mechanics notation that compressive stresses are negative and that the projection of the principal stresses onto their corresponding parallel coordinate axis is denoted by $-\sigma_1$, $-\sigma_2$, $-\sigma_3$. It follows that the algebraic quantities σ_1 , σ_2 and σ_3 are positive if compressive and ordered such that $\sigma_1 \geq \sigma_2 \geq \sigma_3$ (see also Shapiro, 2015; Johann et al., 2018; Johann and Shapiro, 2020). Thus, they correspond to the maximum, intermediate and minimum compressive tectonic stresses, respectively. The stress tensor σ_{ij} is then given by its three diagonal components σ_{xx} , σ_{yy} and σ_{zz} . If one of the principal tectonic stresses is vertically oriented, denoted by σ_{zz} , the other two stresses act in horizontal direction, σ_{xx} and σ_{yy} . From this it follows for a normal faulting regime (σ_1 in vertical direction): $\sigma_{zz} = -\sigma_1$, $\sigma_{xx} = -\sigma_2$, $\sigma_{yy} = -\sigma_3$, for a strike-slip faulting regime (σ_1 in horizontal direction): $\sigma_{xx} = -\sigma_1$, $\sigma_{zz} = -\sigma_2$, $\sigma_{yy} = -\sigma_3$, and for a thrust faulting regime (σ_3 in vertical direction): $\sigma_{xx} = -\sigma_1$, $\sigma_{yy} = -\sigma_2$, $\sigma_{zz} = -\sigma_3$.

2.2 Failure Theory

Fluid-induced seismicity as introduced above is caused by shear failure of pre-existing faults in the stressed subsurface (see e.g. Jaeger et al., 2007). One widely used theory to describe the failure of these faults is the Coulomb failure criterion (Coulomb, 1773). He assumed that rock failure along a fault plane is due to the shear stress τ acting along such a plane. This motion is resisted by the sum of a frictional stress $\mu_f \sigma_n$ and the cohesion C_c . Here, μ_f is the coefficient of friction and σ_n the normal stress on the fault. Failure occurs if the so-called Coulomb criterion:

$$|\tau| = C_c + \mu_f \sigma_n \quad (2.8)$$

is satisfied. Note that the sign of τ only influences the direction of motion such that the absolute value is used in the failure criterion.

2.2.1 Porous Media

So far I regarded rocks as media which consist of a matrix composed of solid grains. As a first order approximation, I assumed this matrix to be isotropic and homogeneous (Figure 2.2, left panel). Normal stresses acting on the rock matrix are supported by the grains. However, in reality, the rock matrix is typically porous and the pore space may be filled with some fluid phase under pressure p (Figure 2.2, right panel). Since the pore pressure counteracts the normal stresses,

the presence of a pore fluid influences the failure strength of the rock.

Therefore, Terzaghi (1936) proposed to use *effective stresses*, σ_{eff} . Following his concept, effective normal stresses are given by the normal stresses reduced by the pore-fluid pressure in all three principal stress directions equally: $\sigma_{1,eff} = \sigma_1 - p$, $\sigma_{2,eff} = \sigma_2 - p$ and $\sigma_{3,eff} = \sigma_3 - p$. In contrast, shear stresses are not altered by the pore-fluid pressure. The Coulomb criterion is then given by:

$$|\tau| = C_c + \mu_f (\sigma_n - p) . \quad (2.9)$$

Thus, the presence of a pore fluid generally weakens the rock volume as well as pre-existing fractures therein.

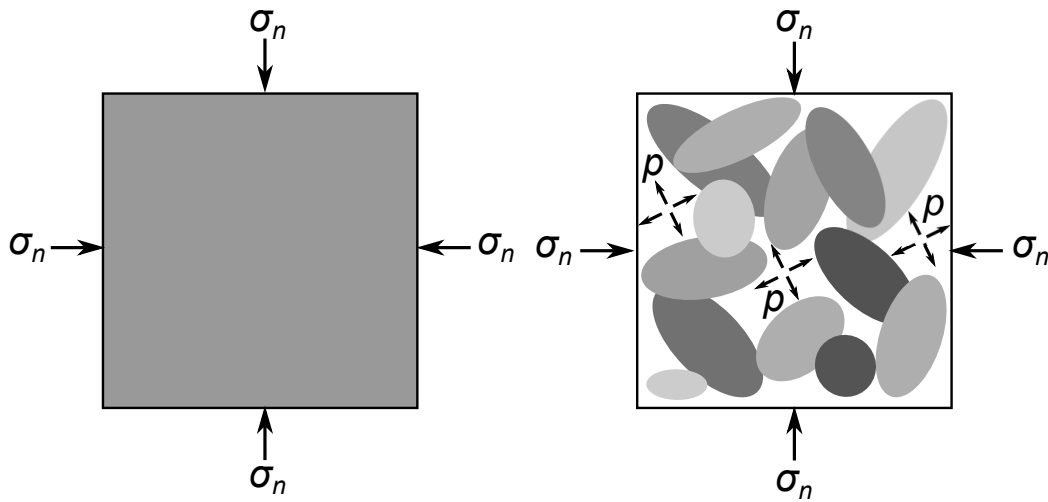


Figure 2.2. A sketch of two hypothetical media. The left panel depicts a medium which consists of a solid phase only (grey surface). In contrast, a more realistic example is shown on the right. Here, the medium consists of a solid skeleton made up of grain material (grey ellipses) and of pore space which may be filled with some saturating fluid phase (white space). Whereas the solid matrix supports elastic stresses, here normal stresses σ_n , the pore pressure p is supported by the pore fluid and counteracts the normal stress.

2.2.2 Mohr Diagrams and Failure Criterion Stress Changes

The stress state of faults can be graphically analysed by so-called Mohr diagrams (see Figure 2.3). These diagrams relate the shear and normal stress (τ and σ_n on the y - and x -axes, respectively) that act on a fault plane of a given orientation θ with respect to the direction of the maximum principal stress σ_1 . For further considerations it is meaningful to use Terzaghi's principle of effective stresses

introduced above. Rather than defining the total normal stress on the x -axis, a modified coordinate system $(\sigma_n - p, \tau)$ can be used (Shapiro, 2015).

Let us first assume a 2D stress state but denote the minimum principal stress by σ_3 . Depending on the stresses acting on a fault with orientation θ , a circle defined by:

$$\left(\sigma_{n,eff} - \frac{\sigma_{1,eff} + \sigma_{3,eff}}{2}\right)^2 + \left(\frac{\sigma_{1,eff} - \sigma_{3,eff}}{2} \sin 2\theta\right)^2 = \frac{(\sigma_{1,eff} - \sigma_{3,eff})^2}{4} \quad (2.10)$$

can be plotted (Figure 2.3, grey circle). The so-called *Mohr circle* is then fully described by its diameter $\sigma_1 - \sigma_3$ and by its midpoint $(\sigma_{1,eff} + \sigma_{3,eff})/2$, corresponding to the differential stress σ_d and the effective mean stress $\sigma_{m,eff}$, respectively. Equation 2.10 can then be written as:

$$(\sigma_{n,eff} - \sigma_{m,eff})^2 + \left(\frac{\sigma_d}{2} \sin 2\theta\right)^2 = \frac{\sigma_d^2}{4}. \quad (2.11)$$

Note that the differential stress is not influenced by the presence of a pore fluid. In the Mohr diagram, the Coulomb failure criterion is represented by a straight line with slope μ_f , also referred to as the failure envelope, that intercepts the τ -axis at C_c (Figure 2.3, black straight line). The angle between this line and the σ_n -axis is given by the friction angle $\Phi_f = \arctan \mu_f$.

A valuable method to examine the potential of shear failure along a fault plane is the failure criterion stress *FCS*. Taking a pre-existing, critically stressed fault with a certain orientation θ to the maximum principal stress (Figure 2.3, inset), the fault may be depicted by a point on the Mohr circle. The distance between this point and the Coulomb failure criterion defines the failure criterion stress (see e.g. Shapiro, 2015):

$$FCS = 0.5\sigma_d - \sin \varphi (\sigma_m - p) - C_c \cos \varphi. \quad (2.12)$$

FCS can take positive and negative values. Whereas a negative *FCS* characterises a stable fault, a positive value implies an unstable stress state, resulting in shear failure along the corresponding fault plane.

Assuming that subsurface rock formations are poroelastic media, the in situ pore-fluid pressure and tectonic stresses may be perturbed by human activities such as fluid injection- and production operations. These perturbations result in changes of the failure criterion stress, denoted as ΔFCS . Accepting that the cohesion and friction coefficient remain constant, ΔFCS is given by:

$$\Delta FCS = 0.5\Delta\sigma_d - \sin \varphi (\Delta\sigma_m - \Delta p). \quad (2.13)$$

If ΔFCS is negative, a given optimally oriented fault is stabilised. In contrast, a

positive value of ΔFCS indicates fault destabilisation. Visually speaking, destabilisation means that the Mohr circle moves closer to the failure envelope. Once it intersects the failure criterion in one point, shear failure of the fracture with optimal orientation to the maximum principal stress, defined by an angle θ_{opt} , occurs. The corresponding optimal angle is given by $\theta_{opt} = 0.5 \arctan 1/\mu_f$. With a friction coefficient between 0.6 and 1, as frequently observed, θ_{opt} varies between 30° and 22.5° (Shapiro, 2015).

Equation 2.13 demonstrates that fault destabilisation (positive ΔFCS) may result from a decreasing mean stress (negative $\Delta\sigma_m$) and from an increasing differential stress or pore-fluid pressure (positive $\Delta\sigma_d$ and p , respectively).

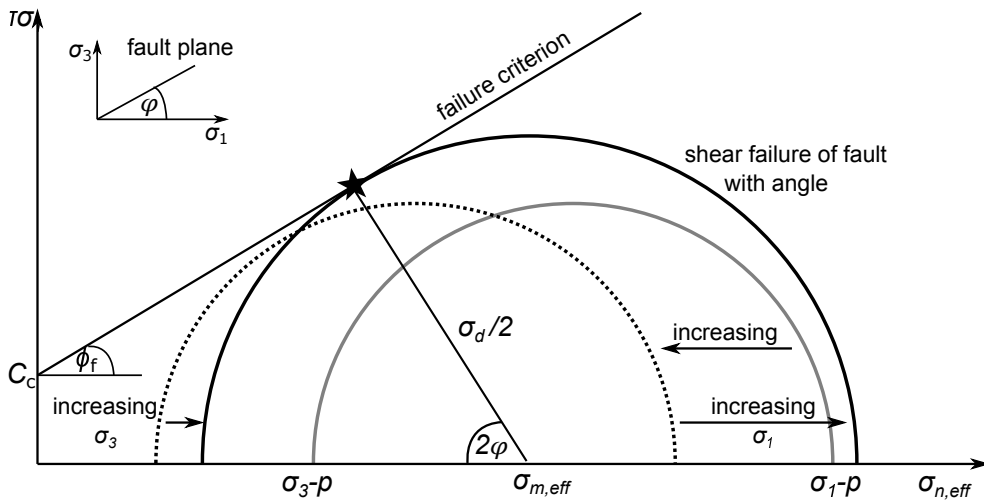


Figure 2.3. Illustration of the Mohr circle and the Coulomb failure criterion. If the circle does not intersect the failure line (grey circle), the stress state of faults with all possible orientations θ to the maximum principal stress (inset) is stable. Such a safe stress state can be perturbed by increasing pore-fluid pressure p (dotted circle) and stress perturbations (solid black circle), moving the circle closer to the failure line. If the changes are sufficiently high, the circle may intersect the failure line in one point (marked by the star) which indicates shear failure of faults with one certain optimal orientation θ .

Considering underground fluid injection, a stable fault (Figure 2.3, grey circle) may be brought closer to failure by an increase of the pressure in the pore space by Δp . This leads to a reduction of the effective principal stresses. While the differential stress remains unaffected by the increasing pore-fluid pressure, the effective mean stress decreases. This results in a shift of the Mohr circle by Δp towards the left, closer to the failure criterion line (Figure 2.3, dotted circle). Physically, this can be interpreted as follows: While compressive normal stresses strengthen a rock mass by pushing its grains together, the fluid within the pore space acts in opposite direction, weakening the rock. *Pore-fluid pressure diffusion*, causing pressure changes in the pore space, is subject of the following section.

Apart from pure pore-fluid pressure perturbations, stress changes may cause failure of pre-existing faults as well. One possible scenario is that σ_1 increases more than σ_3 , resulting in a larger differential stress. If the differential stress increase is sufficiently large, the Mohr circle may touch the failure line in one point (Figure 2.3, black circle), indicating shear failure of the fault with a given, optimal orientation. *Poroelastic stress changes*, which cause the destabilisation of pre-existing faults, are discussed below.

Regarding the 3D space and following Coulomb's theory, the consideration of an intermediate stress σ_2 does not affect the conclusions drawn above. That is, because the Mohr circle that intersects the failure envelope first is the one defined by the maximum and minimum principal stress.

2.3 Pore-Fluid Pressure Diffusion as a Triggering Mechanism

Let us consider high-pressure fluid-injections such as hydraulic fracturing for shale gas production. In such a scenario, a fluid is injected under high pressure into a rather impermeable rock formation (e.g. shale). If the injection pressure is higher than the minimum principal compressive tectonic stress, new fractures will be opened. This increases the in situ permeability of the reservoir, allowing for an easier extraction of the natural gas. Often, these injection operations are accompanied by seismic events.

Shapiro et al. (1997, 1999, 2002) demonstrated that the driving mechanism of seismicity observed during hydraulic fracturing is the diffusional relaxation of a pore-fluid pressure perturbation initiated at the injection well. The pore-fluid pressure diffusion is based on two fundamental equations: Darcy's law and the continuity equation. In the 19th century, the French engineer Henry Darcy conducted experiments involving water flow through sand beds and found an empirical relation relating the fluid filtration velocity q_i to the gradient in pore-fluid pressure $\partial p / \partial x_j$. In its general form, Darcy's law for a homogeneous, isotropic rock volume is defined as (Jaeger et al., 2007; Hummel, 2013; Shapiro, 2015):

$$q_i = -\frac{\kappa}{\eta} \frac{\partial p}{\partial x_i}, \quad (2.14)$$

where κ is the hydraulic permeability of the medium (in m^2) and η the dynamic viscosity of the pore fluid (in Pa s).

The continuity equation that expresses the conservation of fluid mass is given by (Coussy, 2003; Jaeger et al., 2007; Segall, 2010; Shapiro, 2015):

$$\frac{\partial \rho_f \Phi}{\partial t} + \frac{\partial \rho_f q_i}{\partial x_i} = 0. \quad (2.15)$$

Here Φ and ρ_f denote the porosity of the rock and the fluid density, respectively. Assuming that the product $\rho_f \Phi$ is proportional to a pressure perturbation, it can be replaced by $\rho_f \Phi = \rho_0 p S$. Here, S and ρ_0 are the uniaxial storage coefficient (in Pa^{-1}) and a reference fluid density, respectively.

Allowing only small variations of the fluid density ρ_f , it is reasonable to set $\rho_f/\rho_0 \approx 1$ (Coussy, 2003). The combination of equations (2.15) and (2.14) then yields the equation of linear pore-fluid pressure diffusion from a point source through a fluid-saturated, hydraulically homogeneous and isotropic medium:

$$\frac{\partial p}{\partial t} = D \nabla^2 p, \quad (2.16)$$

where D denotes the scalar hydraulic diffusivity (in m^2/s) which is related to the isotropic permeability of the medium κ by $D = \kappa/(\eta S)$. As can be seen from equation (2.16), fluid flow through the pore space of the medium is completely controlled by the hydraulic diffusivity D .

Based on linear pore-fluid pressure diffusion as a primary triggering mechanism of fluid-induced events, Shapiro et al. (1999, 2002) introduced the *seismicity-based reservoir characterization* (SBRC) method. They propose that spatio-temporal features of induced seismicity can be well explained by the assumption of linear fluid-rock interaction. Following the SBRC, estimates of the large-scale hydraulic diffusivity tensor can be found by fitting a so-called *triggering front* to the outermost envelope of a seismic event cloud in a plot showing its spatio-temporal distribution (in the following referred to as $r - t$ -plot). Approximating borehole fluid injections by a source point, $r - t$ -plots show the radial event distance from the source, r , as a function of the event time after the start of the injection, t .

Figure 2.4 illustrates this on the example of a hydraulic fracturing experiment in the Barnett Shale, Texas, U.S. (Hummel, 2013; Hummel and Shapiro, 2013, 2016). Assuming linear pore-fluid pressure diffusion, the triggering front (subscript TF , Figure 2.4, dashed line) is defined in Shapiro et al. (1997, 2002) as:

$$r_{TF} = \sqrt{4\pi D t} \quad (2.17)$$

In case of pressure diffusion through a hydraulically isotropic, homogeneous medium, D denotes the scalar hydraulic diffusivity. If the medium is hydraulically heterogeneous, D is the scalar diffusivity of an effective isotropic, homogeneous medium (Shapiro, 2015).

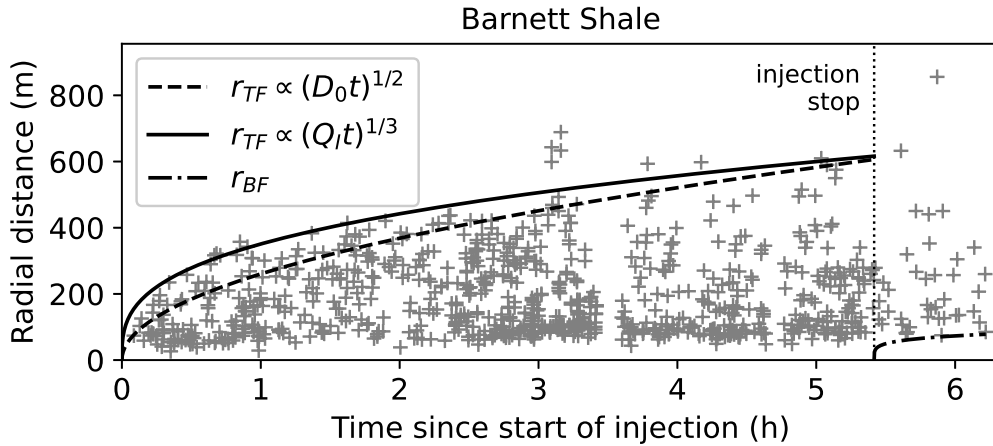


Figure 2.4. The $r-t$ -plot representation of the spatio-temporal evolution of seismicity induced by a hydraulic fracturing operation in the Barnett Shale, Texas, U.S. During 5.4 h of high-pressure fluid injection, numerous seismic events have been recorded. The upper boundary of the evolving seismic event cloud is described by the triggering front. In this case, a cubic root of time-dependent, non-linear diffusion triggering front (bold line, equation (2.21)) captures the spatio-temporal evolution better than a linear diffusion, square root of time-dependent triggering front (dashed line, equation (2.17)). After the termination of the injection, the seismic activity continues and an aseismic domain evolves around the source. The back front forms a lower boundary of the seismic event cloud (dash-dotted line, equation (2.18)).

Recent cases of seismicity at hydraulic fracturing sites revealed that the seismic activity does not terminate with the injection stop at time t_0 but continues in the postinjection phase, also referred to as *postinjection-induced seismicity* (Parotidis et al., 2004; Hummel and Shapiro, 2012). Since the pore-fluid pressure continues to diffuse through the medium even when the injection pressure at the source ceases, locations at greater distances from the source may be destabilised during postinjection times. As soon as a location-dependent pressure maximum has been reached, the pressure at the corresponding location begins to decrease. In turn, the effective stress increases, stabilising the location. It follows that earthquakes can be induced only at locations where the pore-fluid pressure perturbation has not yet reached its local maximum. This leads to the formation of the so-called *back front* of the seismic cloud (subscript BF , Figure 2.4, dash-dotted line). This lower envelope of the seismic cloud describes the aseismic domain which evolves around the source after the injection stop. For a hydraulically isotropic and homogeneous d -dimensional medium, it is described by (Parotidis et al., 2004):

$$r_{BF} = \sqrt{2dDt \left(\frac{t}{t_0} - 1 \right) \ln \frac{t}{t - t_0}}. \quad (2.18)$$

Fitting this function to the lower boundary of the seismic cloud yields also estimates of the diffusivity. With the assumption of linear pore-fluid pressure diffusion, diffusivity estimates obtained for the triggering front (equation (2.17)) and the back front (equation (2.18)) are equal (Hummel and Shapiro, 2012).

Theoretically, the concept of linear pore-fluid pressure diffusion as the main seismicity controlling mechanism is valid for fluid injections into high-permeable rocks. Now, let us take an unconventional shale gas reservoir with an extremely low permeability. In order to facilitate the gas production, fluid flow must be enhanced. This is achieved by hydraulic fracturing which mechanically breaks the rock. Thereby a network of fractures and cracks is created, leading to an enhanced permeability. In such a case, the permeability is no longer constant but pressure-dependent. Since the hydraulic diffusivity and the permeability are directly proportional to each other (see above), a non-linear version of equation (2.16) can be written as (Shapiro and Dinske, 2009; Hummel and Shapiro, 2012):

$$\frac{\partial p}{\partial t} = \nabla D(p) \nabla^2 p, \quad (2.19)$$

where $D(p)$ denotes the pressure dependent diffusivity.

Several approaches have been proposed to account for this pressure dependence (e.g. Gischig and Wiemer, 2013; Miller, 2015; Shapiro and Dinske, 2009; Hummel and Müller, 2009). For this work, the focus is on a power-law-dependent diffusivity as introduced by Shapiro and Dinske (2009):

$$D(p) = (n + 1) D_0 p^n. \quad (2.20)$$

Here, D_0 is a normalising parameter (in $\text{m}^2/(\text{s Pa}^n)$) and n denotes the index of non-linearity (without units). For $n = 0$, $D = D_0$ and equation (2.20) is equal to the linear diffusion equation (equation (2.16)). With increasing n , the diffusivity is controlled more strongly by the pressure.

Using equation (2.20), a general form of the triggering front in a d -dimensional space can be expressed as (Shapiro and Dinske, 2009):

$$r_{TF} \propto (D_0 Q_I^n t^{n+1})^{\frac{1}{d n + 1}}, \quad (2.21)$$

where Q_I is a constant injection rate. For linear diffusion ($n = 0$) through a d -dimensional medium, it follows the already introduced square root of time-dependent triggering front (Shapiro and Dinske, 2009; Hummel and Shapiro, 2012):

$$r_{TF} \propto \sqrt{D_0 t}. \quad (2.22)$$

However, if the diffusivity is strongly controlled by pore pressure ($n \gg 1$) and we assume diffusion through a 3-dimensional medium ($d = 3$), the triggering front is

resolved by a cubic root of time dependence:

$$r_{TF} \propto (QIt)^{\frac{1}{3}}. \quad (2.23)$$

Using microseismic data from hydraulic fracturing operations, as for example in the Barnett Shale, Texas, U.S., previous works demonstrated that such a cubic root of time dependency captures the spatio-temporal evolution of the seismically active zone better than a square root of time-dependent triggering front (Hummel and Shapiro, 2012; Johann et al., 2016, and Figure 2.4, solid line).

The concept of non-linear pore-fluid pressure diffusion, assuming a power-law-dependent hydraulic diffusivity, and the relation for the triggering front (equation (2.21)) can be applied to derive a similar relation for the back front. Such an approach has been developed in Johann et al. (2016) and is described in detail in chapter 3 of this thesis. It can be shown that the following proportionality accurately describes spatio-temporal features of postinjection-induced events:

$$r_{BF} \propto t^{\frac{1}{dn+2}}. \quad (2.24)$$

By fitting this equation to seismic event clouds, estimates of the parameters n and d , controlling the spatio-temporal evolution of the seismic cloud, can be obtained. This contributes to the understanding of postinjection-induced events and can help to improve future fluid injections as well as the seismic risk mitigation.

Overall, the in situ pore-fluid pressure is altered as a result of the spatio-temporal evolution of the pressure perturbation by diffusion. In this case, the failure criterion stress change (equation (2.13)) is given by $\Delta FCS = \sin \varphi \Delta p$. If ΔFCS is large enough, shear failure along pre-existing, favourably oriented faults may occur, resulting in seismic activity. Apart from pore-fluid pressure diffusion as a destabilisation mechanism, poroelastic stress changes may affect the stress state of pre-existing faults. These stress changes will be briefly introduced in the following section and are subject in chapters 4 and 5.

2.4 Poroelastic Stress Changes

As introduced in the previous section, rocks can be considered porous media where the pore space is filled with a fluid such as water, oil or air. Assuming a porous rock mass with fully saturated pores, I considered only the impact of the pore-fluid pressure on the stability of pre-existing fractures so far. However, the system of the solid skeletal frame and the pore fluid may also be considered as a whole. While pressure changes are supported by the pore fluid, elastic stresses are supported by the porous solid. In such a fluid-saturated, porous medium, pore-fluid pressure- and elastic stress changes are coupled. In other words, changes

in stress produce changes in pore pressure and changes in pore pressure produce strains in the porous solid frame (Wang, 2000; Jaeger et al., 2007). If such a coupling is taken into account, changes of the failure criterion stress ΔFCS are influenced not only by changes of the pore-fluid pressure Δp but also by changes of the differential and mean stress, $\Delta\sigma_d$ and $\Delta\sigma_m$, respectively.

The *theory of poroelasticity* deals with such a fluid-to-solid coupling. Its fundamentals were found by the Belgian-American physicist Maurice Biot (Biot, 1941) but further discussed and reformulated by e.g. Geertsma (1966); Rice and Cleary (1976); Rudnicki (1986); Detournay and Cheng (1993); Wang (2000). The constitutive equations necessary to solve for pressure- and stress changes in a poroelastic, fluid-saturated, isotropic medium, are briefly introduced in the following paragraphs.

In general, four variables are necessary for the solution of a poroelastic problem; two mechanical quantities, stress σ_{ij} and strain ϵ_{ij} , and two hydraulic quantities, pore-fluid pressure p and the dilatational characteristic of the pore space χ that represents the volumetric deformation of the pore space due to additional fluid mass. Two equations describe the connection between the four constitutive variables (see chapter 2 in Shapiro, 2015, for a detailed description): Hooke's law for elastically isotropic, fluid-saturated media and a relation between the pore-fluid pressure and the dilatation of the medium. In case of poroelastic coupling, Hooke's law is given by (e.g. Shapiro, 2015):

$$\sigma_{ij} = 2G\epsilon_{ij} + \lambda\delta_{ij}\epsilon - \alpha p\delta_{ij}, \quad (2.25)$$

where α is the Biot-Willis coefficient (Biot, 1962), playing the role of an effective stress coefficient. It is defined as $\alpha = 1 - K/K_{gr}$, where K and K_{gr} are the bulk moduli of the drained rock matrix and its grain material, respectively. α takes on values between Φ and 1. Whereas it may be as low as 0.1 to 0.4 for low porous rocks, it may be higher than 0.5 for rocks with high porosity, and close to 1 for rather soft rocks (Shapiro, 2015, 2018). Applying a double-dot product to equation (2.25) yields:

$$\epsilon = \frac{1}{K} \left(\frac{1}{3}\sigma_{ij} + \alpha p \right). \quad (2.26)$$

Furthermore, the pore-fluid pressure and the dilatation of an isotropic medium are directly proportional (Jaeger et al., 2007; Shapiro, 2015):

$$p = M(\chi - \alpha\epsilon). \quad (2.27)$$

In this equation, M denotes the Biot modulus (Detournay and Cheng, 1993), defined as $M = (\Phi/K_f + (\alpha - \Phi)/K_{gr})^{-1}$. Equations (2.26) and (2.27) demonstrate that from the four constitutive quantities, only two variables are independent.

To solve for poroelastic problems, a quasi-static approximation of linear poroelasticity has been developed (Rice and Cleary, 1976; Rudnicki, 1986; Detournay and Cheng, 1993). Here, it is assumed that mechanical equilibrium is attained (almost) instantaneously after changes in pressure and stress (Wang, 2000).

The description of such a poroelastic problem (neglecting initial stresses and pore-fluid pressure) is based on three equations (Wang, 2000; Shapiro, 2015): Darcy's law (equation (2.14)), which relates the stationary filtration of the pore-fluid pressure in the pore space; the continuity equation (equation (2.15)), which may also be expressed in terms of the volumetric change of the pore space volume due to influent or effluent fluid mass given by the quantity χ (Jaeger et al., 2007; Shapiro, 2015):

$$\frac{\partial \chi}{\partial t} + \frac{\partial q_i}{\partial x_i} = 0; \quad (2.28)$$

and the stress equilibrium equation (equation (2.7)).

Using these three equations and assuming an elastically and hydraulically isotropic and homogeneous, fluid-saturated poroelastic medium, the two constitutive equations can be written as (Shapiro, 2015):

$$\frac{\kappa}{\eta} \nabla^2 (M(\chi - \alpha \epsilon)) = \frac{\partial \chi}{\partial t}, \quad (2.29)$$

$$(\lambda_{dr} + M\alpha^2) \frac{\partial \epsilon}{\partial x_i} - \alpha M \frac{\partial \chi}{\partial x_i} + 2\mu_{dr} \frac{\partial \epsilon_{ij}}{\partial x_j} = 0. \quad (2.30)$$

Combining different equations, equivalent forms of relations (2.29) and (2.30) can be found (Jaeger et al., 2007; Shapiro, 2015). Using the pore-fluid pressure and the displacement field as constitutive variables, for example, and inserting equation (2.27) in equation (2.29) yields a mixed form of the diffusion equation with an additional term for the poroelastic coupling (Jaeger et al., 2007):

$$\frac{\kappa M}{\eta} \nabla^2 p = \frac{\partial p}{\partial t} + \alpha M \frac{\partial \epsilon}{\partial t}. \quad (2.31)$$

Here, $\alpha M \partial \epsilon / \partial t$ represents the influence of the poroelastic coupling.

In a recent work, Shapiro (2015) introduced the so-called poroelastic stress coefficient n_S which gives an estimate of the strength of the poroelastic coupling. It is given by $n_S = \alpha(1 - 2\nu)/2(1 - \nu) = \alpha G/(\lambda + 2G)$. Generally speaking, the higher the value of n_S , the larger the influence of the poroelastic coupling. Consider a rather incompressible, low-permeable rock with $\nu \geq 0.3$ (e.g. shale). In this case, the poroelastic stress coefficient may be below 0.2. If the rock additionally has a low porosity, ν may even be smaller than 0.1. In turn, a highly porous, compressible rock (e.g. sandstone) with a Poisson's ratio of around 0.2

and a Biot coefficient α close to one may have a poroelastic stress coefficient higher than 0.35 (Shapiro, 2018).

It can therefore be assumed that poroelastic coupling can be neglected in case of earthquakes associated with high-pressure fluid injections that typically occur in low porous and incompressible rocks (e.g. shales or granite). Accordingly, the work presented in chapter 3 is based purely on pure pore-fluid pressure diffusion through a porous medium.

In contrast, wastewater-induced earthquakes in the central U.S. are linked to massive fluid disposal into a highly porous aquifer and occur in a strongly fractured crystalline basement. Poroelastic stress changes may thus play an important role in explaining the observed seismicity. Additionally, events in the central U.S. frequently occur at large distances from high-volume disposal wells (Weingarten et al., 2015; Goebel et al., 2017; Peterie et al., 2018). Since the transmission of stress changes is not limited by the permeability of the rock, this may be another indication for poroelastic fluid-rock interaction (Goebel et al., 2017). Thus, I complement the thesis with two works on wastewater-induced seismicity where I also account for poroelastic stress changes (chapters 4 and 5). Whereas the focus of chapter 4 is on earthquakes observed in Oklahoma throughout the period May 2013 to November 2016 that occur directly below a high-volume disposal area and seem to migrate to greater depth with time, chapter 5 concentrates on earthquakes in Kansas where the seismically active area shifts away from disposal wells in horizontal direction with time.

Table 2.1. Compilation of typical hydraulic and poroelastic parameters for different rock types. Note that the listed values are merely supposed to give approximate realistic ranges. Usually, the parameters strongly depend on stress conditions and measurement techniques (see e.g. Detournay and Cheng, 1993).

Rock	porosity Φ (-)	permeability κ (m^2)	Biot coefficient α (-)
sandstone	0.16–0.24*	10^{-17} – $10^{-11}\ddagger$	0.65–0.85 \ddagger
granite	0.01–0.02 \dagger	10^{-20} – $10^{-16}\ddagger$	0.27–0.47 \ddagger
limestone	0.04–0.29 \dagger	10^{-22} – $10^{-12}\ddagger$	0.69–0.71**
shale	< 0.1 ^a	10^{-23} – $10^{-16}\ddagger$	0.1–0.4 \parallel

Reference

* Nur et al. (1980)

** Wang (2000)

\dagger Coussy (2003)

\ddagger Jaeger et al. (2007)

\parallel Shapiro (2018)

^a Todd (1964)

CHAPTER 3

Scaling of Seismicity Induced by Nonlinear Fluid-Rock Interaction after an Injection Stop¹

Key Points:

- Derivation of a novel scaling law for the back front and the triggering front of postinjection-induced seismicity.
- The spatio-temporal evolution of the seismic cloud is sensitive to the non-linearity of pore-fluid pressure diffusion and the Euclidean dimension of the seismically active zone.
- Numerical modelling verified the novel relations, allowing for a successful application to case studies of high-pressure fluid injections to estimate the two governing parameters.

¹ This article has been published in *Journal of Geophysical Research: Solid Earth*: L. Johann, C. Dinske and S. A. Shapiro (2016). Scaling of seismicity induced by nonlinear fluid-rock interaction after an injection stop. DOI: <https://doi.org/10.1002/2016JB012949>. Published by the American Geophysical Union (AGU). All Rights Reserved. Please note the error in equation (18): The left and right part of the equation are correct, however the middle part has to be removed.

RESEARCH ARTICLE

10.1002/2016JB012949

Key Points:

- Derivation of a novel scaling law for the back front and triggering front of postinjection-induced seismicity
- Back front and triggering front are sensitive to nonlinearity and the Euclidean dimension of the seismic cloud
- Modeling and testing of the scaling laws for case studies including propped stimulated domains

Correspondence to:

L. Johann,
lisajohann@zedat.fu-berlin.de

Citation:

Johann, L., C. Dinske, and S. A. Shapiro (2016), Scaling of seismicity induced by nonlinear fluid-rock interaction after an injection stop, *J. Geophys. Res. Solid Earth*, 121, 8154–8174, doi:10.1002/2016JB012949.

Received 24 FEB 2016

Accepted 3 NOV 2016

Accepted article online 8 NOV 2016

Published online 18 NOV 2016

Scaling of seismicity induced by nonlinear fluid-rock interaction after an injection stop

L. Johann¹, C. Dinske¹, and S. A. Shapiro¹¹Institute of Geophysics, Freie Universitaet Berlin, Berlin, Germany

Abstract Fluid injections into unconventional reservoirs, performed for fluid-mobility enhancement, are accompanied by microseismic activity also after the injection. Previous studies revealed that the triggering of seismic events can be effectively described by nonlinear diffusion of pore fluid pressure perturbations where the hydraulic diffusivity becomes pressure dependent. The spatiotemporal distribution of postinjection-induced microseismicity has two important features: the triggering front, corresponding to early and distant events, and the back front, representing the time-dependent spatial envelope of the growing seismic quiescence zone. Here for the first time, we describe analytically the temporal behavior of these two fronts after the injection stop in the case of nonlinear pore fluid pressure diffusion. We propose a scaling law for the fronts and show that they are sensitive to the degree of nonlinearity and to the Euclidean dimension of the dominant growth of seismicity clouds. To validate the theoretical finding, we numerically model nonlinear pore fluid pressure diffusion and generate synthetic catalogs of seismicity. Additionally, we apply the new scaling relation to several case studies of injection-induced seismicity. The derived scaling laws describe well synthetic and real data.

1. Introduction

Caused by the world's increasing energy demand, the exploitation of unconventional hydrocarbon reservoirs and operation of geothermal systems has become a large issue within the last decade. To enhance hydraulic transport properties, pressurized fluids are injected into the reservoir.

Although the nature of fluid migration in the subsurface, particularly during hydraulic fracturing, is still poorly understood, it is known that borehole fluid injections are often accompanied by microseismicity [see, e.g., Healy *et al.*, 1968; Raleigh *et al.*, 1972, 1976]. Analyzing spatiotemporal distributions of the observed seismic events, hydraulic transport properties of the reservoir rock can be characterized [see Shapiro, 2015].

In recent years, many studies have been conducted in order to describe fundamental processes that lead to microseismicity associated with reservoir activity. On the one hand, seismic events are observed during the production of hydrocarbons or of fluids at Enhanced Geothermal Systems (EGS) [e.g., Segall, 1989; Grasso, 1992; Zoback and Zinke, 2002; Majer *et al.*, 2007; Van Wees *et al.*, 2014]. On the other hand, the injection of fluids, as, for example, at geothermal sites or during hydraulic fracturing of hydrocarbon reservoirs, very frequently causes seismicity [Raleigh *et al.*, 1972; Zoback and Harjes, 1997; Baisch and Vörös, 2010; Ellsworth, 2013].

Early tests to understand the behavior of rocks at high stresses were performed by Griggs [1936], who also invented the so-called Griggs apparatus to study the deformation of a rocks sample under high pressure. Terzaghi [1936] was the first one to propose that rock failure is controlled by an effective stress, given by the principal stresses minus the pore fluid pressure. Paterson and Wong [2005] studied the strength of rocks under the influence of stress and pore fluid pressure further. They conducted triaxial laboratory experiments which reveal that shear failure can be predicted by using the Mohr-Coulomb failure criterion in the principal coordinate system.

Following Terzaghi's concept of effective stresses [Terzaghi, 1936], Talwani and Acree [1984] and Zoback and Harjes [1997] proposed that pore fluid pressure artificially increases in the reservoir as a result of the injection. This leads to a decrease of the effective normal stress, which might cause sliding along already critically stressed preexisting favorably oriented cracks and fractures.

According to *Langenbruch and Shapiro* [2014], the stress distribution in elastically heterogeneous and fractured rock masses can be highly heterogeneous. However, all its principal components are dominantly (and nearly equally) modified by the diffusion of pore fluid pressure p .

In turn, an anisotropic distribution of p is mainly caused by an anisotropic permeability of the rock. The spatiotemporal evolution of microseismicity is generally controlled by such an anisotropic nature. Given microseismic event locations, *Shapiro et al.* [1999] and *Hummel and Shapiro* [2013, 2016] attempted to estimate the permeability anisotropy by solving an inverse problem. To account for the hydraulic anisotropy in real data examples, we later use an effective isotropic medium transformation (see section 4) [*Hummel*, 2013].

Seismicity during extraction and production is understood to be linked to a modification of normal and shear stresses which act on preexisting faults [*Majer et al.*, 2007; *Suckale*, 2009]. The focus in this study will be only on injection-induced seismicity.

Since the number of works on injection-induced seismicity has increased within the last years, many competing ideas on seismicity-controlling processes have developed. *Healy et al.* [1968] were the first to directly link the spatiotemporal distribution of observed microseismicity during waste water injection at the Rocky Mountain Arsenal, USA, with the fluid injection. They assume that rocks contain a number of favorably oriented critically stressed fractures and cracks which can be reactivated by increasing pressures. Thus, they consider the reduction of the frictional strength of preexisting cracks and fractures by increasing pore fluid pressures to be the fundamental mechanism for seismicity.

Hsieh and Bredehoeft [1995] quantitatively studied the waste water injection at the Rocky Mountain Arsenal, USA, further. The authors show that the pressure buildup along the reservoir coincides with the spatial distribution of microseismic locations. Thus, *Hsieh and Bredehoeft* [1995] propose that seismicity is likely to be induced by the increased pore fluid pressure as already noted by *Healy et al.* [1968].

On the basis of comprehensive seismic monitoring of reservoir-induced seismicity in South Carolina, USA, *Talwani and Acree* [1984] suggest that the diffusion of pore fluid pressure plays a major role for the spatiotemporal distribution of microseismic events during fluid injections. They assume that seismicity mainly occurred on critically stressed preexisting fractures. With that idea they follow previous works as mentioned above. Furthermore, they use the spatiotemporal distribution of epicenters to get estimates of the hydraulic diffusivity.

The aforementioned works do not consider poroelastic effects as described in the pioneering work by *Biot* [1941], i.e., that a change of pore fluid pressure induces stresses, which in turn cause changes in pore fluid pressure. *Rutqvist et al.* [2008] performed a poroelastic analysis of reservoir-geomechanical modeling for tensile and shear failure at a CO₂ storage system. They show that the total horizontal compressive stress increases as a result of the injection, while total vertical stresses do not change significantly.

A poroelasticity-based study by *Rozhko* [2010] (see also discussion by *Shapiro* [2012]) revealed that shear stress changes can become larger than pore fluid pressure changes at locations far from the injection source.

Segall and Lu [2015] and *Chang and Segall* [2016] further examined processes that control fluid injection-induced seismicity. They show that pore fluid pressures predicted by a poroelastic model are larger than those predicted by pure diffusion models. Yet the pressure distribution strongly depends on the in situ stress regime of the reservoir. Moreover, they show that induced stresses can have a significant impact on injection-related seismicity, especially at large distances from the source.

However, poroelastic coupling parameters such as the Biot coefficient α used in the aforementioned studies are relatively high (e.g., $\alpha \geq 0.3$). These values are too high for situations in which fluids are injected into a rock formation which is characterized by initially isolated pores and nearly negligible permeability of the rock matrix. In such a situation, α is significantly smaller than previously reported values. As shown in chapters 2.9.5 and 3.4 in *Shapiro* [2015], the strength of the poroelastic stress coupling, controlled by parameter $n_s = \alpha n'$ [*Shapiro*, 2015, equation 2.277 with 2.278], with $\alpha \leq 0.3$ results in pore fluid pressure perturbations which dominate shear stress perturbations. Since the modeling performed in this study is based on a hydraulic fracturing treatment of a shale gas reservoir, we here neglect poroelastic coupling effects. Our study follows many other works [e.g., *Talwani and Acree*, 1984; *Shapiro et al.*, 1997, 1999; *King et al.*, 2016], by accepting the mechanism of pore fluid pressure diffusion as the underlying process of fluid-induced seismicity. Such a simplified model corresponds to a poroelastic analysis for situations with small α . This limit is fundamental for understanding

triggering processes as well. Below we provide an analytic solution for this case. Such a solution can be especially significant for situations where multiparameter description is possible and dominance of various effects is not clear. An analytical solution can then be used as an orientation to understand contribution of different phenomena, especially in future nonlinear poroelastic coupled models.

Based on the assumption of solely pore fluid pressure diffusion, *Shapiro et al.* [1997, 1999, 2002] developed a method for the determination of the hydraulic diffusivity D of the medium, known as the seismicity-based reservoir characterization. This approach spatiotemporally analyzes the distribution of microseismicity induced during the injection. Yet seismic activity is not restricted to the injection phase but occurs also after the termination of the fluid injection. *Parotidis et al.* [2004] studied this phenomenon further and observed an aseismic domain which evolves in time and space around the injection source after the injection stop at time $t = t_0$. The authors first introduced and analytically described the back front of seismicity, which can also be used for the quantification of hydraulic reservoir properties. Their description is based on the linear differential equation for pore fluid pressure diffusion.

All studies mentioned above [*Rutqvist et al.*, 2008; *Rozhko*, 2010; *Segall and Lu*, 2015; *Chang and Segall*, 2016] addressed linear effects only. This is an important feature of the corresponding poroelastic models. In many situations, the spatiotemporal distribution of seismicity is not captured by linear pore fluid pressure diffusion. One example is hydraulic fracturing, where hydraulic transport properties are significantly enhanced and become a function of pore fluid pressure. This observation correlates well with the understanding of hydraulic rock properties to be dependent on the effective stress. Numerous works, e.g., by *Katsube et al.* [1991], *Berryman* [1992], *Detournay and Alexander* [1993], *Al-Wardy and Zimmerman* [2004], *Li et al.* [2009], and *Shapiro et al.* [2015] show that hydraulic rock parameters such as the permeability can be strongly influenced by pore fluid pressure. Enhanced pore fluid pressure increases the size of pores. This effect may lead to a rather nonlinear pore fluid pressure diffusion process. In other words, the differential diffusion equation, effectively describing the process of pore fluid pressure perturbation, becomes strongly nonlinear.

To understand seismicity induced by nonlinear diffusion of pore fluid pressure, much work has recently been done [*Rice*, 1992; *Miller et al.*, 2004; *Shapiro and Dinske*, 2009; *Dinske*, 2010; *Hummel and Shapiro*, 2012; *Gischig and Wiemer*, 2013]. *Shapiro and Dinske* [2009] as well as *Hummel and Shapiro* [2012] found scaling relations for the triggering front of seismicity induced during the injection by nonlinear diffusion of pore fluid pressure for different sets of boundary conditions. These help to understand the controlling parameters and can be used for large-scale diffusivity estimates of the reservoir.

In this paper, we assume the pore fluid pressure perturbation as the triggering mechanism. We use the previously obtained results for rather general cases of nonlinear pore fluid pressure diffusion [see, e.g., *Shapiro and Dinske*, 2009; *Shapiro*, 2015] and formulate the front behavior for the postinjection-induced seismicity. We derive a novel theoretical scaling relation for the back front but also for the triggering front of seismicity after the injection stop. To verify the theoretical finding, comprehensive 3-D modeling of nonlinear pore fluid pressure diffusion is carried out. For this purpose, we generate catalogs of synthetic seismicity. We examine the spatiotemporal distribution of synthetic seismicity induced during as well as after the injection termination and compare observed scaling relations for the back front to theoretical values predicted by the novel scaling law. Additionally, we apply the theoretical relation to back front signatures of different hydraulic fracturing and Enhanced Geothermal System (EGS) case studies taken from literature. We show that the derived scaling law works well for real data. Therefore, the methodology can be used for further reservoir characterization, understanding of hydraulic fracturing processes as well as hazard assessment.

2. Theoretical Background

2.1. Linear Pore Fluid Pressure Diffusion

Fluid injections into the subsurface are frequently accompanied by microseismic activity. A probable triggering mechanism of observed microseismicity is the diffusion of pore fluid pressure. Approximating the fluid injection by a point source of pressure perturbation into an infinite hydraulically homogeneous and isotropic poroelastic fluid-saturated medium, the spatiotemporal evolution of the pore fluid pressure perturbation p can be found in Biot's equations. According to *Shapiro et al.* [1997, 1999, 2002], the diffusion equation for the low-frequency range can be expressed by

$$\frac{\partial p}{\partial t} = \nabla(D\nabla p), \quad (1)$$

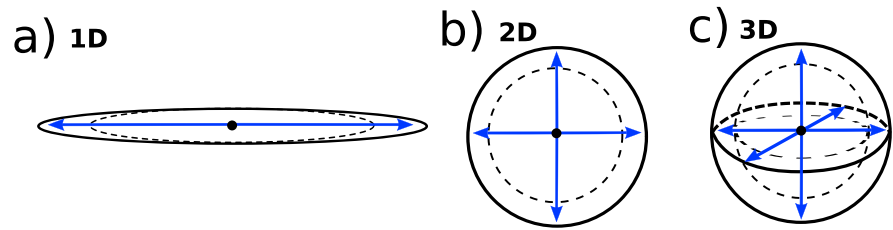


Figure 1. Euclidean dimensions of diffusion. (a) One-dimensional diffusion describes the diffusion along a typical hydraulic fracture and results in seismic clouds which occur on or in vicinity of this fracture. (b) The 2-D case indicates that the diffusion occurred in a plane, yielding a two-dimensional event distribution. (c) In 3-D, a hydraulic fracture interacts with a preexisting fracture network, which gives seismic events in 3-D space.

with the time t , pore fluid pressure p , and the scalar hydraulic diffusivity D , which is assumed to be constant in time and independent of pressure.

Dependent on the local stress field, mechanical and hydrological rock properties, and the injection pressure strength, the diffusion of pore fluid pressure can effectively occur in one, two, or three dimensions as shown in Figure 1. While the 1-D case describes the diffusion of pore fluid pressure along a typical hydraulic fracture, the two-dimensional example is valid for diffusion in a plane. In contrast, three-dimensional diffusion occurs in the case of the pressure perturbation propagating in a complex fracture network, for example, either opening of preexisting cracks and pores or new cracks and pores. Later, we address the 1-D, 2-D, and 3-D scenarios in more detail.

Shapiro *et al.* [1997, 1999, 2002] use the spatiotemporal event distribution for the characterization of the scalar hydraulic diffusivity D of a hydraulically effective isotropic medium. In r - t plots, where the radial event distance from the injection source r is plotted versus the event occurrence time t , the triggering front of seismicity can be found as an envelope of the seismic cloud. For an isotropic and homogeneous medium it is approximately given by the heuristic relation:

$$r_{tf} = \sqrt{4\pi Dt}. \tag{2}$$

The parameter D is directly related to the permeability k by $D = k/(\mu S)$. Here μ is the dynamic viscosity of the fluid and S denotes the storage coefficient defined by Jaeger *et al.* [2007, p. 188] which combines the porosity and different rock bulk moduli. Whereas most sandstones have permeabilities within the range of 10^{-16} to 10^{-12} m², the permeability of shales is usually much lower with values between 10^{-21} m² and 10^{-18} m² [Hummel, 2013].

Since fluid-induced seismicity is also observed after the injection stop, Parotidis *et al.* [2004] include spatiotemporal characteristics of postinjection-induced seismicity in reservoir characterization, specifically to get estimates of the hydraulic diffusivity D . As the study shown in this paper is only valid for injection-induced seismicity (see also section 1), we do not consider production-induced events which are associated with different physical mechanisms, namely, poroelastic stress changes [see, e.g., Segall, 1989; Grasso, 1992; Zoback and Zinke, 2002; Majer *et al.*, 2007; Baisch and Vörös, 2010; Van Wees *et al.*, 2014].

On the assumption that seismicity occurs only for increasing pore fluid pressures, an aseismic domain, evolving around the source after the pressure has reached its local maximum and $\frac{\partial p}{\partial t} \leq 0$, can be defined. Parotidis *et al.* [2004] documented observations on this domain. They call the lower (smaller-distance) boundary of postinjection-induced seismicity the back front of seismicity. For a hydraulically homogeneous and isotropic medium and a constant-rate fluid injection until $t = t_0$, Parotidis *et al.* [2004] used the analytical solution of the pressure distribution as given by Carslaw and Jaeger [1959] for event distances r at times $t > t_0$. In such a case, the lower boundary of seismicity can be described by the following exact result:

$$r_{bf} = \sqrt{2dDt \left(\frac{t}{t_0} - 1 \right) \ln \left(\frac{t}{t - t_0} \right)}. \tag{3}$$

Again, D is the hydraulic diffusivity of the rock and d is the Euclidean dimension of the space of seismic cloud dominant growth, influenced by the dimension of pore fluid pressure diffusion (Figure 1). The value for d is taken from the spatiotemporal distribution of seismic events. It is $d = 3$ for a 3-D cloud, $d = 2$ for a 2-D case,

i.e., a seismicity cloud evolving in time predominantly on a plane, and $d = 1$ for a 1-D case, i.e., seismicity occurring predominantly along a line or a thin spatial band. Fitting equations (2) and (3) to the seismic cloud yields estimates of the medium hydraulic diffusivity D . Given that seismicity is induced by linear pore fluid pressure diffusion in a hydraulically homogeneous medium, the values of D in equations (2) and (3) will coincide [see, e.g., Parotidis et al., 2004; Hummel and Shapiro, 2016].

2.2. Nonlinear Pore Fluid Pressure Diffusion

In many situations, the diffusivity becomes a function of pore fluid pressure. This is always the case for hydraulic stimulations of reservoirs. High fluid pressure (comparable to or higher than the minimum principal stress σ_3) acts against the normal stress and increases apertures of pores and fractures. This leads to a strong enhancement of permeability and has been described and discussed in previous works [see, e.g., Shapiro and Dinske, 2009; Hummel and Shapiro, 2012; Gischig and Wiemer, 2013; Miller, 2015]. Approximating the fluid injection by a point source switched on at $t = 0$ s and neglecting hydraulic anisotropy and heterogeneity, the following general differential equation of diffusion can be derived for a d -dimensional space [Shapiro and Dinske, 2009]:

$$\frac{\partial p}{\partial t} = \nabla(D(p)\nabla p). \quad (4)$$

This equation describes the perturbation of pore fluid pressure in time and space, controlled by a pressure-dependent diffusivity $D(p)$. It can be applied for diffusion in 1-D, 2-D, and 3-D (see also Figure 1).

Later, we numerically model a 3-D diffusion scenario where the seismicity is induced by the pore fluid pressure diffusion. In contrast, our analytical results are valid for 1-D, 2-D, and 3-D geometries of a hydraulic stimulation (see Figure 1). In this case, the diffusion equation (equation (4)) describes pore fluid pressure perturbation propagating along a hydraulic-fractured domain. Due to pore fluid pressure perturbation and coupled stress changes in the surrounding rocks caused by the fracturing, seismic events are induced parallel to this propagating pressure perturbation, inside and behind the boundaries of the fractured domain.

To account for the pressure dependence, Shapiro and Dinske [2009] propose the following power law for the diffusivity [see also Shapiro et al., 2015]

$$D(p) = (n + 1)D_0p^n, \quad (5)$$

where $D(p) = D(p(x, y, z, t))$. Thus, the diffusivity depends on pore fluid pressure p , which in turn is a function of location (x, y, z) and time t . Correspondingly, also, D is a function of location and time. Furthermore, n is the index of nonlinearity which describes the influence of nonlinear pore fluid pressure diffusion on transport properties. It may depend on reservoir properties such as lithology and pore space geometry. D_0 is a scaling parameter with unit $\text{m}^2/(\text{s Pa}^n)$, and $(n + 1)$ is an integration factor. While $n = 0$ describes the linear diffusion case, the diffusivity will strongly depend on pressure for large n . Since we consider the diffusion of pore fluid pressure as the seismicity controlling triggering mechanism, p is the changing variable and the tectonic stress remains almost unaffected. Thus, the effective normal stress is modified predominantly by p . Here we neglect poroelastic coupling of stress and pressure, which is an acceptable approximation in tight rocks (see section 1) [Shapiro, 2015, chap. 2].

If pore fluid pressure diffusion is controlled by nonlinear fluid-rock interaction, linear diffusion triggering front and back front (equations (2) and (3)), respectively) do not adequately describe the temporal behavior of the seismic cloud. Rather, equations (2) and (3) can be used to obtain heuristic effective diffusivity estimates D_h [Hummel and Shapiro, 2016]. If diffusion is controlled by a highly nonlinear process, $D_{h,tf}$ for the triggering front and $D_{h,bf}$ for the back front no longer coincide.

To determine the actual temporal dependence of the seismicity induced during as well as after the injection, we recall that we assume a power law dependence of the diffusivity. Power law functions are also possible simple fits to the seismic envelope [see, e.g., Hummel and Shapiro, 2012, 2016]. They can be empirically applied according to

$$r_{tf} = At^x \quad (6)$$

for the triggering front and

$$r_{bf} = B(t - t_0)^\psi \quad (7)$$

for the back front of seismicity. Later, we show that the power laws are indeed theoretically justified.

The parameters A, B , and χ, ψ are determined by a fit of functions (6) and (7) to the upper and lower boundaries of seismic clouds in corresponding r - t plots, respectively.

Shapiro and Dinske [2009] and *Hummel and Shapiro* [2012] demonstrate that the parameter χ takes values between $1/3$ and $1/2$. While a value of $\chi = 1/2$ indicates linear fluid-rock interaction, the lower limit of $\chi = 1/3$ is obtained for seismicity induced by very strong nonlinear diffusion ($n \rightarrow \infty$) of pore fluid pressure in 3-D media. In contrast, for the back front, $\psi \approx 1/3$ in case of linear pore fluid pressure diffusion, but it is significantly smaller than $1/3$ for nonlinear pore fluid pressure diffusion [*Hummel and Shapiro*, 2016].

2.3. Scaling of the Triggering Front

Shapiro and Dinske [2009] found the parameters that control the temporal behavior of the triggering front by deriving a scaling law for times t before the injection stop at t_0 . They assumed initially homogeneous and isotropic rocks and considered simplifications of equation (4) for a radially symmetric d -dimensional geometry with the diffusivity model formulated by equation (5) [see also *Shapiro*, 2015, equation (4.22)]

$$\frac{\partial r^{d-1} p}{\partial t} = D_0 \frac{\partial}{\partial r} r^{d-1} \frac{\partial}{\partial r} p^{n+1}. \tag{8}$$

Q_0 is a normalizing coefficient defining the fluid injection rate $Q_i(t)$ [*Shapiro*, 2015, p. 185]:

$$Q_i(t) = S(i + 1)A_d Q_0 t^i. \tag{9}$$

In this equation, S is the storage coefficient and A_d will take values of $4\pi, 2\pi h$, and $2A_r$ for a d -dimensional space of $d = 3, 2$, or 1 , respectively. h is the height of a hypothetical homogeneous plane layer for a cylindrically symmetric injection source ($d = 2$), and A_r denotes the cross section of a hypothetical infinite straight rod ($d = 1$). The parameter i depends on the injection source. It is $i = -1$ for a delta-like, instantaneous injection of a finite fluid volume and $i = 0$ in case of a constant injection rate. For a linearly with time increasing injection rate $i = 1$, which results in parabolic cumulative injected volume with time. For illustration of the injection source, see Figure 2.

Shapiro and Dinske [2009] show for the formulation of $Q_i(t)$ (equation (9)) that the mass conservation law leads to the following simple constraints [*Shapiro*, 2015, equation (4.23)]:

$$\int_0^\infty r^{d-1} p(t, r) dr = Q_0 t^{i+1}. \tag{10}$$

This is an expression of the fact that the volume integral of the pore fluid pressure perturbation during an injection is proportional to the injected fluid volume. Using the conditions above, the authors performed a dimensional analysis of the quantities r, t, D_0 , and Q_0 which influence the pressure perturbation [see also *Shapiro*, 2015, equations (4.22)–(4.23)]. The dimensions are given by $[r] = L, [t] = T, [D_0] = \frac{L^2}{TP^n}$, and $[Q_0] = \frac{PL^d}{T^{i+1}}$. From these quantities, only one dimensionless combination θ can be found. It is given by

$$\theta = r \left(D_0 Q_0^n t^{n(i+1)+1} \right)^{\frac{-1}{(dn+2)}}. \tag{11}$$

A combination of the quantities in equation (11) yields the dimension of pressure $p = [P]$:

$$\left(\frac{Q_0^2}{D_0^d t^{d-2i-2}} \right)^{\frac{1}{(dn+2)}} \tag{12}$$

Following the Π theorem as defined in *Barenblatt* [1996], a description of pressure can then be formulated as follows:

$$p(t, r) = \left(\frac{Q_0^2}{D_0^d t^{d-2i-2}} \right)^{1/(dn+2)} \Phi(\theta). \tag{13}$$

Here $\Phi(\theta)$ is a dimensionless function found by substituting (5) and (13) into (8) and (10) and applying the boundary condition $p = 0$ Pa for $t < 0$ s [see *Shapiro*, 2015, equations (4.36)–(4.37)].

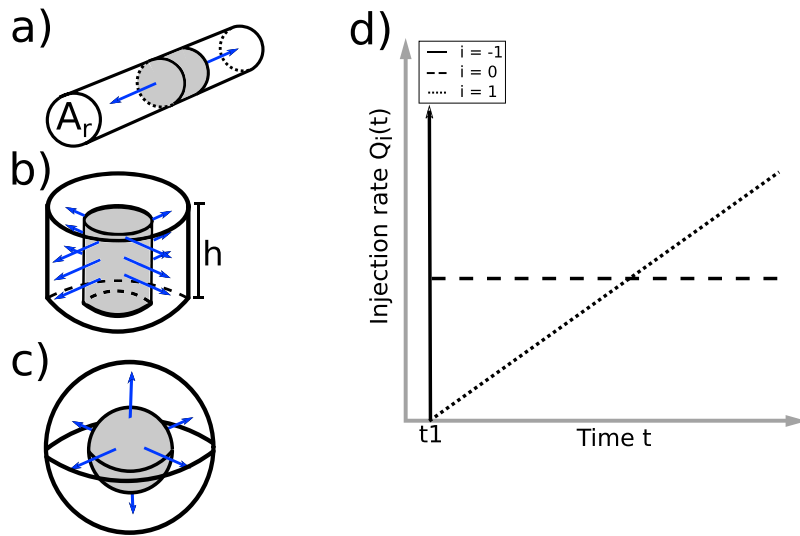


Figure 2. (a–c) The 1-D, 2-D, and 3-D injection scenarios. (d) The different geometries influence the injection rate $Q(t) = S(i + 1)A_d Q_0 t^i$, where i denotes the injection type. It is $i = -1$ for an instantaneous injection of a finite volume of fluid, $i = 0$ for a constant injection, and $i = 1$ for an increasing injection rate. A_d takes values of $2A_r$, $2\pi h$, and 4π for $d = 1, 2$, and 3 , respectively. Q_0 is a scaling parameter, and S is the storage coefficient. Visualized are functions for $i = -1, 0$, and 1 (solid, dashed, and dotted lines, respectively).

Further, rearranging (11) yields a general proportionality for the triggering front

$$r_{tf} \propto (D_0 Q_0^n t^{n(i+1)+1})^{\frac{1}{(dn+2)}}. \tag{14}$$

Additionally, *Hummel and Shapiro* [2012] investigate triggering front signatures for a constant injection pressure source ($i = 0$). Their results show that χ in equation (6) is very well described by $\chi = (n + 1)/(dn + 2)$, what is in agreement with equation 14.

2.4. Scaling of Postinjection-Induced Seismicity

To understand the nature of postinjection-induced seismicity, we derive a novel scaling law for the back front of seismicity.

Let us assume that the observation time is significantly longer than the injection period. Then, we can further use the scaling laws introduced by *Shapiro and Dinske* [2009] for our theoretical derivation of the back front scaling law. For this we accept the assumption of an instantaneous injection of a finite fluid volume (i.e., $i = -1$). This permits to avoid consideration of a second time which corresponds to the instantaneous termination of the fluid injection, t_0 . Furthermore, we take into account that the injection source corresponds to a point-like source at the radial distance $r = 0$ m. In this way, we will obtain asymptotic long time limit scaling laws for the triggering and back fronts, which can then be applied to real data examples of fluid-induced seismicity.

Under the above mentioned assumptions of $i = -1$ and a point-like (in d -dimensional space) injection source located at $r = 0$ m, equation (13) can be written as

$$p(t, 0) = \left(\frac{Q_0^2}{D_0^d t^d} \right)^{1/(dn+2)} \Phi(0), \tag{15}$$

where $\Phi(0)$ is a constant. Using the expression for the pressure distribution $p(t, 0)$, equation (13) can be reformulated, yielding the pressure distribution at distances r smaller than the triggering front r_{tf} [*Shapiro and Dinske, 2009; Shapiro, 2015*]:

$$p(t, r) = p(t, 0) \left(1 - \frac{r^2}{r_{tf}^2} \right)^{1/n}. \tag{16}$$

Please note that $p = 0$ if $r > r_{tf}$.

Assuming that events are only induced for increasing pore fluid pressure, the condition for the back front is given by the vanishing partial time derivative $\frac{\partial p(t,r)}{\partial t}$. Using equation (16) for computing this derivative, we get

$$\frac{\partial p(t,0)}{\partial t} \left(1 - \frac{r^2}{r_{\text{ff}}^2}\right)^{1/n} + \frac{2}{n} p(t,0) \left(1 - \frac{r^2}{r_{\text{ff}}^2}\right)^{(1-n)/n} \frac{r^2}{r_{\text{ff}}^3} \frac{\partial r_{\text{ff}}}{\partial t} = 0. \quad (17)$$

The partial time derivative of the pressure distribution $p(t,0)$ (equation (15)) is given by

$$\frac{\partial p(t,0)}{\partial t} = t^{d/(dn+2)} \frac{1}{t} p(t,0) = \frac{-d}{dn+2} t^{-1} p(t,0). \quad (18)$$

Substituting equation (18) into equation (17) leads to the following criterion for the back front:

$$0 = \frac{-d}{dn+2} t^{-1} + \frac{2}{n} \left(1 - \frac{r^2}{r_{\text{ff}}^2}\right)^{-1} \frac{r^2}{r_{\text{ff}}^3} \frac{\partial r_{\text{ff}}}{\partial t}. \quad (19)$$

The solution $r(t)$ of this equation yields the back front $r_{\text{bf}} = r(t)$.

Using $i = -1$ in equation (14), we get

$$r_{\text{ff}} \propto (Q_0^n D_0 t)^{1/(dn+2)}. \quad (20)$$

The function $\partial r_{\text{ff}}(t)/\partial t$ in equation (19) can be found from equation (20). It is given by

$$\frac{\partial r_{\text{ff}}}{\partial t} \propto \frac{1}{dn+2} (D_0 Q_0^n)^{1/dn+2} t^{-(dn+1)/(dn+2)}. \quad (21)$$

Subsequently, the combination of equations (20) and (21) yields (note that a proportionality constant in these equations is eliminated in this way)

$$\frac{1}{r_{\text{ff}}} \frac{\partial r_{\text{ff}}}{\partial t} = \frac{1}{dn+2} t^{-1}. \quad (22)$$

Substituting this into equation (19) gives the following result:

$$dn = (2 + dn) \frac{r^2}{r_{\text{ff}}^2}, \quad (23)$$

where r is a function of time, describing the back front distance from the source, r_{bf} . Thus,

$$r_{\text{bf}}(t) = r_{\text{ff}}(t) \left(\frac{dn}{2 + dn}\right)^{(1/2)}. \quad (24)$$

Using this relation in combination with equation (20), we finally obtain for the time scaling of the back front of seismicity:

$$r_{\text{bf}} \propto t^{\frac{1}{2+dn}}. \quad (25)$$

Therefore, seismicity induced by the relaxation of pore fluid pressure after the termination of the fluid injection shows a $t^{\frac{1}{2+dn}}$ — proportionality of the back front distance r_{bf} . Since the asymptotic character of equations (18) to (25) is not maintained for $n = 0$, equation (25) is not valid for linear pore fluid pressure diffusion.

Using the above made assumption of a long time limit, we note that the scaling given by equation (25) holds also for the triggering front:

$$r_{\text{ff}} \propto t^{\frac{1}{2+dn}}, \quad (26)$$

which can be applied for linear diffusion cases as well. Unlike equation (20), which is derived from equation (14) and therefore valid for all times, equation (26) applies only to the triggering front for long times after the injection stop.

Equations (24)–(26) have the following implications. In case of strong nonlinearity (high n), the time dependence of both fronts vanishes for long times; i.e., they both stabilize on a time-independent distance.

3. Modeling of Nonlinear Pore Fluid Pressure Diffusion

Since pressure-dependent diffusivities can be observed during proppant injections, such as hydraulic fracturing [Mader, 1989], and self-propping processes by shear dilatation, e.g., at geothermal sites [Durham and Bonner, 1994], the influence of this effect on injection-induced microseismic distributions needs to be further studied not only for coinjection times but also for the postinjection period.

To understand features of coinjection- and postinjection-induced microseismic events under the aforementioned conditions of changing pressure dependencies for the limiting poroelastic case of small Biot constants α (i.e., pure pore fluid pressure diffusion), we perform 3-D finite element numerical modeling (FEM) of the nonlinear equation of diffusion (equation (4)) with initial and boundary conditions given below. Another goal of this study is the validation of the theoretical back front scaling law derived in the previous section.

The FEM is implemented with COMSOL Multiphysics[®], using an iterative **GMRES** (Generalized Minimum Residual) solver with a maximum of 50 iterations. The geometry is meshed with tetrahedral elements for the spatial discretization. The mesh is highly refined in vicinity of the injection source to resolve pressure gradients. To account for the pressure dependence of the hydraulic diffusivity $D(p)$, we apply equation (5) for different indices of nonlinearity n . Regarding the postinjection behavior of the pressure-dependent diffusivity, we apply two models. One model to consider an "elastic" behavior of the diffusivity (i.e., reversible) and another model to account for an irreversible and thus "frozen" diffusivity. These models will be discussed below.

Using the numerically derived pressure distributions in time and space, catalogs of synthetic seismicity are generated, following an approach by Rothert and Shapiro [2003], and spatiotemporal characteristics of synthetic triggering and back fronts are analyzed.

3.1. Numerical Solution

The numerical solution is implemented based on a hydraulic fracturing treatment in the Barnett Shale, Texas, USA (see studies by, e.g., Hummel and Shapiro [2012, 2013]). Here fluids have been injected through a perforated wellbore for 5.4 h with an average flow rate of 0.145 m³/s. The average injection pressure amounted to 8.34 MPa. Both rates did vary only slightly within this interval, and pressures followed flow rate variations. During the treatment, a cumulative amount of fluid of 2683 m³ was injected into the formation.

3.1.1. Frozen Diffusivity Model

To approximate real hydraulic fracturing and geothermal (EGS) case studies, involving propping or self-propping, respectively, assumptions about the postinjection hydraulic behavior of the medium have to be made. As the fluid injection is stopped, the pore fluid pressure p increases up to a distance-dependent maximum $p_{\max}(t, r)$ and decreases thereafter. Consequently, the effective normal stress increases and previously opened fractures and cracks close. However, hydraulic fracturing of low permeable rocks is performed by the hydrocarbon industry to develop permanent flow paths for natural oil and gas. Therefore, proppants are added to the fracturing fluid [Mader, 1989]. These small particles prevent the pore space from closing and maintain the desired flow paths. A similar effect can be achieved in some cases by a self-propping shear dilatation at EGS [Durham and Bonner, 1994]. To account for this postinjection hydraulic behavior of the medium, Hummel and Shapiro [2016] proposed the following frozen diffusivity model.

Terminating the fluid injection at t_0 leads to the relaxation of pore fluid pressure in the form of a diffusional wave with a pressure maximum $p_{\max}(t, r)$ at $r = \sqrt{x^2 + y^2 + z^2}$. As soon as the pressure maximum is reached after the injection stop, the pressure decreases. If the diffusivity D is a function of pressure, it will behave similar to the pressure perturbation. It increases up to a distance-dependent value $D_{\max}(p_{\max}(t, r))$ and would decrease thereafter. However, added proppants preserve the enhanced diffusivity. Therefore, the frozen diffusivity model keeps the diffusivity at each location in the model constant at $D(p(t, r)) = D_{\max}(p_{\max}(t, r))$ as soon as the pressure decreases.

3.1.2. Elastic Diffusivity Model

In addition to the frozen diffusivity model, we test a nonlinear model considering a reversible elastic behavior of the hydraulic diffusivity. In this model, the previously enhanced medium diffusivity $D(p)$ is not held constant but is allowed to decrease as soon as the pore fluid pressure has reached its local maximum $p_{\max}(t, r)$.

Note that a real behavior of the diffusivity will be between these two asymptotic situations, the frozen diffusivity model and the elastic diffusivity model.

3.1.3. Model Geometry, Governing Equations, and Boundary Conditions

For our numerical model, the stimulated rock volume is represented by a sphere with the radius $r_R = 500$ m. This is large enough to exclude any significant numerical interaction between the outer boundary of the model and the pressure perturbation. Following previous works [see, e.g., *Dinske, 2010; Hummel, 2013*], real fluid injection scenarios, where fluids are injected through an open hole or a perforated interval of the wellbore, can be approximated by an effective injection source cavity. Thus, the injection source in our model is realized by a smaller sphere of the radius $r_S = 0.5$ m (as defined by *Hummel [2013]*), located in the center of the large sphere. We do not include actual fractures in our scenario, but the pressure is only allowed to diffuse from the injection source into the spherical model space. Such a geometry effectively approximates the complex 3-D geometry of a hydraulic fracturing treatment which strongly interacts with a 3-D network of preexisting cracks, as observed, for example, in the Barnett Shale [*Hummel and Shapiro, 2013*] (see also Figure 1).

We assume an isotropic pressure-dependent diffusivity $D = D(p(t, r))$ which follows a power law dependence on pressure (equation (5)). For the postinjection interval, the two aforementioned models of diffusivities are applied. To solve for the equation of nonlinear diffusion (equation (4)), we use nonlinearity indices $n = 1, 2, \dots, 5$.

In our modeling procedure, the scaling parameter D_0 is adjusted for each value of n such that the pore fluid pressure $p(x, y, z, t_0)$ at $t = t_0$ does not penetrate beyond a radial distance of $r_{\max, t_0} = 250$ m from the injection point. This maximum penetration distance is taken from the farthest triggered event distance from the source of a typical case study like, e.g., the Barnett Shale seismicity [*Hummel, 2013*].

Initial pressures in the model area are set to $p(x, y, z, t < 0) = 0$ Pa. The fluid injection is realized by a Dirichlet-type boundary condition with $p = p_0$. For this, a boxcar-like injection pressure with a duration of $t_0 = 5.4$ h is defined on the surface of the source cavity. It is switched on at $t = 0$ h and has a magnitude of $p_0 \approx 8.34$ MPa. After the injection stop at $t = t_0$, the pressure at the source is set to 0 Pa. The boundary condition at the outer edge of the model at a large $r = r_R = 500$ m is represented by $\frac{\partial p}{\partial t} = 0$ for the whole modeling time, i.e., by a no-flow boundary.

The time interval of the study is set to $t = [0 \text{ h}, 11.1 \text{ h}]$ with time increments of $\Delta t = 60$ s.

3.2. Synthetic Seismicity

In the following, pressure distributions obtained from both models are used for the generation of catalogs of synthetic seismicity. For this, we apply a method introduced by *Rothert and Shapiro [2003]*. It is based on the hypothesis that rocks contain preexisting fractures and cracks which are critically stressed. Therefore, even small perturbations of pore fluid pressure p above the in situ pore fluid pressure level can modify the effective normal stress such that seismic events are induced. This observation leads to the following triggering criterion:

$$p(x, y, z, t) > C(x, y, z). \quad (27)$$

It results from the classical Mohr-Coulomb failure criterion, i.e., shear failure of optimally oriented faults, and states that a seismic event is triggered, if the pore fluid pressure $p(x, y, z, t)$ exceeds the critical value $C(x, y, z)$ at a certain location (x, y, z) at a given time t . C is a function of in situ stresses and friction along planes of weakness, and values correspond to pressures necessary for shear failure and sliding along preexisting, optimally oriented critically stressed cracks and fractures.

Assuming that a number of randomly generated critical values $C(x, y, z)$ are equally distributed between a minimum value C_{\min} and a maximum of C_{\max} , the criticality field C is defined. For our modeling, the minimum is set to $C_{\min} = 10^5$ Pa. According to *Rothert and Shapiro [2007]*, this is a representative value. The maximum value C_{\max} is given by the injection pressure (i.e., $C_{\max} \approx 9$ MPa), which is the highest pore fluid pressure value that can induce an event, considering the triggering criterion equation (27). A maximum value is required to get an integral of 1 for the probability density function of C . Physically, this value sets a limit to the distribution of critical pressure values.

Possible hypocenter locations are defined by a grid of random, uniformly distributed points (X, Y, Z) within a sphere [*Knuth, 1998*]. In the following, each value of C , being random within $[C_{\min}, C_{\max}]$, is assigned with one location such that $C = C(X, Y, Z)$. Furthermore, numerically obtained pore fluid pressures $p(x, y, z, t)$ are interpolated on the locations (X, Y, Z) such that $p(x, y, z, t) = p(X, Y, Z)$.

The triggering is confined such that once a seismic event is triggered at a certain location (X, Y, Z) , the local criticality is set to a value higher than expected from the pressure distribution. This restriction prevents multiple triggering at one specific location to exclude healing of fractures and cracks due to tectonic loading, which would take much longer compared to the modeling time.

3.3. Fitting Algorithm and Error Estimates

For the fit of equations (6) and (7) to the seismic clouds, event distances $r = \sqrt{x^2 + y^2 + z^2}$ from the source are plotted versus their occurrence times t , yielding r - t plots.

To get an estimate of the triggering front, we look for the farthest triggered events (FEs) at each time step t_i during the injection first. The algorithm works as follows: the first event induced at time step t_i with $i = 1$ is taken as a starting point, i.e., the first FE. The algorithm then checks the event distances at the subsequent time step t_{i+1} . If the event with the largest distance at this time step occurred farther away from the source than the previous FE, this event is registered as the second FE and is taken as the starting point for the next iteration. If no event distance was larger than that of the previous FE, the algorithm proceeds to the next time step t_{i+2} and checks the event distances for this time. As soon as an FE is found, it is taken as a starting point for the next iteration. This procedure is repeated until the injection stop time t_0 is reached and then continued for events after the injection stop.

Regarding the back front of seismicity, the algorithm works similar to the one described above for triggering front events. However, it starts with the back front event (BFE) induced at the last time step t_n and looks regressively for induced events that are closer to the source in previous time steps t_{n-1} until the injection stop at $t = t_0$.

Subsequently, we perform a nonlinear regression to fit power law functions to determine triggering and back fronts (equations (6) and (7)). For this, we use the nonlinear optimization tool "fminsearch" in MATLAB[®]. This tool aims at finding a local minimum of the power law functions, equations (6) and (7), using the so-called Nelder-Mead simplex algorithm as described by *Lagarias et al.* [1998].

We note that synthetic seismic clouds are influenced by numerical errors caused by the chosen mesh size and applied time stepping. To minimize errors caused by the mesh, an adaptive mesh refinement was implemented. Yet inaccuracies in the pressure distribution cannot be excluded. Further, synthetic event locations are subject to the triggering and fitting algorithms. In contrast, recorded seismic event locations are biased by mislocalization, which affects especially events in vicinity of the injection source. Additionally, there is often a lack of event recordings in the postinjection time.

To account for these errors, we apply 95% confidence intervals (CIs) to the curves fitted to the determined FE and BFE. Thus, we assume that the assigned values of A , χ , B , and ψ are statistically significant within the 95% CI, concluding that the obtained values are reasonable estimates accounting for different sources of errors. For this, the MATLAB[®] nonlinear regression function "nlfite" is applied with starting values returned by fminsearch. The output obtained by this is then used together with the functions "nlparci" and "nlpredci" to get confidence and prediction intervals for the fitting parameters A , B , and χ , ψ .

3.4. Discussion of Numerical Results

From the numerical modeling we obtain pore fluid pressure distributions $p(x, y, z, t)$ as well as distributions of the diffusivity $D(x, y, z, t) = (n + 1)D_0\rho^n$. Figure 3 (left column) shows pore fluid pressure profiles taken along the radial distance r from the injection point for different times (color-coded) and for both model realizations. Solid lines indicate results obtained from the frozen diffusivity model, dashed lines represent values derived from the reversible elastic model. The results are shown for indices of nonlinearity $n = 1, 3, 5$ (top to bottom), where $n = 1$ indicates only slight nonlinear diffusion and $n = 5$ represents a case of rather strong nonlinearity.

Noticeable is the distinct pressure decrease in the vicinity of the source, which is analogous to the observation of geometrical spreading in the case of classical propagating waves. The nonlinearity of the pressure diffusion impacts on the shape of the profiles as well as on the pressure magnitude. Increasing nonlinearity leads to more pronounced piston-shaped profiles defined by a distinct pressure drop to zero at the tip of the profile. Furthermore, the stronger the nonlinear fluid-rock interaction, the higher the corresponding pressure values along the profile.

Concentrating on the postinjection phase, the influence of the diffusional-like wave becomes evident. As a result of the termination of the fluid injection at $t = t_0 = 5.4$ h, the pressure defined on the surface of

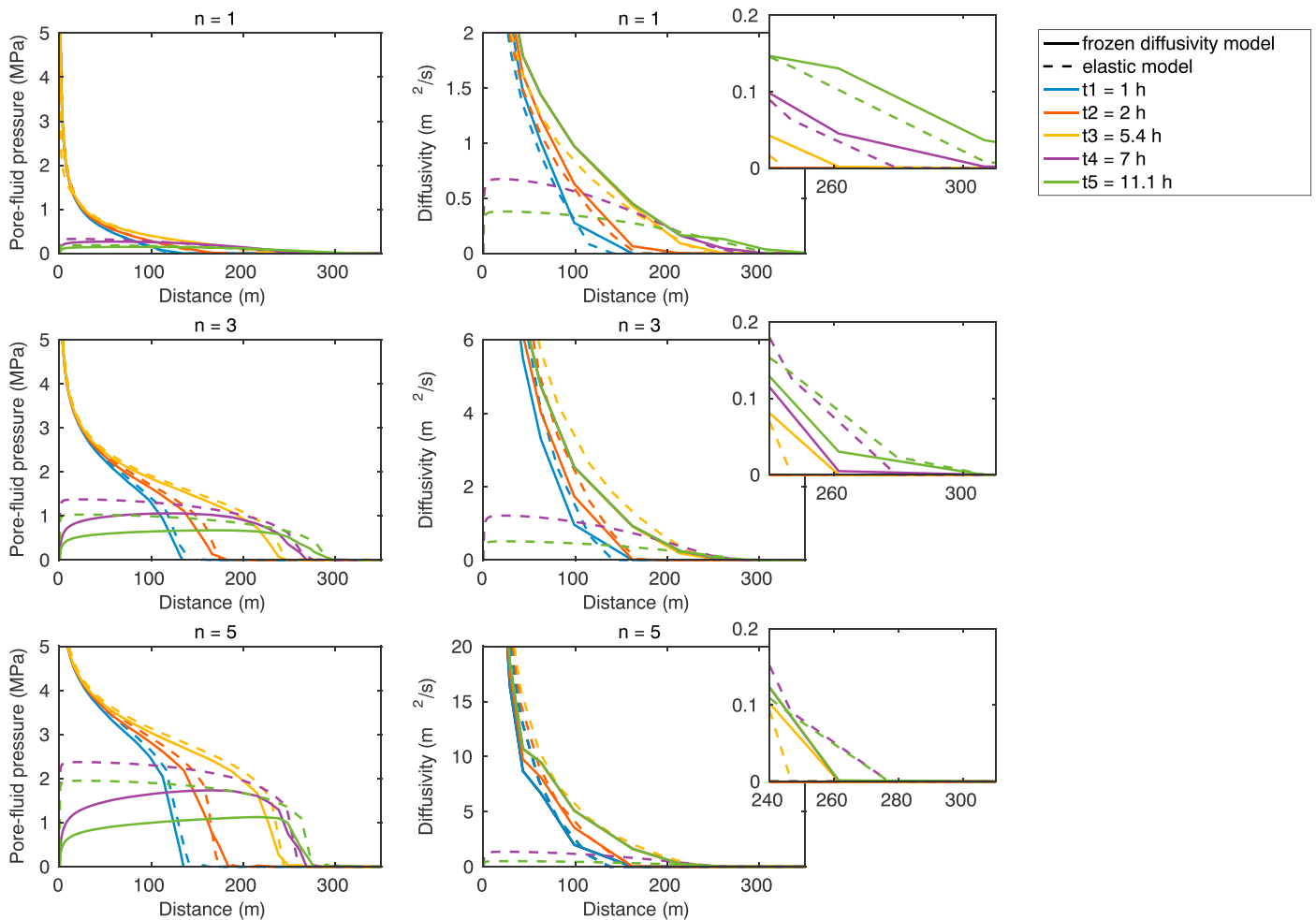


Figure 3. (left column) Numerically derived pore fluid pressure distributions in time and space for different indices of nonlinearity, plotted as pressure profiles for different time steps. A distinct pressure drop characterizes the pressure evolution in vicinity of the borehole as well as the tip of the profiles. The higher the nonlinearity, the more pronounced the piston shape of the profiles. Remarkable differences between both models develop after the injection stop at $t_0 = 5.4$ h. This observation is caused by different realizations of the behavior of the pressure-dependent hydraulic diffusivity $D(p)$. (right column) The evolution of the pressure-dependent diffusivity $D(p)$, obtained from equation (5). Until the injection stop at $t = 5.4$ h (yellow line), the diffusivity for both models varies only slightly. As soon as the pressure drops to 0 Pa, the diffusivity of the “elastic” model follows the pressure evolution, whereas the $D(p)$ in the frozen model remains at its local maximum value.

the source decreases to zero. Nonetheless, the diffusional wave of pore fluid pressure still penetrates farther into the medium. It increases slowly with distance up to a certain pressure maximum $p_{\max}(t > t_0, r)$. This maximum $p_{\max}(t > t_0, r)$ depends on the index of nonlinearity as well as on the distance from the source. The higher the index on nonlinearity and the smaller the distance from the source, the higher the maximum value. Additionally, stronger fluid-rock interaction leads to earlier pressure maxima. However, as soon as the maximum is reached, pressure starts to decrease, marked by a pressure drop at the tip.

Regarding the course of the pressure-dependent diffusivity $D(p)$ given by equation (5), distinct differences between the frozen and elastic diffusivity models can be observed after the injection stop at $t = 5.4$ h. During the injection (at times $t < 5.4$ h), the diffusivity follows the pressure evolution, which is almost the same for both models. However, as soon as the injection pressure is set to 0 Pa at $t = 5.4$ h, the diffusivity in the elastic model drops to zero at the source and increases only slightly further within the medium. In contrast, the diffusivity in the frozen diffusivity model does not decrease after $t = 5.4$ h. Rather, it is held constant at its local value as soon as the pressure starts to decrease at this location. Consequently, the diffusivity in this model

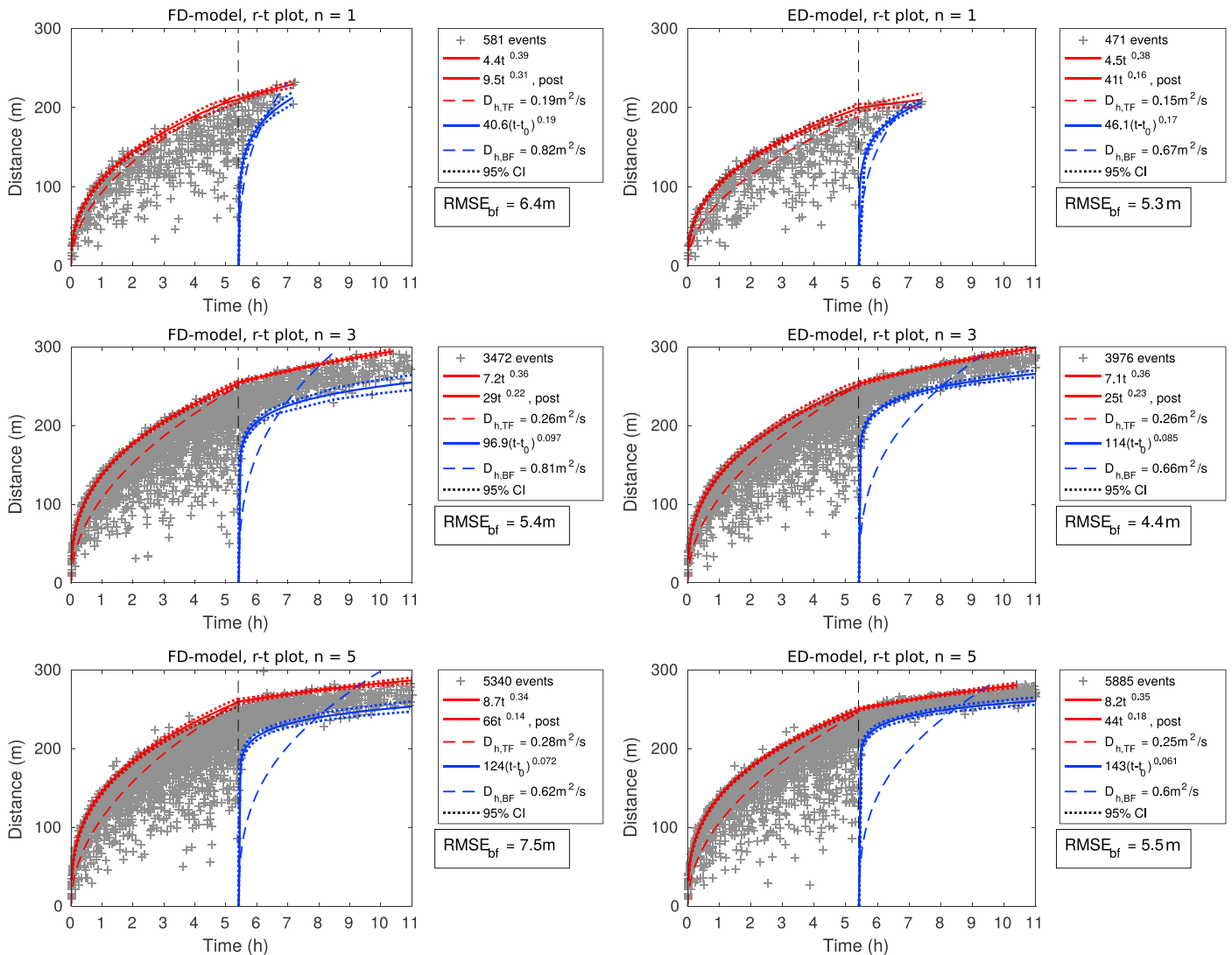


Figure 4. *r-t* plots of synthetic events generated from pressure distributions (left column) of the frozen diffusivity model and (right column) of the reversible elastic realization for different indices of *n*. Regarding spatiotemporal characteristics, the nonlinearity of the diffusion is indicated by a rather cubic root of time-dependent triggering front and an exponent of $\psi < 1/3$ for the back front. Differences between the *r-t* plots of both models, especially after the injection stop (black, dashed line), are related to different pressure distributions. Thin, dotted lines mark the confidence interval of the fit of 95%. The root-mean-square error (RMSE) for the nonlinear regression of the back front of all model realizations <10 m which is smaller than localization errors of real data.

increases after the injection stop only at larger distances. Regardless of the model, the diffusivity increases with higher nonlinearity *n* by more than 1 order of magnitude from more than $6 \text{ m}^2/\text{s}$ at $n = 1$ to over $60 \text{ m}^2/\text{s}$ at $n = 5$.

The spatiotemporal evolution of pore fluid pressure derived from the numerical modeling leads to characteristic seismic clouds. Spatiotemporal event distributions are shown in Figure 4 for $n = 1, 3, 5$ (top to bottom) for the frozen diffusivity model (left column) and for the reversible elastic realization (right column).

Focusing on the injection phase, the evolution of the seismicity for both models coincides. The seismic clouds are characterized by a sharp upper boundary with a concentration of events. This front is also known as the triggering front and describes the distance beyond which the medium has not yet been pressurized. A square root fit according to equation (2) to the farthest triggered events (FEs) in both models, which were found as described above, does not represent spatiotemporal signatures very well (dashed red lines). Fitting equation (6) to the FE, using the algorithm outlined in the previous chapter, confirms that the temporal behavior of the triggering front does not correspond to a \sqrt{t} dependence but shows nearly cubic root signatures

Table 1. Values of the Exponent ψ (Equation (7)) Obtained From Synthetic Data and Real Data Examples From Literature^a

FD Model	Observed ψ	Predicted $1/(dn + 2)$	ED Model	Observed ψ	Predicted $1/(dn + 2)$
$n = 1$	0.17 < 0.19 < 0.21	0.20	$n = 1$	0.15 < 0.17 < 0.19	0.20
$n = 2$	0.11 < 0.13 < 0.14	0.125	$n = 2$	0.11 < 0.12 < 0.13	0.125
$n = 3$	0.085 < 0.097 < 0.11	0.091	$n = 3$	0.079 < 0.086 < 0.092	0.091
$n = 4$	0.081 < 0.089 < 0.098	0.071	$n = 4$	0.062 < 0.068 < 0.073	0.071
$n = 5$	0.063 < 0.072 < 0.082	0.059	$n = 5$	0.053 < 0.061 < 0.068	0.059
Hydraulic fracturing data				observed ψ	estimated n
Horn River Basin (relocated events by A. Reshetnikov)				0.095 < 0.16 < 0.22	2.5 < 4.3 < 8.6
Montney Shale, lower (r - t by Birkelo et al. [2012])				0.14	5.1
EGS data				observed ψ	estimated n
Basel 2006				0.11 < 0.21 < 0.30	0.45 < 0.95 < 2.3
Cooper Basin 2003				0.11 < 0.18 < 0.25	0.69 < 1.2 < 2.5
Fenton Hill (ψ by Hummel and Shapiro [2016])				0.33	0.34
Ogachi (ψ by Hummel and Shapiro [2016])				0.36	0.26

^aFor synthetic data, also predicted values for $1/(dn + 2)$ (equation (25)) are given for the frozen diffusivity model (FD model) and the reversible elastic diffusivity model (ED model). For real data, equation (25) was applied, yielding estimates of the nonlinearity n within 95% confidence intervals. Values of observed ψ and predicted $1/(dn+2)$ are plotted in Figure 5.

(solid red lines). This characteristic is found for both models and indicates nonlinear diffusion of pore fluid pressure. For the elastic diffusivity model (ED model), the fit yields exponents χ between 0.38 and 0.35 for $n = 1$ and $n = 5$, respectively. In comparison, for the frozen diffusivity model (FD model), values of χ between 0.39 and 0.34 for $n = 1$ and $n = 5$, respectively, are obtained. The 95% CI is marked by thin, dotted red lines.

In terms of postinjection-induced seismicity, the triggering front seems to change its temporal evolution. Events occur at smaller distances than predicted by the triggering front from equation (6). Values of χ derived from the fit of equation (6) to farthest triggered events after the injection stop get smaller for the postinjection triggering front (solid red lines, indicated in the respective legend by “post”). This observation corresponds to the derived scaling law for the triggering front at times $t > t_0$ (equation (26)). Furthermore, seismic event clouds for both models reveal a domain of seismic quiescence which evolves with time $t > t_0$ from the injection source. A linear diffusion back front according to equation (3) does not adequately describe the temporal behavior of postinjection-induced seismicity (dashed blue lines). Therefore, equation (7) is applied to synthetic seismicity for both models (solid blue lines), using the fitting algorithm (explained above). Values of ψ are summarized in Table 1. For the FD-model, this yields exponents between 0.19 and 0.072 for $n = 1$ and $n = 5$, respectively. In comparison, values decrease from 0.17 to 0.061 between $n = 1$ and $n = 5$ for the reversible elastic model. For both models $\psi < 1/3$, which again is typical for seismicity induced by nonlinear diffusion. The 95% CI of the back front fit is marked by thin blue lines. For all model realizations, the front lies well within this interval. Root-mean-square errors (RMSE) of the estimated front obtained from the nonlinear regression are given in each subfigure. Values are <10 m. This is smaller than typical localization inaccuracies of data, which are usually in the range of tens of meters. Thus, the determined back fronts can be assumed to be a good approximation of the spatiotemporal evolution of microseismic events.

4. Validation of the Scaling and Application to Real Data

The novel scaling law for the back front of seismicity (equation (25)) demonstrates that the temporal behavior of the back front of seismicity is consistent with the idea that the back front of seismicity is controlled by the nonlinearity of pore fluid pressure diffusion and the Euclidean dimension of the dominant growth of the seismic cloud. To validate this finding, we compare the theoretical exponent $1/(dn + 2)$ to the exponent ψ , which was obtained from a power law fit to synthetic seismicity (equation (7)). Subsequently, we apply the scaling to real data examples. Observed values of ψ , predicted values of $\psi = 1/(dn + 2)$ for the synthetic data, and estimates of n for real data are also summarized in Table 1.

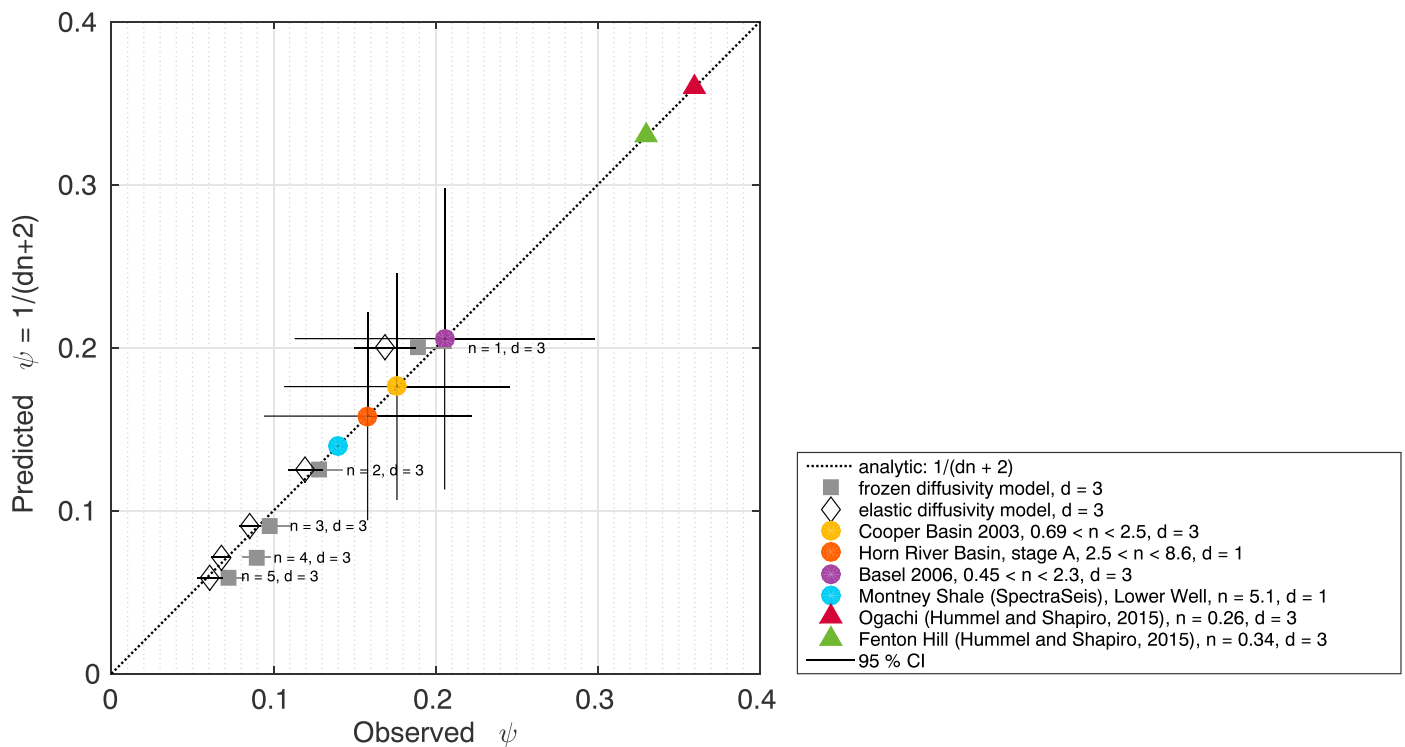


Figure 5. Theoretical relation for the back front scaling compared to exponents ψ derived for the frozen diffusivity and elastic model as well as to observed real data examples. The values of ψ derived for the synthetic seismicity as well as for real data examples coincide with theoretically predicted values from equation (25). Thin solid lines show the 95% confidence interval of the fitted parameter ψ .

In Figure 5, predicted values of the theoretical exponent $1/(dn + 2)$ are plotted versus observed values of ψ , including error bars. Focusing on the synthetic seismicity, the derived exponents are well approximated by the theoretical line. This is especially the case for synthetic seismicity for the reversible elastic model. Slight discrepancies between the theoretical value and ψ derived for the frozen diffusivity model are attributable to the fact that equation (25) does not describe a frozen diffusivity. Despite this, it can be concluded that the derived scaling law can explain the controlling parameters of the back front which evolves after the termination of a fluid injection. Thus, the relation can be used for parameter estimates if one of the parameters is unknown.

For a demonstration of this advantage, we apply the $\psi = 1/(dn + 2)$ dependence to real data examples. Note that fluid-induced seismicity frequently occurs in hydraulically anisotropic media. To account for this anisotropy, we use an effective isotropic medium transformation introduced by Hummel [2013] for seismic clouds induced at the Basel and Cooper Basin EGS sites before a fit of both fronts.

Case studies from hydraulic fracturing operations performed by the hydrocarbon industry in Canada, Horn River Basin and Montney Shale [see, respectively, Baig et al., 2015; Birkelo et al., 2012], are two examples where the Euclidean dimension of the seismic cloud can be estimated from the dominant growth tendency of the microseismic cloud, yielding $d = 1$. Such a one-dimensional case, depicted in Figure 1a, indicates that seismic events occur on or at least close to the created classical hydraulic fracture such that their locations can be projected onto the fracture. Since the equation of diffusion (equation (4)) we solved numerically (section 3.1) is also valid for 1-D scenarios, the theoretical scaling law can be applied here. Now we have a chance to estimate the strength of nonlinear pore fluid pressure diffusion. Fitting function (7) to the back front in corresponding $r-t$ plots (solid blue lines in Figures 6 and 7) yields exponents ψ . For the Horn River Basin it is $\psi_{HRB} = 0.16$ (solid blue line) within a CI of $\psi = [0.095, 0.22]$ (dotted blue lines). This rather large interval for ψ results from a lack of events after the injection stop, which makes a definition of the back front difficult. Regarding the Montney Shale case, a fit to the lower well induced seismicity results in $\psi_{Mo} = 0.14$. The application of CI was not possible in this case, since the fit was implemented only for the $r-t$ plot by Birkelo et al. [2012] without exact

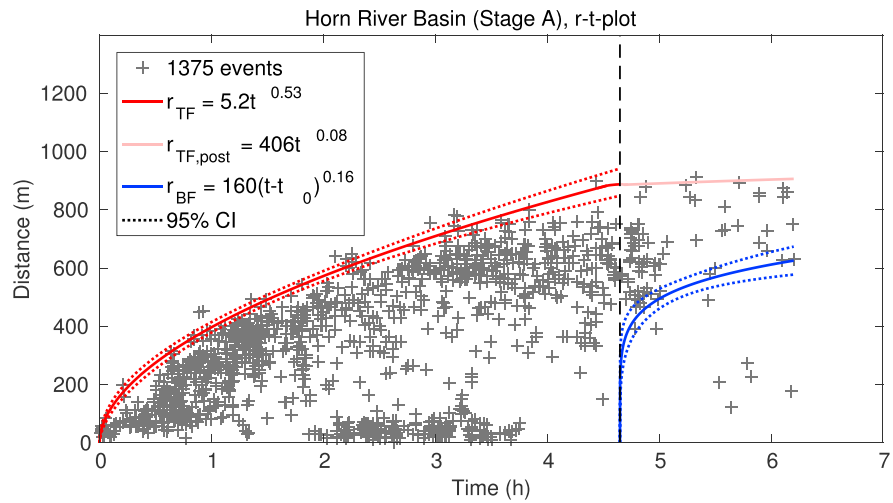


Figure 6. *r-t* plot of Horn River Basin seismicity. Seismicity induced by the fluid injection can be related to nonlinear diffusion, indicated by a temporal dependence with $\chi < 1/2$ for the triggering front and with $\psi = 0.16$ for the back front. After the injection stop (black, dashed line), the triggering front clearly changes its behavior as predicted by equation (26). Note that $\chi \approx 1/2$ of the triggering front for the case of a nearly 1-D hydraulic fracture is an indication of strong leak-off into the surrounding reservoir [see Shapiro, 2015, chap. 4]. Dotted lines indicate the 95% confidence interval. Data have been provided by a sponsor of the PHASE consortium. We thank A. Reshetnikov for relocating the events.

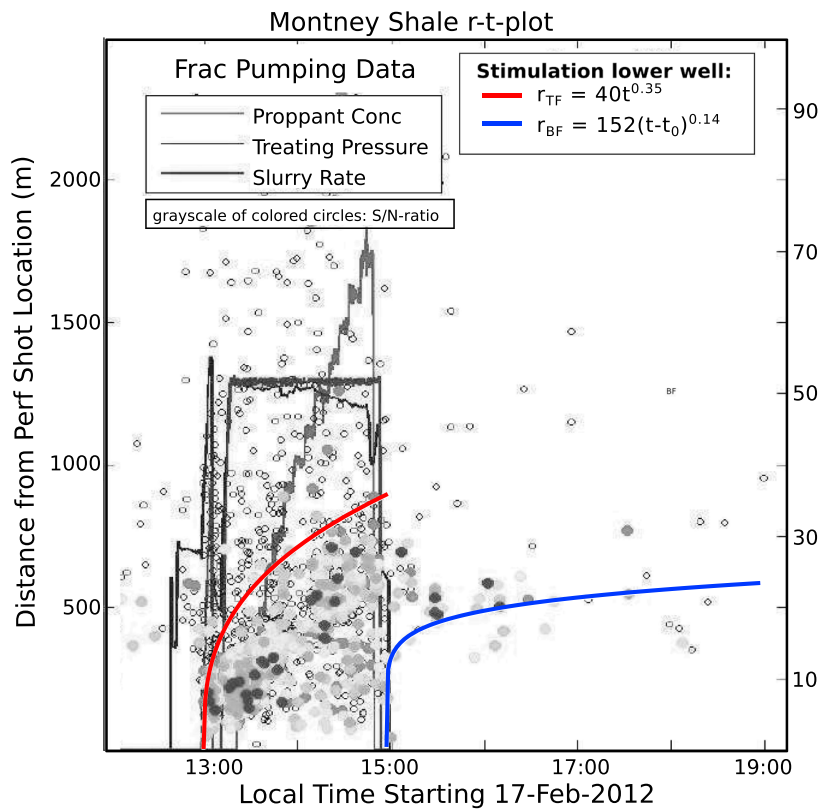


Figure 7. Stimulation of two different wells in the Montney Shale led to fluid-induced seismicity. The spatiotemporal event distribution indicates that seismicity in the Lower Montney Shale was induced by nonlinear pore fluid pressure diffusion. The injection was stopped at approximately 15:00. *r-t* plot by Birkelo et al. [2012].

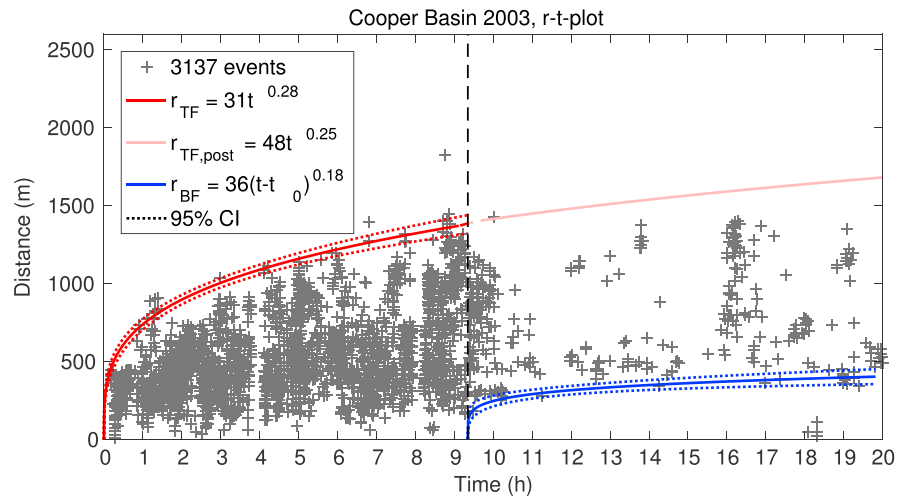


Figure 8. Cooper Basin r - t plot of events in an effective isotropic medium. Power law fits to the triggering front and the back front of seismicity with equations (6) and (7) reveal that seismicity was induced by nonlinear diffusion of pore fluid pressure. As soon as the injection pressure at the source ceases (indicated by the black, dashed line), the slope of the triggering front changes which is in accordance to the scaling law for the triggering front after the injection stop (equation (26)). Dotted lines mark the confidence interval of 95% of the fit. The data are courtesy of H. Kaieda. [see also Shapiro and Dinske, 2009].

event locations. Thus, the errors can be assumed to be rather large. To determine the strength of influence of nonlinear pore fluid pressure diffusion for both case studies, observed values of ψ are plotted in Figure 5. For the Horn River Basin stimulation, also error bars resulting from the 95% confidence interval are shown. Given that the diffusion of pore fluid pressure in both cases occurred along a 1-D hydraulic fracture (i.e., $d = 1$) and using the obtained value of ψ , a best fit to the theoretical law for the Horn River Basin is achieved for $n = 4.3$, which lies within the 95% confidence interval of $n = [2.5, 8.6]$. For the Montney Shale, n is determined to be $n = 5.1$ for the lower well hydraulic fracturing treatment.

Two case studies from EGS operations in Basel, Switzerland, and Cooper Basin, Australia, further confirm the applicability and advantage of the scaling law [see Häring et al., 2008; Asanuma et al., 2005]. Again, function (7)

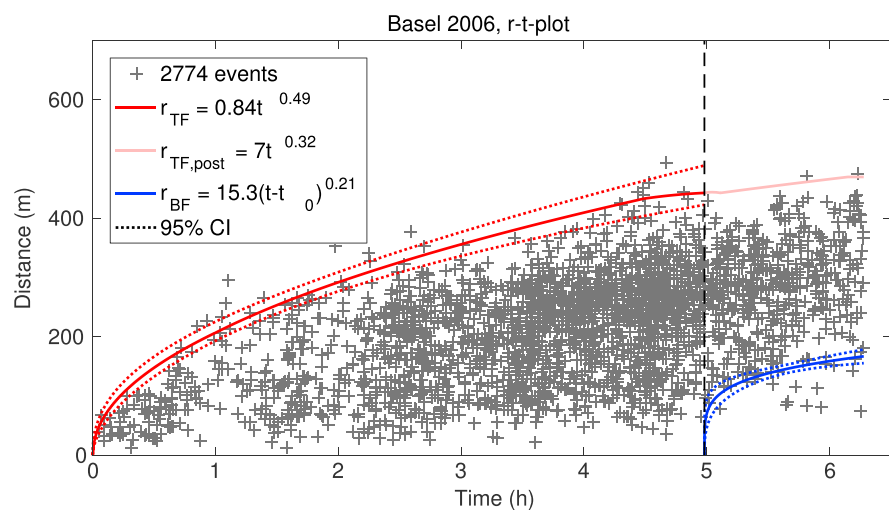


Figure 9. r - t plot of seismicity in an effective isotropic medium at the EGS site Basel. Seismicity induced by the fluid treatment is assumed to be related to a slightly nonlinear diffusion of pore fluid pressure as indicated by $\psi < 0.3$ for the back front. The triggering front clearly changes its temporal behavior after the injection stop (black, dashed line). Dotted lines indicate the 95% confidence interval of the fit. The data are courtesy of U. Schanz and M. O. Häring [see also Shapiro and Dinske, 2009].

can be fitted to seismic back fronts in corresponding r - t plots with a confidence interval of 95% (see Figures 8 and 9, solid and dotted blue lines, respectively). This gives exponents ψ for both reservoirs with $\psi_{Ba} = 0.21$ in an interval of $\psi = [0.11, 0.30]$ and $\psi_{CB} = 0.18$ between $\psi = [0.11, 0.25]$. In both cases, hydraulic fracturing operations induced 3-D seismic clouds. Therefore, plotting observed values of ψ in Figure 5 and assuming $d = 3$, the influence of nonlinear fluid-rock interaction can be estimated. Obviously, seismicity in the Basel EGS operation was controlled by only weak nonlinear diffusion of pore fluid pressure, $n = 0.95$ within boundaries of $0.45 < n < 2.3$. In the Cooper Basin, nonlinear pore fluid pressure diffusion was slightly higher, yielding $n = 1.2$ with lower and upper boundaries of $0.69 < n < 2.5$. The difference between the two scenarios may be related to different in situ stress regimes: Whereas the stress field at the Basel EGS site can be characterized by a strike-slip regime [Kraft and Deichmann, 2014], maximum principal stresses are horizontal at Cooper Basin, indicating a thrust fault regime [Baisch and Vörös, 2010].

Comparing the case studies for EGS operations and hydraulic fracturing of hydrocarbon reservoirs, a distinct difference of n can be seen. The influence of nonlinear diffusion at the examined hydraulic fracturing sites Montney Shale and Horn River Basin is much larger than that observed during EGS operations in Basel and Cooper Basin. Such an observation correlates well with the actual aim of hydraulic fracturing of hydrocarbon reservoirs and the hydraulic stimulation of geothermal sites: Injection pressures usually do not exceed the local minimum stress at EGS (see, e.g., for Basel) [Häring *et al.*, 2008], which prevents the opening of new fractures. In contrast, the production of unconventional hydrocarbons from tight formations requires massive fracturing of the rock by injection pressures higher than the minimum in situ principal stress. Such a process may artificially increase the in situ hydraulic diffusivity and permeability by several orders of magnitude [see Shapiro, 2015, p. 200], resulting in nonlinear diffusion as discussed above.

5. Discussion of Assumptions and Competing Models

Recently, several models have been developed to describe spatiotemporal characteristics of fluid-induced seismicity during as well as after the injection.

Among these models, poroelastic coupling models were developed to describe injection- and production-induced seismicity. (as discussed by, e.g., Rutqvist *et al.* [2008], Rozhko [2010], Segall and Lu [2015], and Chang and Segall [2016]). These works are all based on Biot's idea [Biot, 1941] that pressure changes, such as caused by fluid injections, induce a stress field. In turn, these stresses might affect pore fluid pressures. For more information, see also section 1.

Yet for the case of injections into low permeable rocks, the observed spatiotemporal distribution of microseismic events induced by proppant injections or self-propping processes is adequately described by incorporating only pore fluid pressure diffusion, while ignoring poroelastic fluid-to-solid coupling [see, e.g., Talwani and Acree, 1984; Shapiro *et al.*, 1997, 1999, 2002]. Also, we note that a diffusion model is the end-member case of poroelastic coupling in which the poroelastic coupling parameter $\alpha \rightarrow 0$. Therefore, such a scenario is an important and necessary step for further understanding of seismicity-controlling mechanisms.

For the purpose of the derivation of the novel scaling relation as described above, we accepted nonlinear diffusion of pore fluid pressure, in which the hydraulic diffusivity becomes a function of pressure as the driving force behind observed seismic events. This process was studied in detail by Shapiro and Dinske [2009] and further described, e.g., by Hummel and Shapiro [2013] and Shapiro [2015]. Other nonlinear diffusion models were, for example, developed and adapted by Rice [1992], Miller *et al.* [2004], Gischig and Wiemer [2013], and Miller [2015].

Certainly, a model of nonlinear pore fluid pressure diffusion is just one mechanism to describe real observations of injection-induced seismicity. Other models, which additionally include stress changes related to the seismicity rate, as proposed by Dieterich [1994] and applied by Segall and Lu [2015], might also be a contributing explanation for injection-induced seismic events.

We do not want to exclude other possible seismicity-controlling mechanisms. However, the application and combination of many different factors is beyond the scope of the work presented in this paper, which aimed at the derivation of a novel scaling relation to explain observed features of postinjection-induced seismicity. Our approach showed that a rather straightforward model can explain observed microseismic features; that is, microseismicity after the injection stop is mainly controlled by the nonlinearity of the diffusion process as

well as the dimension of the dominant growth direction of the seismic cloud. Nonetheless, it is already under consideration to include poroelastic pressure-stress coupling to future nonlinear diffusion models.

We studied a simplified case of equally distributed possible hypocenter locations with a uniform distribution of critical pressure values. It is likely that large faults exist in the medium which might act as possible fast pathways for the pressure or for stress transmission to deeper levels [Chang and Segall, 2016]. Furthermore, in situ stresses might have a significant impact on the evolution of seismic hypocenter locations. Therefore, for explicit case studies in future, knowledge of preexisting fractures as well as the in situ stress regime should be included in the model.

Regarding possible leak-off effects caused by fluids which enter the formation from the hydraulic fracture, we can qualitatively state the following: Our model implies that the leak-off is significant for small n ($n \leq 1$) but vanishes if n is significantly higher than 1. With respect to flowback volumes, for negligible leak-off ($n > 1$) and the elastic model, flowback will be approximately equal to the injected volume. In the frozen model, flowback will be significantly smaller. In the case of a high leak-off ($n < 1$), the flowback to the borehole will vanish. Note that a high n just means a volume balance: The volume of the opened pore space is approximately equal to the injected fluid amount.

Assuming that fluid-induced seismicity is controlled by a rather general case of pore fluid pressure diffusion, we fitted power law functions to the triggering and back front of seismic clouds. This yields estimates of the temporal dependence, given by exponents ψ . In order to account for numerical errors as well as inaccuracies caused by triggering and fitting algorithms for synthetic data and localization uncertainties as well as rare postinjection-induced events of real data, we introduced 95% confidence intervals of the triggering and back front fits, which are an accepted measure for inaccuracies in statistics. Corresponding r - t plots illustrate that these intervals are a good approximation. Regarding the application of the scaling law (equation (25)) to real observed data, the significance of 95% results in a range of values for the index of nonlinearity n . This uncertainty has to be considered when the values are used for further reservoir simulations and hazard assessments.

6. Conclusion

For the numerical 3-D solution of nonlinear pore fluid pressure diffusion, we assumed a power law dependence of the hydraulic diffusivity on pressure [Shapiro and Dinske, 2009]. We applied two different models regarding postinjection behavior of the hydraulic diffusivity, a frozen diffusivity model as introduced by Hummel and Shapiro [2016] and a reversible elastic model. Even if the latter one is easier to implement, the frozen diffusivity model captures the usage of proppants added to the fracturing fluid to keep the hydraulic diffusivity constant after the injection stop. Nevertheless, real configurations are somewhere between these two end-member approximations, explaining the implementation of both models, the frozen diffusivity model and the reversible elastic model.

We proposed a novel scaling law for the back front of induced seismicity. It reveals that postinjection-induced seismicity is sensitive to the nonlinearity (quantified by the index n) of the diffusion process and to the Euclidean dimension d of the preferential direction of growth of the seismic cloud. Therefore, the derived dependence becomes of particular importance when one of the two parameters is unknown. This may be fundamental for the development and the optimization of hydrocarbon reservoirs, for example, for modeling of production. The validity of the theoretical dependence was verified by synthetic data and was subsequently successfully applied to data from case studies.

Seismic monitoring systems and long-enough record times after the termination of the fluid injection are crucial for successful and reliable assessments of the controlling hydraulic parameters and thus for the optimization of production of hydrocarbons from unconventional reservoirs (or operation of EGS sites) and seismic hazard assessment.

References

- Al-Wardy, W., and R. W. Zimmerman (2004), Effective stress law for the permeability of clay-rich sandstones, *J. Geophys. Res.*, *109*, B04203, doi:10.1029/2003JB002836.
- Asanuma, H., N. Soma, H. Kaieda, Y. Kumano, T. Izumi, K. Tezuka, H. Niitsuma, and D. Wyborn (2005), Microseismic monitoring of hydraulic stimulation at the Australian HDR project in Cooper Basin, paper presented at World Geothermal Congress 2005, Antalya, Turkey, 24–29 Apr.

Acknowledgments

We thank the sponsors of the PHASE consortium project for supporting the research presented in this manuscript. Microseismic data used for this work have been provided by sponsors of the PHASE consortium project and cannot be made publicly available. However, the data are properly cited and referred to in Table 1 and in the reference list. Corresponding r - t plots are visualized in the manuscript. Numerical data, MATLAB codes, and synthetic seismicity can be obtained upon request from the authors (lisajohann@zedat.fu-berlin.de). The data are visualized in the corresponding figures and are also listed in Table 1. We thank the Associate Editor Doug Schmitt, the reviewer Adam Baig, and one anonymous reviewer for their helpful and constructive comments which substantially improved the quality of the manuscript.

- Baig, A., G. Viegas, T. Urbancic, E. v. Lunen, and J. Hendrick (2015), To frac or not to frac: Assessing potential damage as related to hydraulic fracture induced seismicity, *First Break*, 33(7), 67–71.
- Baisch, S., and R. Vörös (2010), Reservoir induced seismicity: Where, when, why, how strong?, paper presented at World Geothermal Congress, 2010, Bali, Indonesia, 25–29 Apr.
- Barenblatt, G. I. (1996), *Scaling, Self-Similarity and Intermediate Asymptotics*, Cambridge Univ. Press, New York.
- Berryman, J. G. (1992), Effective stress for transport properties of inhomogeneous porous rock, *J. Geophys. Res.*, 97, 17,409–17,424, doi:10.1029/92JB01593.
- Biot, M. (1941), General theory of three-dimensional consolidation, *J. Appl. Phys.*, 12, 155–164.
- Birkelo, B., K. Cieslik, B. Witten, S. Montgomery, B. Artman, D. Miller, and M. Norton (2012), High-quality surface microseismic data illuminates fracture treatments: A case study in the Montney, *Leading Edge*, 31, 1318–1325.
- Carslaw, H., and J. Jaeger (1959), Conduction of heat in solids.
- Chang, K. W., and P. Segall (2016), Injection-induced seismicity on basement faults including poroelastic stressing, *J. Geophys. Res. Solid Earth*, 121, 2708–2726, doi:10.1002/2015JB012561.
- Detournay, E., and H.-D. C. Alexander (1993), Fundamentals of poroelasticity, in *Comprehensive Rock Engineering: Principles, Practice and Projects*, vol. 2, edited by C. Fairhurst, pp. 113–171, Pergamon Press, New York.
- Dieterich, J. (1994), A constitutive law for rate of earthquake production and its application to earthquake clustering, *J. Geophys. Res.*, 99(B2), 2601–2618.
- Dinske, C. (2010), Interpretation of fluid-induced seismicity at geothermal and hydrocarbon reservoirs of Basel and Cotton Valley, PhD thesis, Freie Univ., Berlin.
- Durham, W. B., and B. P. Bonner (1994), Self-propping and fluid flow in slightly offset joints at high effective pressures, *J. Geophys. Res.*, 99(B5), 9391–9399, doi:10.1029/94JB00242.
- Elsworth, W. (2013), Injection-induced earthquakes, *Science*, 341, 1225942, doi:10.1126/science.1225942.
- Gischig, V. S., and S. Wiemer (2013), A stochastic model for induced seismicity based on non-linear pressure diffusion and irreversible permeability enhancement, *Geophys. J. Int.*, 194(2), 1229–1249, doi:10.1093/gji/ggt164.
- Grasso, J.-R. (1992), Mechanics of seismic instabilities induced by the recovery of hydrocarbons, *Pure Appl. Geophys.*, 139(3), 507–534, doi:10.1007/BF00879949.
- Griggs, D. T. (1936), Deformation of rocks under high confining pressures: I. Experiments at room temperature, *J. Geol.*, 44(5), 541–577.
- Håring, M. O., U. Schanz, F. Ladner, and B. C. Dyer (2008), Characterisation of the Basel 1 enhanced geothermal system, *Geothermics*, 37, 469–495.
- Healy, J. H., W. W. Rubey, D. T. Griggs, and C. B. Raleigh (1968), The Denver earthquakes, *Science*, 161(3848), 1301–1310.
- Hsieh, P. A., and J. D. Bredehoeft (1995), A reservoir analysis of the Denver earthquakes: A case of induced seismicity, *Energy Convers. Manage.*, 36(6–9), 535–538.
- Hummel, N. (2013), Pressure-dependent hydraulic transport as a model for fluid induced earthquakes, PhD thesis, FU Berlin.
- Hummel, N., and S. Shapiro (2016), Back front of seismicity induced by non-linear pore pressure diffusion, *Geophys. Prospect.*, 64(1), 170–191, doi:10.1111/1365-2478.12247.
- Hummel, N., and S. A. Shapiro (2012), Microseismic estimates of hydraulic diffusivity in case of non-linear fluid-rock interaction, *Geophys. J. Int.*, 188(3), 1441–1453.
- Hummel, N., and S. A. Shapiro (2013), Nonlinear diffusion-based interpretation of induced microseismicity: A Barnett Shale hydraulic fracturing case study, *Geophysics*, 78, B211–B226, doi:10.1190/geo2012-0242.1.
- Jaeger, J. C., N. G. W. Cook, and R. W. Zimmerman (2007), *Fundamentals of Rock Mechanics*, 4th ed., 475 pp., Wiley-Blackwell, Malden, Mass.
- Katsube, T. J., B. S. Mudford, and M. E. Best (1991), Petrophysical characteristics of shales from the Scotian shelf, *Geophysics*, 56(10), 1681–1689, doi:10.1190/1.1442980.
- King, V., L. Block, and C. Wood (2016), Pressure/flow modeling and induced seismicity resulting from two decades of high-pressure deep-well brine injection, Paradox Valley, Colorado, *Geophysics*, 81(5), B119–B134, doi:10.1190/GEO2015-0414.1.
- Knuth, D. E. (1998), *The Art of Computer Programming*, Addison-Wesley Longman, Reading, Mass.
- Kraft, T., and N. Deichmann (2014), High-precision relocation and focal mechanism of the injection-induced seismicity at the Basel EGS, *Geothermics*, 52, 59–73.
- Lagarias, J. C., J. A. Reeds, M. H. Wright, and P. E. Wright (1998), Convergence properties of the Nelder-Mead simplex method in low dimensions, *SIAM J. Optim.*, 9(1), 112–147.
- Langenbruch, C., and S. Shapiro (2014), Gutenberg-Richter relation originates from Coulomb stress fluctuations caused by elastic rock heterogeneity, *J. Geophys. Res. Solid Earth*, 119, 1220–1234, doi:10.1002/2013JB010282.
- Li, M., Y. Bernabé, W.-I. Xiao, Z.-Y. Chen, and Z.-Q. Liu (2009), Effective pressure law for permeability of E-bei sandstones, *J. Geophys. Res.*, 114, B07205, doi:10.1029/2009JB006373.
- Mader, D. (1989), *Hydraulic Proppant Fracturing and Gravel Picking*, vol. 26, pp. 173–174, Elsevier Sci., Amsterdam, Netherlands.
- Majer, E. L., R. Baria, M. Stark, S. Oates, J. Bommer, B. Smith, and H. Asanuma (2007), Induced seismicity associated with Enhanced Geothermal Systems, *Geothermics*, 36(3), 185–222, doi:10.1016/j.geothermics.2007.03.003.
- Miller, S. A. (2015), Modeling enhanced geothermal systems and the essential nature of large-scale changes in permeability at the onset of slip, *Geofluids*, 15(1–2), 338–349, doi:10.1111/gfl.12108.
- Miller, S. A., C. Collettini, L. Chiaraluca, M. Cocco, M. Barchi, and B. J. P. Kaus (2004), Aftershocks driven by a high-pressure CO₂ source at depth, *Nature*, 427, 724–727, doi:10.1038/nature02251.
- Parotidis, M., S. A. Shapiro, and E. Rotherth (2004), Back front of seismicity induced after termination of borehole fluid injection, *Geophys. Res. Lett.*, 31, L02612, doi:10.1029/2003GL018987.
- Paterson, M. S., and T.-F. Wong (2005), *Experimental Rock Deformation—The Brittle Field*, Springer, Berlin.
- Raleigh, C. B., J. H. Halej, and J. D. Bredehoeft (1972), Faulting and crustal stress at Rangely, Colorado, in *Flow and Fracture of Rocks*, *Geophys. Monogr. Ser.*, vol. 16, pp. 275–284, AGU, Washington, D. C., doi:10.1029/GM016p0275.
- Raleigh, C. B., J. H. Halej, and J. D. Bredehoeft (1976), An experiment in earthquake control at rangely, Colorado, *Science*, 191, 1230–1237.
- Rice, J. R. (1992), Fault stress states, pore pressure distribution, and the weakness of the San Andreas Fault, in *Fault Mechanics and Transport Properties of Rock*, edited by B. Evans and T. F. Wong, pp. 476–503, Academic Press, San Diego, Calif.
- Rotherth, E., and S. A. Shapiro (2003), Microseismic monitoring of borehole fluid injections: Data modeling and inversion for hydraulic properties of rocks, *Geophysics*, 68, 685–689.
- Rotherth, E., and S. A. Shapiro (2007), Statistics of fracture strength and fluid-induced microseismicity, *J. Geophys. Res.*, 112, B04309, doi:10.1029/2005JB003959.
- Rozhko, A. Y. (2010), Role of seepage forces on seismicity triggering, *J. Geophys. Res.*, 115, B11314, doi:10.1029/2009JB007182.

- Rutqvist, J., J. Birkholzer, and C.-F. Tsang (2008), Coupled reservoir-geomechanical analysis of the potential for tensile and shear failure associated with CO₂ injection in multilayered reservoir-caprock systems, *Int. J. Rock Mech. Min. Sci.*, *45*, 132–143.
- Segall, P. (1989), Earthquakes triggered by fluid extraction, *Geology*, *17*, 942–946.
- Segall, P., and S. Lu (2015), Injection-induced seismicity: Poroelastic and earthquake nucleation effects, *J. Geophys. Res. Solid Earth*, *120*, 5082–5103, doi:10.1002/2015JB012060.
- Shapiro, S. (2015), *Fluid-Induced Seismicity*, Cambridge Univ. Press, Cambridge, U. K.
- Shapiro, S. A. (2012), Comment on “Role of seepage forces on seismicity triggering”, *J. Geophys. Res.*, *117*, B03305, doi:10.1029/2011JB008346.
- Shapiro, S. A., and C. Dinske (2009), Scaling of seismicity induced by nonlinear fluid-rock interaction, *J. Geophys. Res.*, *114*, B09307, doi:10.1029/2008JB006145.
- Shapiro, S. A., E. Huenges, and G. Borm (1997), Estimating the permeability from fluid-injection induced seismic emission at the KTB site, *Geophys. J. Int.*, *131*, F15–F18.
- Shapiro, S. A., P. Audigane, and J.-J. Royer (1999), Large-scale in situ permeability tensor of rocks from induced microseismicity, *Geophys. J. Int.*, *137*, 207–213.
- Shapiro, S. A., E. Rothert, V. Rath, and J. Rindschwentner (2002), Characterization of fluid transport properties of reservoirs using induced microseismicity, *Geophysics*, *67*, 212–220.
- Shapiro, S. A., R. Niemann, G. P. Khizhniak, Y. P. Ilyushin, V. V. Plotnikov, and S. V. Galkin (2015), Stress-dependent permeability versus stiff and compliant porosity: Theory and experiments, SEG Technical Program Expanded Abstracts SEG–2015-5761906, presented at 2015 SEG Annual Meeting, pp. 2990–2994, Society of Exploration Geophysicists, New Orleans, Louisiana, 18–23 Oct., doi:10.1190/segam2015-5761906.1.
- Suckale, J. (2009), Induced seismicity in hydrocarbon fields, in *Advances in Geophysics*, vol. 51, edited by R. Dmowska, pp. 55–106, Academic Press, USA.
- Talwani, P., and S. Acree (1984), Pore pressure diffusion and the mechanism of reservoir-induced seismicity, *Pure Appl. Geophys.*, *122*(6), 947–965, doi:10.1007/BF00876395.
- Terzaghi, K. (1936), The shearing resistance of saturated soils and the angle between planes of shear, paper presented at 1st International Conference on Soil Mechanics and Foundation Engineering, vol. 1, pp. 54–56, Harvard Univ. Press, Cambridge, Mass.
- Van Wees, J. D., L. Buijze, K. Van Thienen-Visser, M. Nepveu, B. B. T. Wassing, B. Orlic, and P. A. Fokker (2014), Geomechanics response and induced seismicity during gas field depletion in the Netherlands, *Geothermics*, *52*, 206–219, doi:10.1016/j.geothermics.2014.05.004.
- Zoback, M., and H. P. Harjes (1997), Injection-induced earthquakes and crustal stress at 9 km depth at the KTB deep drilling site, Germany, *J. Geophys. Res.*, *102*, 18,477–18,491.
- Zoback, M. D., and J. C. Zinke (2002), Production-induced normal faulting in the Valhalland Ekofisk oil fields, *Pure Appl. Geophys.*, *159*, 403–420.

CHAPTER 4

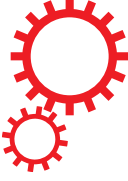
The Surge of Earthquakes in Central Oklahoma Has Features of Reservoir-Induced Seismicity¹

Key Points:

- Earthquakes linked to large-volume wastewater disposal in Central Oklahoma, U.S., occur below the injection formation in the crystalline basement.
- A novel conceptual model was developed based on the physics of reservoir-induced seismicity, taking poroelastic stress changes into account.
- Analytic solutions and numerical modelling results capture spatio-temporal features of the observed seismicity, also if disposal volumes are declining.


¹ This article has been published in Nature Scientific Reports: L. Johann, S. A. Shapiro and C. Dinske (2018). The surge of earthquakes in Central Oklahoma has features of reservoir-induced seismicity. DOI: <https://doi.org/10.1038/s41598-018-29883-9>. Published by Nature. All Rights Reserved. The chapter is identical to the Supplementary Materials of the publication except for a modification of the caption of Figure S10.

SCIENTIFIC REPORTS



OPEN

The surge of earthquakes in Central Oklahoma has features of reservoir-induced seismicity

Lisa Johann , Serge A. Shapiro & Carsten Dinske

The recent surge of seismicity in Oklahoma and Kansas is related to fluid disposal. Evidences suggest that critical parameters are the injection volume as well as injection depth but dominant physical processes and a corresponding model to describe the physics are still not clear. We analyse the spatio-temporal distribution of induced earthquakes in the basement and find visible signatures of pore pressure diffusion and poroelastic coupling, features which strongly resemble seismicity induced by the filling of artificial lakes, so-called reservoir-induced seismicity. We developed a first-principle model of underground reservoir-induced seismicity. The physics of the model are based upon the combined mechanisms of fluid mass added to the pore-space of the injection layer and acting as a normal stress on the basement surface, pore-fluid pressure diffusion in the basement as well as poroelastic coupling contributing to the pore-fluid pressure and stress. Furthermore, we demonstrate that underground reservoir-induced seismicity occurs preferably in normal faulting and strike-slip settings, the latter being prevalent in Oklahoma. Our model explains observed injection volume and depth dependence of the seismicity and should be considered as a basis for future hazard prediction and prevention as well as for planning possible disposal sites.

Starting in 2009, an unexpected burst of earthquakes has struck the central U.S.^{1,2}. Whereas only about one magnitude $M \geq 3$ earthquake happened per year in north-central Oklahoma before 2009, approximately 900 $M \geq 3$ events were recorded in 2015³. It is now widely understood that this acceleration of seismic activity is linked to the injection of huge volumes of waste water through salt water disposal (SWD) wells^{2,3}. Most of these wells inject into the highly permeable, underpressured Arbuckle aquifer which is hydraulically connected to the underlying crystalline basement where most of the seismicity occurs. In reaction to the strong increase of earthquakes, the Oklahoma Corporation Commission (OCC) Oil and Gas Division called for a 40% reduction of the 2014 injection volume in Central Oklahoma to be completed in mid- 2016.

Numerous studies on mechanisms explaining the spatio-temporal evolution of the observed fluid-disposal induced seismicity have been published to date. There are indications that the injection volume as well as injection depth affect the seismic activity⁴. However, it remains a challenging task to assess the governing physical processes because they are assumed to deviate from the ones which control seismicity induced by high-pressure reservoir stimulations^{5,6}. For the case of Oklahoma, firstly, events occur in the deeper basement and not directly in the overlying injection formation. Secondly, seismicity is also observed over broad areas far from injectors. And thirdly, unlike in the case of pure pore-fluid pressure diffusion where the spatio-temporal event evolution is enveloped by a triggering front⁷, the time and location of earthquakes in Oklahoma does not clearly obey such a behaviour⁸. Published models include pore-fluid pressure diffusion^{2,3} as well as poroelastic fluid-solid coupling effects⁸⁻¹¹. Yet, the controlling mechanisms of seismic activity in Oklahoma are still not fully understood. Since the number of damaging earthquakes poses a risk not only to infrastructure and buildings but also to human life, a model capable of explaining spatio-temporal features of the seismicity is fundamental for seismic hazard mitigation.

Considering the scenario of large-volume waste water disposal and using knowledge of the concept of seismicity induced by the filling of surface water reservoirs, known as reservoir-induced seismicity (RIS)¹²⁻¹⁴, we developed a new first-principle model called *underground reservoir-induced seismicity* (URIS). Our studies demonstrate that such a model is able to capture the spatio-temporal evolution of the observed seismicity in Central Oklahoma. To draw the connection between URIS and RIS, we assume that the rapid increase of fluid disposal rates in the

Freie Universitaet Berlin, Institute of Geophysics, Berlin, 12249, Germany. Correspondence and requests for materials should be addressed to L.J. (email: lisa.johann@geophysik.fu-berlin.de)

highly permeable Arbuckle formation corresponds to the filling of a large subsurface reservoir. As a consequence, pressure and stress changes in the underlying basement are observed. Accepting that the basement acts as a poroelastic half-space, it is a combination of physical mechanisms that result in pressure- and stress changes in the basement. These mechanisms are the direct effect of mass added to the injection formation (here the Arbuckle aquifer), pore-fluid pressure diffusion in the crystalline basement as well as poroelastic coupling.

We derive an analytical solution for the corresponding initial value poroelastic uniaxial strain problem with constant boundary conditions. Our derivation is directly based on previously elaborated approaches for poroelastic effects of injections and RIS effects^{14–26}. Using hydrological and elastic parameters for Oklahoma from literature, analytical pore-fluid pressure and stress solutions are compared to results obtained by finite element modelling. As the ambient stress and pressure states influence the occurrence of RIS¹², we transfer this knowledge to the case of URIS by computing the change in failure criterion stress for different tectonic stress regimes. We then account for the time of fluid accumulation in the Arbuckle formation by defining a time-dependent boundary condition for the pressure and stress acting on the basement top. We solve analytically for such a boundary condition problem, generate synthetic event catalogues for a strike-slip regime and analyse spatio-temporal features of the events. Concluding the work presented here, we compare patterns of synthetic seismicity to Central Oklahoma events.

Our results suggest that, equivalently to RIS, the background stress regime has to be taken into consideration in the URIS model. This is a direct consequence of the poroelastic coupling effect. However, unlike in the case of RIS, filling of an underground reservoir in a thrust faulting regime also induces a destabilisation front which evolves with time from the reservoir bottom. In contrast, in a strike-slip regime, as existing in Central Oklahoma²⁷, the domain of destabilisation grows rapidly from the bottom of the Arbuckle formation. A sensitivity study confirmed that the choice of parameters affects the medium destabilisation, yet in the range of general event location uncertainties.

As the application of the URIS model to Oklahoma induced events captures well the depth and time evolution of the observed seismicity, our approach should be considered in future research to reduce the risk posed by the anthropogenic events.

Results

Central Oklahoma Seismicity. Recently, Langenbruch and Zoback³ found that seismicity in the area of Central Oklahoma started in 2009 after a monthly injection volume threshold of $3.6 \times 10^6 \text{ m}^3$ had been exceeded. According to the authors, this injection rate sets an upper limit to fluid volumes which can be incorporated into the hydraulic system. If injection rates are higher, *in-situ* stresses are locally modified which in turn might lead to the occurrence of seismic events. The volume reduction plan decreed by the OCC in consequence of the accelerated seismicity rate³ appears to have lowered seismicity rates in the period 2015 to the present²⁸. Still, there is an ongoing debate on whether or not the probability of larger-magnitude events is also declining^{3,8}. Moreover, it was shown that the total seismic moment in Oklahoma has decreased only moderately⁴.

We focus on a catalogue of relocated events published by Schoenball and Ellsworth²⁹. This database includes Oklahoma events that occurred between May 2013 and November 2016. Following the hypocentre locations, most of the seismic activity is distributed along previously unknown basement faults and might occur at large distances of up to 40 km from the wells^{8,29,30}. This observation points to complex poroelastic coupling effects rather than pure pore-fluid pressure diffusion⁸.

We restrict the event catalogue to an area which we define as Central Oklahoma (COH), bounded by longitude $[-97.7^\circ, -96.7^\circ]$ and latitude $[35.5^\circ, 36.5^\circ]$, shown in Fig. 1. Our analysis requires high-precision depth locations, thus we neglect events with depth errors $\delta z > 0.5 \text{ km}$ (Fig. S1). In a later work, Schoenball and Ellsworth³⁰ demonstrated that most of the seismicity occurs in sequences with significant fore- and aftershock activity, probably caused by earthquake interaction such as static stress transfer. To exclude these events, we declustered the catalogue (see Supplementary Materials, Fig. S2). As expected, the main shocks now follow a homogeneous Poissonian distribution in time with a magnitude of completeness $M_c = 2.4$ (Fig. S3). Most of the seismicity with magnitude $M \geq M_c$ occurs at depths between 5 and 7 km below the surface (Fig. 1). Correlating these depths with the top of the basement (TOB) derived from well data³¹ (grey surface in Fig. 1B,C), hypocentres lie within the upper 2 to 4 km of the basement. With time, the seismogenic zone shifts to greater depths (Figs 1D and S10A).

Features of Reservoir-Induced Seismicity. More than 70 years ago, Carder³² noted a positive correlation between the water level of Lake Mead, Nevada/Arizona (U.S.), and seismicity nearby. In the 1960s, a number of damaging earthquakes occurred in India (Koyna, 1967, $M6.3$), China (Hsingfengkiang, 1962, $M6.1$), Zimbabwe (Kariba, 1963, $M5.8$) and Greece (Kremasta, 1966, $M6.3$), all of which are nowadays understood to be linked to lake level changes¹². It is widely accepted that the seismicity is induced by perturbations of the ambient stress field. Based on the theory of poroelasticity^{15,19,33}, consider a poroelastic half-space extended in the vertical z -direction. On the upper boundary, vertical stress and pore-fluid pressure are applied. The stress corresponds to the weight of the water column in the reservoir whereas the pore-fluid pressure is defined by the pressure below the reservoir. Assuming a permeable reservoir bottom, the pressure can diffuse into the pore space of the underlying formation. Clearly, all quantities are functions of the depth z and the problem becomes one-dimensional^{14,17,18,20,26}. Due to the loading, an instantaneous response of the poroelastic, undrained rocks can be observed in terms of pressure and stress changes. Additionally, pore-fluid pressure diffusion leads to a delayed pressure increase in the basement. Both effects may cause shear failure along pre-existing, favourably oriented and critically stressed fractures²².

We here accept the continuum mechanic notation that compressive stresses are negative. Thus, the quantities σ_1 , σ_2 and σ_3 are equal to the principal stresses multiplied by (-1) and $\sigma_1 > \sigma_2 > \sigma_3$, where σ_1 , σ_2 and σ_3 denote absolute magnitudes of the maximum, intermediate and minimum principal compressive stress. Following the concept of the failure criterion stress FCS :

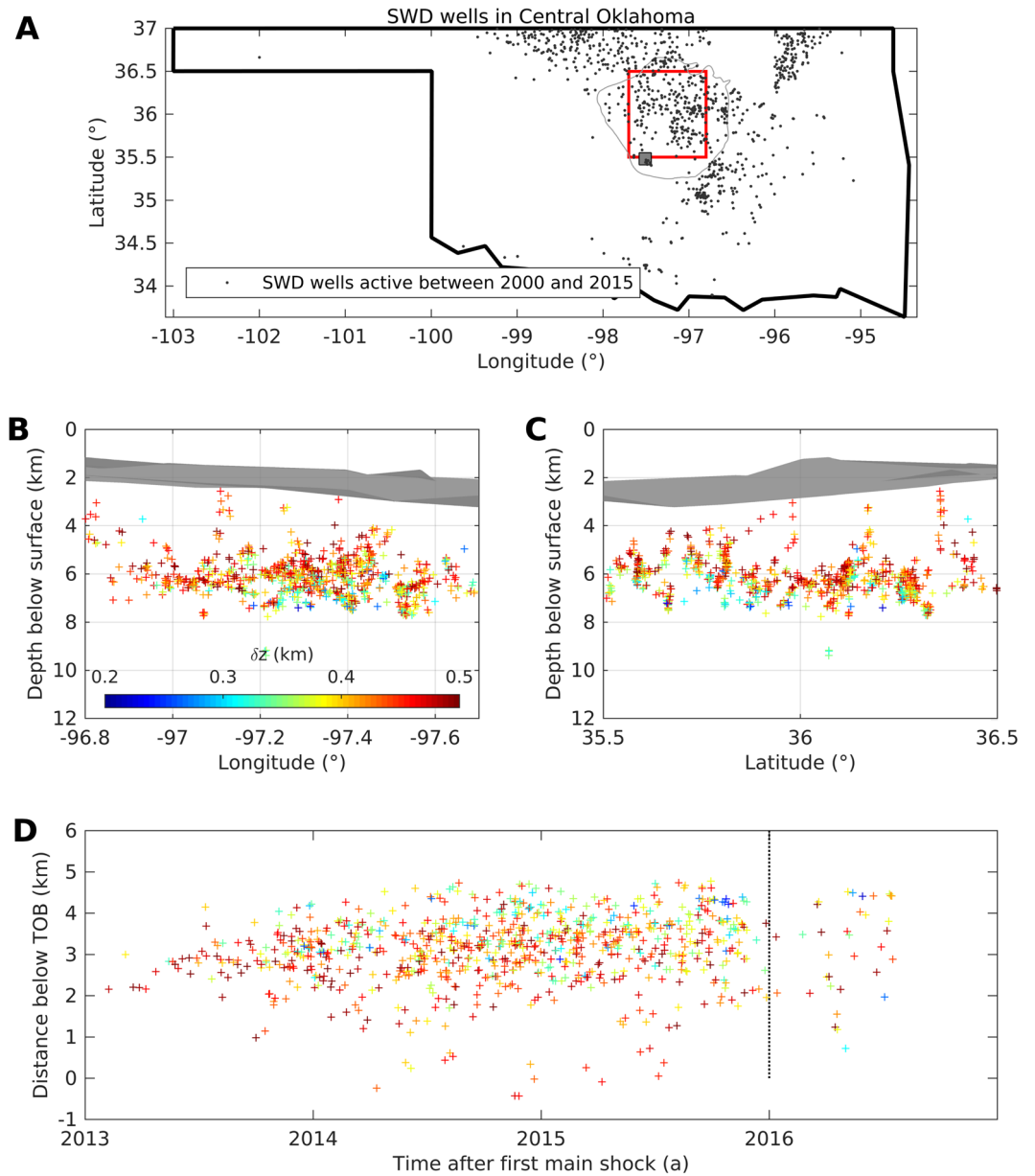


Figure 1. Seismicity in Central Oklahoma from May 2013 to November 2016. The map (A) depicts our study area (Central Oklahoma), bounded by latitude 35.5° to 36.5° and longitude −97.7° to −96.8° (red square). Panels (B,C) show event depths (colour-coded by depth uncertainty) and the top of the basement (TOB, grey surface) relatively to the ground surface elevation. In panel (D), event distances below the TOB are plotted versus their occurrence time. Year 0 denotes the time of the first event included in the catalogue on 5 May 2013. Event locations were published by Schoenball and Ellsworth²⁹, including only events with vertical errors $\delta z < 0.5$ km and with a magnitude larger than the magnitude of completeness obtained from the Gutenberg-Richter relation (see Supplementary Materials). The depth of the TOB was derived from well data³¹.

$$FCS = \frac{\sigma_d}{2} - \sin \varphi (\sigma_m - p), \tag{1}$$

optimally oriented fractures are activated in the case of $FCS > 0$. Further, destabilisation occurs if the variation ΔFCS is positive: $\Delta FCS = \frac{\Delta \sigma_d}{2} - \sin \varphi (\Delta \sigma_m - \Delta p) > 0$ (we assume other parameters, including the cohesion, unaffected). In the above equations, $\sigma_d = \sigma_1 - \sigma_3$ and $\sigma_m = (\sigma_1 + \sigma_3)/2$ are the differential and mean stress, respectively, and p is the pore-fluid pressure. Further, φ denotes the angle of internal friction which is related to the friction coefficient μ_f by $\mu_f = \tan \varphi$.

Previous works noted that RIS might also occur at large distances from the water in the reservoir. It follows that stress changes in the order of 0.1 MPa are sufficiently high to induce seismic events³⁴. Additionally, it was

shown that the stress regime near the reservoir significantly affects the occurrence of RIS^{12,24}. Theoretically, the increasing vertical stress caused by the filling of the reservoir in a normal faulting regime contributes to the vertically oriented maximum principal stress. This leads to a higher differential stress. In a thrust faulting regime where the vertical stress corresponds to the minimum principal compressive stress, the additional load stabilises locations below the reservoir. This theory has been reviewed for several reservoir locations worldwide^{12,24,35}. Indeed, most of the earthquakes which are associated with positive changes of the water level occur in normal faulting or strike-slip regimes. Examples are the Koyna-Warna reservoirs in India^{14,24,36} and the Aswan Dam in Egypt, Africa³⁷, respectively. In contrast, events associated with reservoir impoundment located in thrust faulting tectonic regions correlate with unloading of the reservoir, e.g. the Tarbela dam in Pakistan³⁸.

The Conceptual Model of Underground Reservoir-Induced Seismicity. Previous studies demonstrated that seismogenic processes in the study area are rather complex, leading to a debate on governing physical mechanisms^{8,11}.

The model approach developed in this work is based upon the concept of RIS (e.g. ^{12,24}), motivated by the following observations: Firstly, due to the slightly underpressured Arbuckle aquifer³⁹, waste water in the study area is usually disposed by gravity³⁰. In contrast, injection pressures at Enhanced Geothermal Systems or for shale gas production by hydraulic fracturing amount to multiples of the *in situ* formation pressure. Secondly, unlike the rather local effect of high-pressure fluid stimulations, numerous disposal wells cover the study area which includes also large fault zones^{29,30,40}. Thirdly, disposed cumulative fluid volumes in Central Oklahoma were reported to be as high as 200 million cubic meter³, i.e. much larger than those injected for fluid stimulations. Lastly, seismicity also occurs at large distances not directly connected to single injectors⁸. The same observation has been noted in previous studies on RIS, where the event locations are remote from the water column (see e.g. ³⁴). Thus, poroelastic coupling effects might play an important role.

On this basis, our conceptual model deviates from the classic fluid injection scenario such as for geothermal exploration or hydraulic fracturing for shale gas production. We used the knowledge of RIS to assess seismicity patterns in Central Oklahoma. Adapting this concept to the case of waste water disposal, we call the model *underground reservoir-induced seismicity* (URIS), shown in Fig. 2A.

The fluid injected into the underpressured, highly porous and very permeable Arbuckle formation creates an additional pore-fluid pressure as well as an additional vertical elastic (confining) stress. As injection rates were as high as $13 \times 10^6 \text{ m}^3$ per month in Central Oklahoma³ and the crystalline basement has a low permeability, the fluid is expected to form a layer of a certain height Δh on top of the basement in a depth z_0 . Note that an exact location of the fluid above the basement top has no significance in terms of the basement loading. Thus, we refer to this situation as an *effective* fluid layer. Such a layer with a higher averaged water column is formed along the seismogenic area overlain by the Arbuckle aquifer. However, we note that because of the extremely high permeability of this formation, this effective water layer is not necessarily concentrated in vicinity to the injection borehole. Returning to the case of RIS, the layer is comparable to the water level in a surface reservoir (artificial lake).

Accepting that the underlying basement acts as a poroelastic half-space, it is a combination of physical mechanisms that induce pressure- and stress changes of the ambient pore-fluid pressure- and stress state in the crystalline. These are the direct effect of mass added to the injection formation and poroelastic coupling which lead to an instantaneous increase of the pore-fluid pressure in the basement, as well as pore-fluid pressure diffusion in the crystalline basement, provoking a delayed increase in pore-fluid pressure.

With the above condition, the 1D poroelastic formulation is applicable^{16,17,19,21,25,26}. Modifying equations (2.186)–(2.188) of²⁶ for gravity which acts in the vertical z -direction, we derive analytical stress and pressure solutions for a constant boundary condition p_0 (see Methods' Section). In addition to the analytic solution, we developed a finite element model (FEM, see Supplementary Materials and Fig. S4) verified by the analytical pore-fluid pressure and stress solutions.

Application of URIS to Central Oklahoma. We applied the URIS model to the study area using hydraulic and elastic parameters from literature^{10,41}, knowledge of the local geology²⁷ and reported data from waste water disposal³.

Figure 2B–D, shows computed pressure and stress changes (Δp and $\Delta \sigma$). As the analytic and numerical values coincide, the FEM serves as a basis for future studies. Δp (B) is characterised by two effects: The instantaneous response of the elastic, undrained medium causes the constant value which is approached at greater depth. This effect is superimposed by the delayed response due to pore-fluid pressure diffusion which yields the distinct time-dependent shape of the profiles. The vertical stress perturbation $\Delta \sigma_z$ (C) is constant in time and depth with magnitude p_0 , whereas the horizontal stress perturbation $\Delta \sigma_x$ (D) is time- and depth-dependent.

The Influence of the Tectonic Setting. We used analytic pressure and stress solutions to calculate ΔFCS for different tectonic settings (Fig. 3 and Supplementary Materials). Additionally, we introduced the destabilisation front as a measure for the spatio-temporal evolution of the medium destabilisation. In a normal faulting regime, the whole domain is brought closer to failure immediately (Fig. 3A,B), whereas the front migration is strongly delayed for thrust faulting (Fig. 3E,F). In a strike-slip regime (e.g. in Oklahoma) the destabilisation evolves quickly from TOB to greater depths (Fig. 3C,D).

Sensitivity to Parameters. The model described above depends on a number of hydraulic and elastic parameters which might be subject to large uncertainties. Aiming at evaluating the model outcome in terms of the parameter choice, we performed a sensitivity analysis, known as 'one-at-a-time' (OAT)⁴² (see also Supplementary Materials).

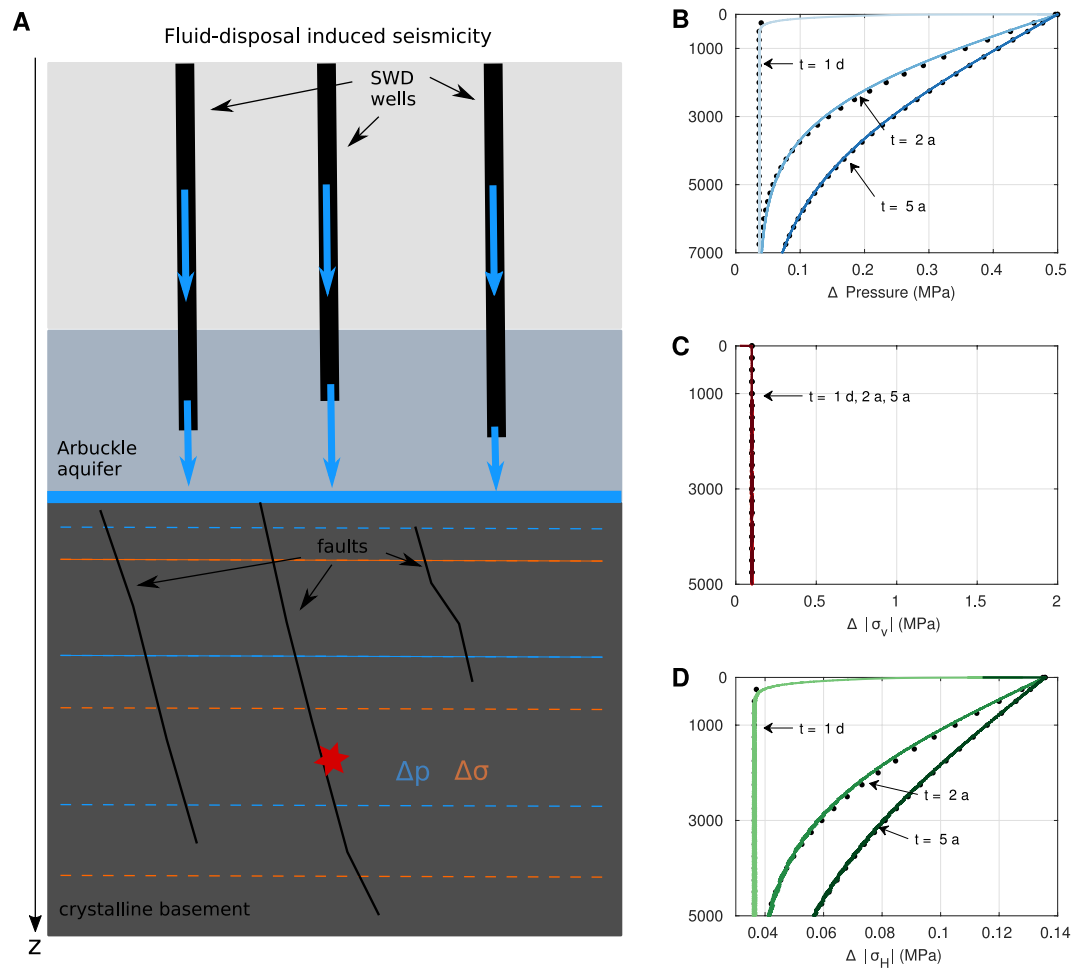


Figure 2. The conceptual model of underground reservoir-induced seismicity (URIS) and pressure and stress solutions. **(A)** Salt water disposal (SWD) wells (black bars) inject into the highly permeable Arbuckle aquifer (grey-blue square). As the basement has a low permeability, the injected fluid forms an effective layer of height Δh (blue layer) on top of the basement (dark grey). Such a scenario can be considered as the filling of an underground reservoir. Caused by the weight of the water column and the pore-fluid pressure beneath Δh , stress- and pressure changes penetrate the poroelastic basement (dashed orange and blue lines, respectively). The perturbation of the ambient stress state may cause shear failure of pre-existing, optimally oriented, critically stressed faults. Changes of pressure **(B)** and stress **(C,D)** as profiles along the depth for times 24 h, 2 a and 5 a (colour-coded from light to dark) obtained from the analytic solution (black dots) and FEM (solid lines) for a constant boundary condition p_0 . Pore-fluid pressure profiles are marked by the distinct diffusion-like shape of the profile. With increasing time, the pressure in the medium increases. The maximum principal stress σ_1 acts in vertical direction and is constant with time. In contrast, the minimum principal stress σ_3 is horizontally oriented and time-dependent.

The OAT was run for six hydraulic and elastic parameters which govern the analytic equations (equations 12 to 15). These are the hydraulic diffusivity of the basement D , the porosities of the injection formation Φ_{Ar} and the basement Φ , the bulk modulus of the pore fluid K_f , the P-wave modulus of the drained rock matrix $P_{mod,dr} = \lambda_{dr} + 2G_{dr}$ and the parameter $\Gamma = n_s/(SG_{dr})$, which characterises the strength of the poroelastic coupling.

As demonstrated in Fig. 4, ΔFCS increases most significantly with D , Γ and $P_{mod,dr}$ and decreases strongly for higher Φ . Yet, the dependence is also controlled by the time and location. For example the impact on ΔFCS by Γ intensifies with depth, indicating that poroelastic coupling is the controlling mechanism at larger depths. The parameter dependence is also revealed by the destabilisation front. Its spatio-temporal evolution is controlled by ΔFCS and thus, by the parameters described above (see Supplementary Materials, Fig. S6).

As known from cases of RIS, the interplay between the water level and the stress regime contributes to the occurrence of seismicity. An additional study on the influence of p_0 in different tectonic regimes (Supplementary Materials) indicates that negative p_0 , i.e. fluid discharge from the overlying permeable formation, stabilises the underlying low-permeable medium in a strike-slip regime (Figs S7, A,B and S8, red line) but brings this medium closer to failure in a thrust faulting regime (Figs S7, E,F and S8, green line). The latter observation has also been made for RIS³⁸ and implies the importance of considering poroelastic coupling in the URIS model.

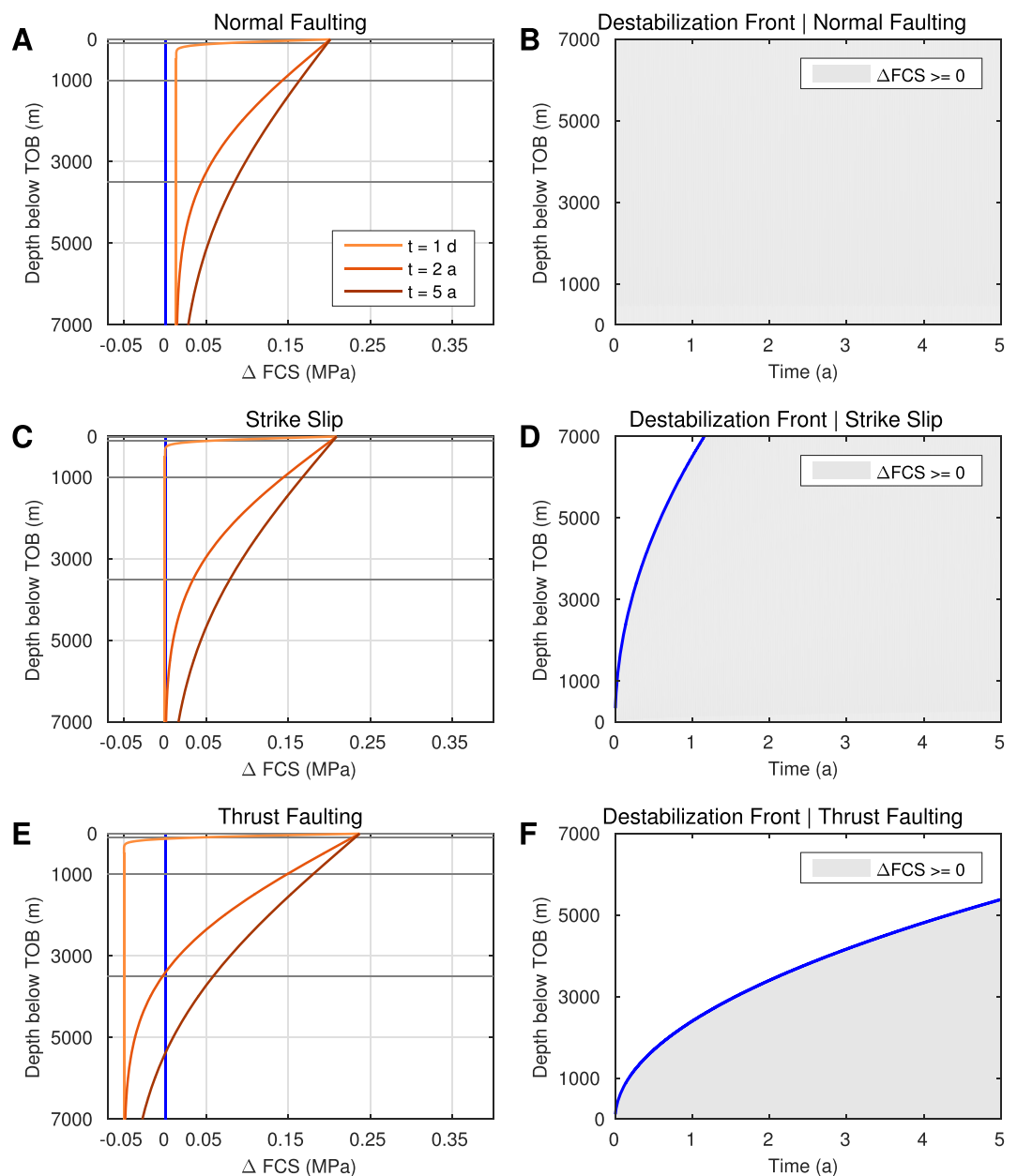


Figure 3. Failure criterion stress and the destabilisation front for different tectonic settings. Based on the analytic solution, ΔFCS is computed for a normal faulting (A), strike-slip (C) and thrust faulting (E) regime. The components of ΔFCS (orange) are illustrated for times 24 h, 2 a and 5 a (colour-coded from light to dark). While the medium is stable for $\Delta FCS < 0$, pre-existing, optimally oriented fractures are destabilised if ΔFCS turns positive. The location of this transition point can also be expressed in terms of the destabilisation front (blue line, (B,D) and (F)).

Time-dependent Boundary Condition. Barbour *et al.*¹¹ showed that varying injection rates significantly influence poroelastic effects. Since URIS is based on the assumption of an effective fluid accumulation on top of the basement which depends on the injection rates, we defined a time-dependent boundary condition $p_0 = p_0(t)$ at the TOB to complement our study.

The evolution of $p_0(t)$ (Fig. 5A, black line) is computed using the monthly injected fluid volume $Q(t)$ in our study area³ (Fig. 5A, blue line). After the triggering threshold had been reached in 2009, seismicity rates in Central Oklahoma significantly increased. Thus, we assume that fluid began to effectively accumulate on top of the basement by that time (model time $t = 0$ a). Since injection rates are not given for times after 15 Dec 2015, we extrapolate for dates until 15 Dec 2018 on a constant value based on the Volume Reduction Plan (see Introduction section). Calculating $\int_0^t Q(\tau) d\tau$ yields the magnitude of $p_0(t)$ divided by a factor Ω . Here, Ω depends on the size of the study area, the fluid density and the gravitational acceleration constant.

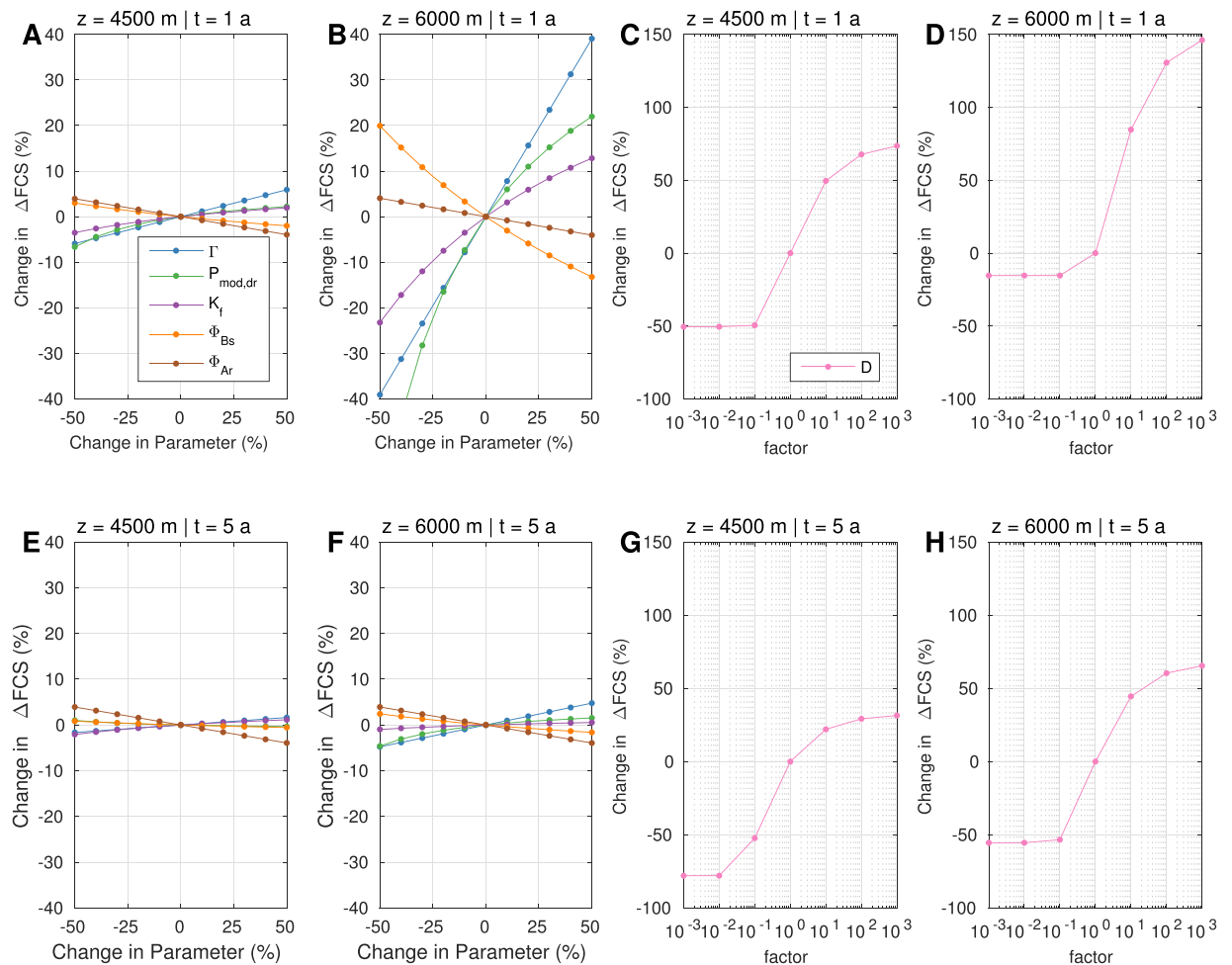


Figure 4. Deterministic sensitivity analysis of input parameters for a strike-slip regime. To account for parameter uncertainties, a sensitivity analysis was performed for hydraulic and elastic parameters Γ , $P_{mod,dr}$, K_f , Φ_{Bs} and Φ_{Ar} (coloured lines, **A,B,E,F**), perturbed incrementally between $\pm 50\%$ while holding the other values at their base values. In contrast, the hydraulic diffusivity D (**C,D,G,H**) was varied logarithmically between $[1e-3$ and $1e3]$ times the base value. The panels show classical sensitivity plots for 1.5 km and 3 km below the TOB at times 1 a and 5 a (top and bottom). The influence on ΔFCS is studied relatively to the base level outcome. In the Supplementary Materials, we additionally demonstrate the influence of the boundary pressure p_0 for different tectonic regimes.

Using $p_0(t)$, we solved for the analytical pressure and stress equations 12–15 (Fig. 5B–D). As for the constant boundary condition, the change of the vertical principal stress is independent of the depth but as p_0 changes with time, this stress becomes a function of time.

Synthetic Seismicity versus Central Oklahoma Seismicity. Increasing shear stress, decreasing normal stress, as well as a reduction of the effective normal stress due to higher pore-fluid pressure can be assumed to increase the failure stress FCS . If these changes are larger than a critical threshold value, a seismic event is triggered^{26,43}.

Based on that idea, we apply the triggering criterion introduced by Rothert and Shapiro⁴⁴: $\Delta FCS(z,t) \geq C(z)$ for the generation of synthetic events. Here, ΔFCS is the change in failure criterion stress, obtained from the analytical solution. The quantity $C(z)$ characterises the strength of pre-existing fractures and faults (criticality) and is governed by rock parameters and the tectonic setting. Seismicity can only happen at locations where the criticality is low, meaning at locations close to failure. At each time step, the value of ΔFCS is compared to the local critical value $C(z)$. If the triggering criterion is full-filled, a seismic event is triggered and the critical value is set to infinity to exclude multiple triggering at one location.

For the computation of ΔFCS , recall that we set $\Delta\sigma_H = \Delta\sigma_n$, justified by the plane strain model (see Supplementary Materials). Thus, in a strike-slip regime $\Delta\sigma_m = \Delta\sigma_h$ and $\Delta\sigma_d = 0$ (shown in Fig. S9). Figure 6A shows profiles of ΔFCS along the depth below the TOB for the dates 15/01/2010, 15/01/2013, 15/01/2015 and 15/12/2018. Driven by the diffusion of pore-fluid pressure, destabilisation of the medium evolves with time from the TOB to the deeper basement. The constant value of p reached at greater depth can be attributed to the elastic response of the medium due to poroelastic coupling effects.

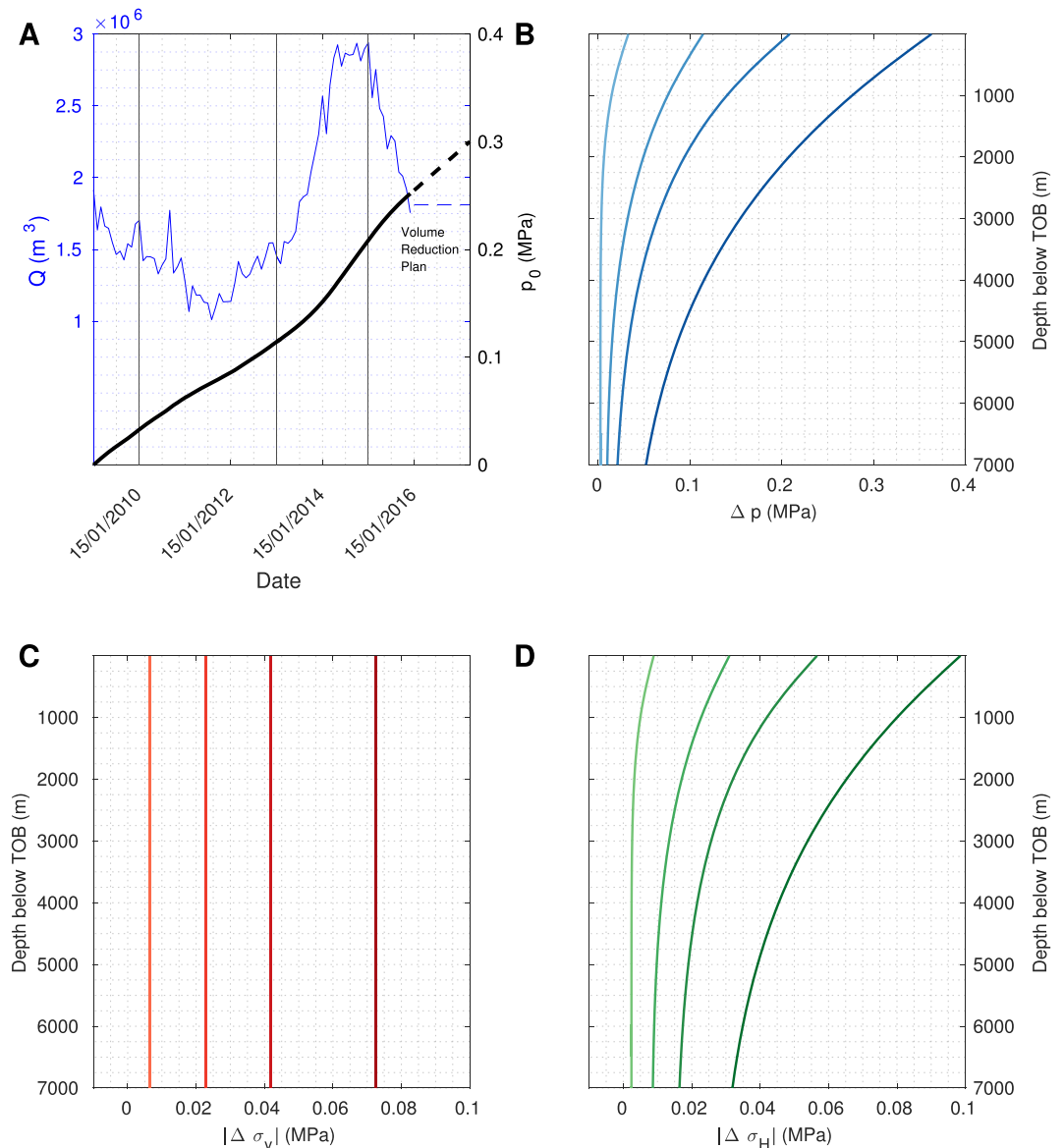


Figure 5. Analytic pressure and stress solutions for a time-dependent boundary condition. To study the influence of the time that the fluid needs to accumulate at the TOB, a time-dependent boundary condition for p_0 is defined, based on the injection rate in our study area between 01/2009 and 12/2015 (blue line, panel (A)). We extrapolated the data until 12/2018, using information of the Volume Reduction Plan, to allow for predictions of the seismicity rate after 12/2015. Calculating $\int_0^t Q(\tau) d\tau$, yields $p_0(t)$. Solving analytically for equations (2)–(5) and subtracting the gravity effect yields changes of the pore-fluid pressure (B), the vertical (C) as well as the horizontal (D) stress. Colour-coding shows the corresponding profile along the depth for times 01/2010, 01/2013, 01/2015 and 12/2018 (light to dark colours). In spite of the fact that the pressure perturbation is generally higher than stress changes, at some depths and times they can have the same order of magnitude. This results in various signatures of URIS under different stress regimes and is a direct result of the poroelastic coupling.

The criticality field $C(z)$ is calibrated on the basis of the spatio-temporal evolution of events in Central Oklahoma as well as on geological features in the study area. This is a first step necessary for the modelling. Accepting that faults close to failure exist in the basement of Central Oklahoma²⁹, we define the magnitude of C by log-normally distributed statistically random numbers which means comparatively more low critical stress values (see Methods' section). Moreover, seismicity in the study area neither occurs in the injection formation (Arbuckle aquifer), nor in the top layers of the basement. Thus, further assumptions have to be made. It has been noted that especially larger magnitude earthquakes happened in zones of increased P-wave velocity, corresponding to tectonically weak areas. On the contrary, hardly any seismicity is observed in regions of low v_p/v_s ratios which exist in the upper basement⁴⁰. Therefore, we define a number of locations with a relatively smaller value of $C(z)$ at depths between 2 km and 5 km below the TOB as well as higher values in the upper basement (small values of $C(z)$ mean that locations are closer to failure). Overall, the statistics of $C(z)$ still follow a log-normal distribution (see Fig. 6B).

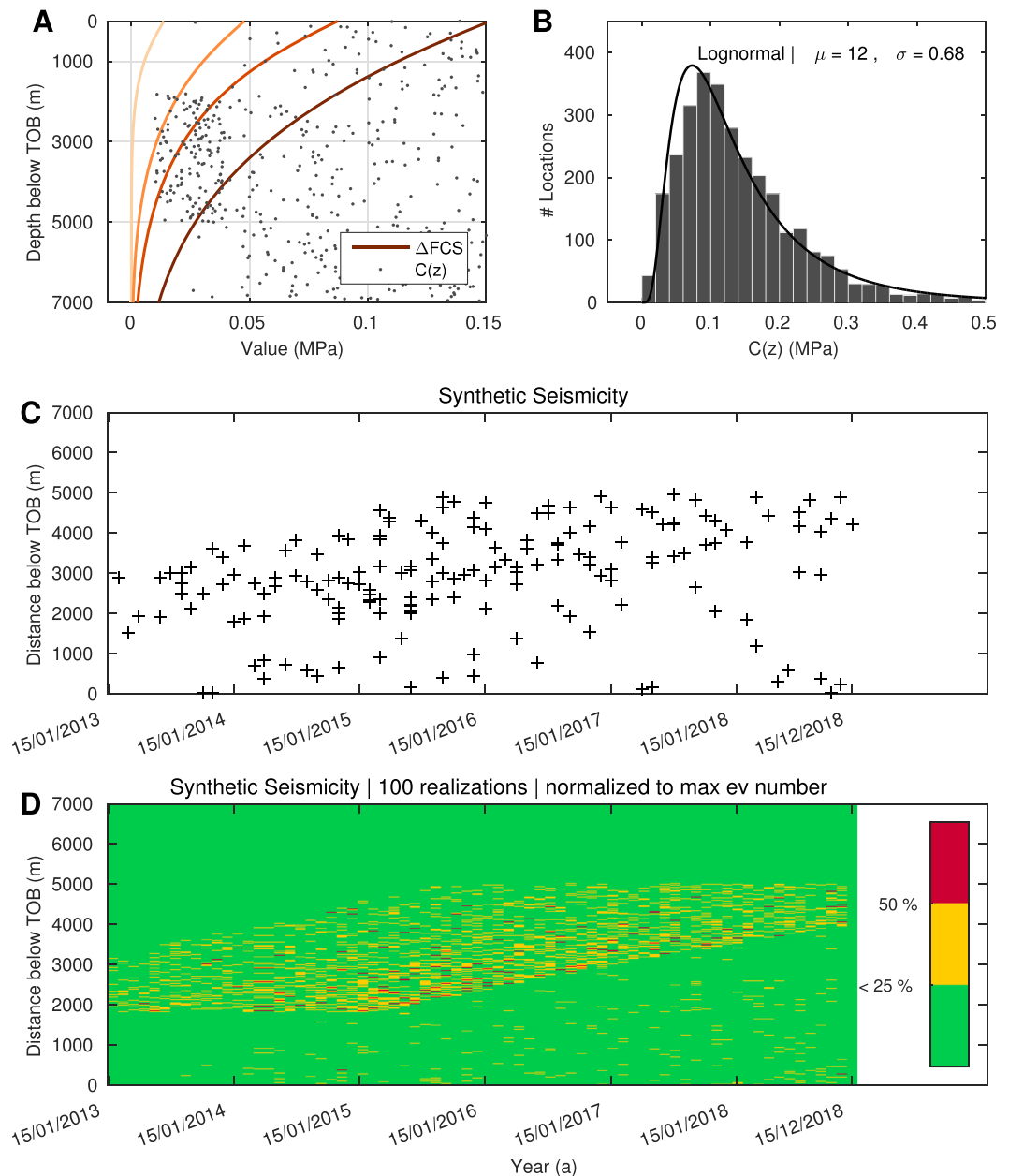


Figure 6. Generation of synthetic seismicity. Accepting that Central Oklahoma is characterised by strike-slip conditions, ΔFCS is calculated (A) using analytical pressure and stress solutions for a time-dependent p_0 (Fig. 5). The triggering criterion $\Delta FCS(z, t) > C(z)$ can then be used for the generation of synthetic events. Here, $C(z)$ is the log-normally and heterogeneously distributed criticality (B). An $r-t$ -plot of the event cloud (C) for the interval 01/2013 to 12/2018 illustrates that the farthest events occur 5000 m below the TOB. This result is stable, evaluating 100 random realisations of $C(z)$ (D). Regions which are most likely to fail are marked in red (locations failed in >50% of the 100 runs).

Spatio-temporal characteristics of the simulated events are graphically presented in an $r-t$ -plot (Fig. 6C) for the time 01/2013 to 12/2018. Whereas the main activity occurs between 2 km to 5 km below the TOB, rather little activity is observed close to the basement top. Taking into account 100 realisations of $C(z)$, this result is confirmed to be stable (Fig. 6D). At the time of the burst in seismicity in 2013, locations most prone to failure (yellow and red) occurred in depths of up to 3 km below the TOB. With time, the seismogenic zone shifts to greater depths but not deeper than 5 km below the TOB (Fig. S7B).

These spatio-temporal features are in general agreement with the analysed Central Oklahoma main shocks observed between mid-2013 and early 2016 (Figs 1 and S7A): Between 2013 and 2016, the seismogenic zone extends between 2–5 km below the TOB, whereas rather little activity is observed close to and deeper than 5 km below the TOB. Furthermore, the maximum event depth migrated from 3 km to 5 km below the TOB and the mean event depth shifted from 2.5 km to 4 km below the TOB.

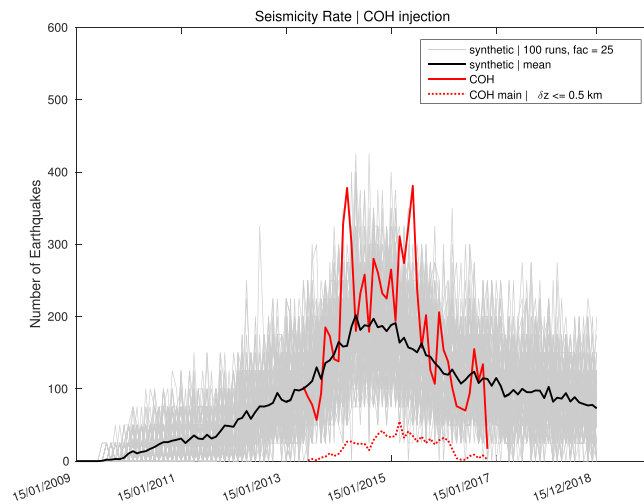


Figure 7. Seismicity Rates for observed and synthetic events. An important feature of earthquakes induced in Oklahoma is the seismicity rate. Using the whole catalogue for the study area Central Oklahoma (COH)²⁹, the event number started to increase in 2013 and decayed in early 2016. Calculated synthetic rates for 100 realisations of $C(z)$ (grey lines) resolves the observed temporal behaviour (the mean is marked by the bold black line) and thus, should be considered as suitable for predictions on the seismic response to varying injection rates.

Regarding seismicity rates we do not depend on high-precision localised events. Thus, in the following, we focus on the complete catalogue of relocated events in the study area. As shown in Fig. 7, seismic activity significantly increased in 2013 and started to decay in late 2015, continuing at least until the time of the last event comprised in the data in November 2016 (compare to Fig. 1 in Langenbruch and Zoback⁴⁵). Comparing this trend to synthetic event rates, we find that our model is supported by the observation of decreasing rates throughout 2016. Using the predictive nature of our model until 15/12/2018, we find that the declining number of events persists throughout that interval. This observation is in agreement with a recent study by Langenbruch and Zoback^{3,45}.

Discussion

We extended the model of URIS caused by the filling of artificial lakes to seismicity induced by high-volume underground fluid disposals, URIS.

Overall, the results show that URIS preferably occurs in normal faulting or strike-slip tectonic regimes and is time-delayed in thrust faulting. That is a noteworthy difference from RIS. The sensitivity study demonstrated that the consideration of poroelastic coupling plays an important role for URIS. In a strike-slip regime, the poroelastic effect controls the change of the failure stress at greater depths and early times.

For the application of the URIS model to Central Oklahoma, we defined a time-dependent boundary condition $p_0(t)$ based on reported values for the monthly injected fluid volume in the study area between 15/01/2009 and 15/12/2015. To include the possibility of predictions for the time after 2015, we extrapolated the injection rate until 12/2018 to a constant value following from the Volume Reduction Plan of OCC (i.e. a 40% reduction of the total volume injected in 2014).

Using the obtained values of the change in failure criterion stress for a strike-slip tectonic setting, a catalogue of synthetic events was generated. Whereas little activity occurs close to the top of the basement, a larger number of events is observed between 2 and 4 km below the basement top. These larger event depths might be attributable to the instantaneous elastic response of the rock matrix. With time, the mean event depth migrates to greater depths which can be explained by the time-dependent pore-fluid pressure diffusion. Overall, the evolution of events in time and depth coincides with the event distribution observed in Central Oklahoma.

Our findings demonstrate that the presented novel physical model of URIS captures spatio-temporal features of the seismicity that was observed in Central Oklahoma within the last decade. Additionally, we demonstrated that our model resolves well the seismic response to the injection rate in the area of interest. Therefore the approach has a predictive power for the seismicity rate even in case of decaying fluid disposal rates.

To conclude, the work presented here will help in understanding controlling physical processes related to high-volume fluid injections such as waste water disposal. This is of importance for hazard assessment and seismic risk mitigation not only in Oklahoma but globally.

Model Limitations. We note that the model developed here comprises only principal features of the phenomena.

First, regarding the spatio-temporal evolution of seismicity linked to waste water injections, it is the interaction of various parameters that controls the magnitude and number of events. Not only does this include the magnitude and orientation of pre-existing stresses, but also the orientation of faults, the injection trajectory¹² as well as hydraulic and elastic parameters. The influence of parameters on ΔFCS was investigated in a sensitivity study. At this point, the application of OAT to the pressure- and stress solutions is a first step before implementing

more time-consuming global sensitivity analyses combined with a 3-D numerical model and Monte Carlo simulations. Accepting the destabilisation front as a measure for the spatio-temporal seismicity evolution, it should be noted that the event distribution is indeed influenced by the parameters used in this study. Yet, within parameter variations of $\pm 10\%$, the location of the front is still within the range of event location uncertainties.

Second, the injection scenario in the area of interest is rather complex. We do not compute exact boundary pressures and stresses at the TOB for each injector but rather consider a cumulative volume for all injectors in Central Oklahoma. Additionally, the assumption of a constant injection rate after 12/2015 evokes uncertainty in the predictive nature of our modelling results after 12/2015.

Third, the spatio-temporal evolution of synthetic events is clearly influenced by the definition of the criticality field $C(z)$. However, the choice of values is justified by the distribution of observed earthquakes as well as geologic features in the study area. Performing P wave tomography in Oklahoma, Pei *et al.*⁴⁰ suggest that seismicity in that area tends to occur in high-velocity regions which can be found in the deeper basement. In contrast, the upper basement is characterised by low v_p/v_s ratios. Thus, geological structures seem to control earthquake locations which justifies the choice of a heterogeneous distribution of the criticality field $C(z)$.

Last, we do not account for subsurface structures which may lead to local stress accumulations and increased pressure perturbations⁴⁶. Moreover, large fault zones act as fluid flow channels, causing a rapid response of deeper basement intervals.

Nevertheless, we successfully applied the new model of URIS to the case of earthquakes observed in Central Oklahoma. Thus, it provides an important step towards future research on the characterisation and analysis of seismicity induced by high-volume fluid injections.

Methods

Data. We use locations and occurrence times of seismic events from a catalogue published by Schoenball and Ellsworth²⁹. Given depths are referred to the ground surface. To analyse only the spatio-temporal distribution of main shocks, we declustered the catalogue (see the Supplementary Materials).

The top of the basement (TOB) was constrained by well data, obtained from Campbell and Weber³¹. We plot here the surface of the basement top relative to the ground surface elevation. Based on this data, we set the mean depth of the TOB z_0 to 3 km for our calculations.

Injection rates for the study area were taken from Langenbruch and Zoback³.

Analytic Solution. For the derivation of the analytical solution, we assume that a medium with porosity Φ_{Ar} overlays a fluid-saturated, poroelastic half-space which extends in the vertical z -direction below the depth z_0 . In such a case, the application of a surface load on the poroelastic half-space can be described by a 1D problem and quantities are functions of z only. The stress-strain relation:

$$\sigma_{ij} + \alpha p \delta_{ij} = 2G \varepsilon_{ij} + \frac{2G\nu}{1 - 2\nu} \varepsilon \delta_{ij} \quad (2)$$

for such an uniaxial-strain problem is given by^{19,26,47}:

$$\sigma_{zz} = (\lambda_{dr} + 2G_{dr}) \varepsilon_{zz} - \alpha p \quad (3)$$

$$\sigma_{xx} = \sigma_{yy} = \lambda_{dr} \varepsilon_{zz} - \alpha p. \quad (4)$$

In the above equations, σ and ε are the stress and strain, respectively. p denotes the pore-fluid pressure and α is the so-called Biot's coefficient. Furthermore, λ_{dr} and G_{dr} are the drained Lamé parameters. Equations 3–4 are valid under the assumption of pore space being filled with a fluid with pressure p . Then, the pore-fluid pressure relation:

$$p = M(\zeta - \alpha \varepsilon_{kk}) \quad (5)$$

for the uniaxial strain case can be written as (equation (2.176) in Shapiro²⁶):

$$p = M(\zeta - \alpha \varepsilon_{zz}). \quad (6)$$

Here, ζ is the relative modification of pore-space volume due to fluid mass changes and M is the Biot's modulus $M = \left[\frac{\Phi}{K_f} + \frac{\alpha - \Phi}{K_{dr}} \right]^{-1}$, with the porosity Φ , the Biot's coefficient α and the bulk moduli of the drained matrix K_{dr} and the pore fluid K_f .

The equilibrium equation for poroelastic stresses, assuming that gravity acts in the vertical z -direction, is given by:

$$\frac{\partial}{\partial z} \sigma_{zz} = -\rho g, \quad (7)$$

with the bulk density $\rho = \rho_{dr} + \Phi \rho_f$ where ρ_f and ρ_{dr} denote the fluid density and the drained matrix density of a medium with porosity Φ , respectively. Following the concept of loading modes introduced by Detournay and Cheng¹⁹, field quantities can be obtained. All of the above hydraulic and elastic parameters are values for the underlying formation (the crystalline basement in Central Oklahoma).

Loading mode I corresponds to Terzaghi's 1D consolidation. In this mode, a normal confining stress of magnitude $\Phi_{Ar}p_0$ acts at the top boundary of the poroelastic half-space at depth z_0 and pore-fluid pressure perturbation on the surface z_0 is absent. We introduced the porosity of the target injection formation Φ_{Ar} , in our case the Arbuckle formation. Note that this is a modification of the 1D solution as described by Shapiro²⁶ and an important feature of the URIS model. The boundary condition for the stress at z_0 is then given by $\sigma_{zz}^I(z_0, t) = -H_s - h(t)\Phi_{Ar}p_0$, $h(t)$ indicates the step-like increase of stress at time $t=0$ and H_s is a constant corresponding to the load caused by the overburden. Using the equilibrium equation (7), the total stress is a function of the depth and given by:

$$\sigma_{zz}^I(z, t) = -H_s - \rho g(z - z_0) - h(t)p_0\Phi_{Ar}. \tag{8}$$

Immediately after the load is applied, the system is in an undrained state and fluid flow is vanishing. From equation (2.179) of²⁶ it follows:

$$p(z, t) = p_0 \operatorname{erfc}\left(\frac{z}{\sqrt{4Dt}}\right). \tag{9}$$

Using this relation, the pore-fluid pressure in loading mode I can be calculated by:

$$p^I(z, t) = \rho_f g(z - z_0) + \Phi_{Ar} \frac{n_s}{G_{dr}S} \left[p_0 h(t) - p_0 \operatorname{erfc}\left(\frac{z - z_0}{\sqrt{4Dt}}\right) \right], \tag{10}$$

(see also equation (2.184) of²⁶). S and D are the uniaxial storage coefficient and the hydraulic diffusivity, respectively, and n_s is the poroelastic stress coefficient $n_s \equiv \alpha(1 - 2\nu_{dr})/2(1 - \nu_{dr})$ with the drained Poisson's ratio ν_{dr} .

In loading mode II, a pore-fluid pressure $p^{II}(z_0, t) = H_f + p_0 h(t)$ is applied at z_0 and normal stresses are vanishing. In analogy to the constant load induced by the overburden H_s , H_f is a constant corresponding to the load caused by the fluid in the pore space of the overburden. In our scenario, H_f is given by the *in-situ* pore-fluid pressure $H_f = \rho_f g z_0$. Thus, it follows:

$$p^{II}(z, t) = H_f + p_0 \operatorname{erfc}\left(\frac{z - z_0}{\sqrt{4Dt}}\right). \tag{11}$$

The complete solution to this boundary problem is then obtained by a summation of the pressure and stress solutions for modes I and II:

$$p(z, t) = H_f + \rho_f g(z - z_0) + p_0 h(t) \left[\Phi_{Ar} \frac{n_s}{G_{dr}S} + \operatorname{erfc}\left(\frac{z - z_0}{\sqrt{4Dt}}\right) \right] \left[1 - \Phi_{Ar} \frac{n_s}{G_{dr}S} \right], \tag{12}$$

$$\sigma_{zz}(z, t) = -H_s - \rho g(z - z_0) - h(t)p_0\Phi_{Ar}. \tag{13}$$

Further it follows for the vertical strain $\varepsilon_{zz}(z, t)$ and horizontal stress $\sigma_{xx}(z, t)$:

$$\varepsilon_{zz}(z, t) = \frac{\sigma_{zz}(z, t) + \alpha p(z, t)}{\lambda_{dr} + 2G_{dr}}, \tag{14}$$

$$\sigma_{xx}(z, t) = \sigma_{yy}(z, t) = \lambda_{dr} \varepsilon_{zz}(z, t) - \alpha p(z, t). \tag{15}$$

The multiplication with $h(t)$ yields a step-like increase of p_0 at time $t=0$ to a constant value p_0 . Later we also show results for a time-dependent boundary condition where $p_0 = p_0(t)$. Note that a multiplication of $p_0 \operatorname{erfc}\left(\frac{z - z_0}{\sqrt{4Dt}}\right)$ with $h(t)$ does not change the solution (see also equation (2.186) in²⁶).

For pressure and stress calculations, we use $z = [0, 10 \text{ km}]$ with a spacing of 1 m.

Numerical Model. The COMSOL Multiphysics software applied for the solution of the numerical model is a finite element software. For our purposes we use version 5.2a and the built-in Poroelasticity interface, which couples the Fluid Flow and Solid Mechanics physics (see Supplementary Materials).

Prior to further analyses, the numerical pressure and stress values obtained for the model geometry of 1 m length and total depth of 30 km were interpolated on a regular two-dimensional grid with a spacing of 0.1 m in x -direction and 1 m in z -direction. Subsequently, we extracted values which lie on a line which extends in z -direction between $[z_0, 10 \text{ km}]$ at $x = 0.5 \text{ m}$.

Synthetic Seismicity. The log-normal distribution is given by the probability density function $y = f(x|\mu, \sigma) = \frac{1}{x\sigma\sqrt{2\pi}} e^{-\frac{(\ln x - \mu)^2}{2\sigma^2}}$, where $\mu = \ln(m^2/\sqrt{v + m^2})$ and $\sigma = \sqrt{\ln(v/m^2 + 1)}$ are parameters of the distribution with the mean m and the variance v . We find that the spatio-temporal distribution of synthetic events and observed seismicity at different depth intervals is most consistent for a criticality field statistically defined by a log-normal distribution with $m = 0.15 \text{ MPa}$ and $v = 10 \text{ GPa}^2$. Additionally, zones in the upper basement (above 2 km) and lower basement (below 2 km) are characterised by uniformly distributed values between $[0.1 \text{ MPa}, 0.3 \text{ MPa}]$ and $[0.01 \text{ MPa}, 0.4 \text{ MPa}]$, respectively. The locations z of $\tilde{C}(z)$ are given by the same spatial grid as used for the analytical solution, i.e. N points along a line which extends in z -direction between $z_0 = 3 \text{ km}$ and 10 km with a grid spacing of 1 m.

Data Availability. The synthetic datasets generated and analysed during the current study are available from the corresponding author on reasonable request. Well data used to constrain the basement depth are available from, <http://ogs.ou.edu/docs/specialpublications/SP2006-1T1.xls>. The catalogue of relocated events used in this work can be obtained from²⁹, Supplementary Material.

References

- Ellsworth, W. L. Injection-Induced Earthquakes. *Science* **341**, <https://doi.org/10.1126/science.1225942> (2013).
- Walsh, F. R. & Zoback, M. D. Oklahoma's recent earthquakes and saltwater disposal. *Sci. Adv.* **1**, <https://doi.org/10.1126/sciadv.1500195> (2015).
- Langenbruch, C. & Zoback, M. D. How will induced seismicity in Oklahoma respond to decreased saltwater injection rates? *Sci. Adv.* **2**, <https://doi.org/10.1126/sciadv.1601542> (2016).
- Hincks, T., Aspinall, W., Cooke, R. & Gernon, T. Oklahoma's induced seismicity strongly linked to wastewater injection depth. *Science* **359**, 1251–1255, <https://doi.org/10.1126/science.aap7911> (2018).
- Raleigh, C. B., Hale, J. H. & Bredehoeft, J. D. An Experiment in Earthquake Control at Rangely, Colorado. *Science* **191**, 1230–1237, <https://doi.org/10.1126/science.191.4233.1230> (1976).
- Zoback, M. & Harjes, H. P. Injection-induced earthquakes and crustal stress at 9 km depth at the KTB deep drilling site, Germany. *J. Geophys. Res.* **102**, 18477–18491, <https://doi.org/10.1029/96JB02814> (1997).
- Shapiro, S. A., Huenges, E. & Borm, G. Estimating the permeability from fluid-injection induced seismic emission at the KTB site. *Geophys. J. Int.* **131**, F15–F18, <https://doi.org/10.1111/j.1365-246X.1997.tb01215.x> (1997).
- Goebel, T. H. W., Weingarten, M., Chen, X., Haffner, J. & Brodsky, E. E. The 2016 Mw5.1 Fairview, Oklahoma earthquakes: Evidence for long-range poroelastic triggering at >40 km from fluid disposal wells. *Earth Planet. Sci. Lett.* **472**, 50–61, <https://doi.org/10.1016/j.epsl.2017.05.011> (2017).
- Segall, P. & Lu, S. Injection-induced seismicity: Poroelastic and earthquake nucleation effects. *Journal of Geophysical Research: Solid Earth* **120**, 5082–5103, <https://doi.org/10.1002/2015JB012060> (2015).
- Norbeck, J. H. & Horne, R. N. Evidence for a transient hydromechanical and frictional faulting response during the 2011 Mw 5.6 Prague, Oklahoma earthquake sequence. *Journal of Geophysical Research: Solid Earth* **121**, 8688–8705, <https://doi.org/10.1002/2016JB013148> (2016).
- Barbour, A. J., Norbeck, J. H. & Rubinstein, J. L. The Effects of Varying Injection Rates in Osage County, Oklahoma, on the 2016 Mw 5.8 Pawnee Earthquake. *Seismol. Res. Lett.* **88**, 1040, <https://doi.org/10.1785/0220170003> (2017).
- Simpson, D. W. Seismicity changes associated with reservoir loading. *Eng. Geol.* **10**, 123–150, [https://doi.org/10.1016/0013-7952\(76\)90016-8](https://doi.org/10.1016/0013-7952(76)90016-8) (1976).
- Simpson, D. W., Leith, W. S. & Scholz, C. H. Two types of reservoir-induced seismicity. *Bull. Seismol. Soc. Am.* **78**, 2025–2040 (1988).
- Talwani, P. On the Nature of Reservoir-induced Seismicity. *Pure Appl. Geophys.* **150**, 473–492, https://doi.org/10.1007/978-3-0348-8814-1_8 (1997).
- Rice, J. & Cleary, M. Some basic stress diffusion solutions for fluid-saturated elastic porous media with compressible constituents. *Rev. Geophys.* **14**, 227–241, <https://doi.org/10.1029/RG014i002p00227> (1976).
- Rudnicki, J. W. Fluid Mass Sources and Point Forces in Linear Elastic Diffusive Solids. *Mechanics of Materials* **5**, 383–393 (1986).
- Norbeck, E. Fault stability changes induced beneath a reservoir with cyclic variations in water level. *Journal of Geophysical Research: Solid Earth* **93**, 2107–2124, <https://doi.org/10.1029/JB093iB03p02107> (1988).
- Gupta, H. *Reservoir Induced Earthquakes*, vol. 64 (Elsevier Science, 1992).
- Detournay, E. & Cheng, A. *Fundamentals of Poroelasticity*, vol. 2 (Pergamon Press, 1993).
- Talwani, P. Speculation on the causes of continuing seismicity near Koyna reservoir, India. *Pure Appl. Geophys.* **145**, 167–174, <https://doi.org/10.1007/BF00879492> (1995).
- Wang, H. F. *Theory of Linear Poroelasticity with Applications to Geomechanics and Hydrogeology* (Princeton University Press, 2000).
- Chen, L. & Talwani, P. Mechanism of Initial Seismicity Following Impoundment of the Monticello Reservoir, South Carolina. *Bull. Seismol. Soc. Am.* **91**, 1582–1594 (2001).
- Cocco, M. & Rice, J. R. Pore pressure and poroelasticity effects in Coulomb stress analysis of earthquake interactions. *Journal of Geophysical Research: Solid Earth* **107**, ESE 2–1–ESE 2–17, <https://doi.org/10.1029/2000JB000138>.
- Gupta, H. K. A review of recent studies of triggered earthquakes by artificial water reservoirs with special emphasis on earthquakes in Koyna, India. *Earth Sci. Rev.* **58**, 279–310, [https://doi.org/10.1016/S0012-8252\(02\)00063-6](https://doi.org/10.1016/S0012-8252(02)00063-6) (2002).
- Gavrilenko, P., Singh, C. & Chadha, R. K. Modelling the hydromechanical response in the vicinity of the Koyna reservoir (India): results for the initial filling period. *Geophys. J. Int.* **183**, 461–477, <https://doi.org/10.1111/j.1365-246X.2010.04752.x> (2010).
- Shapiro, S. *Fluid-Induced Seismicity* (Cambridge University Press, Cambridge, U.K., 2015).
- Alt, R. C. & Zoback, M. D. *In Situ Stress and Active Faulting in Oklahoma* In Situ Stress and Active Faulting in Oklahoma. *Bull. Seismol. Soc. Am.* **107**, 216, <https://doi.org/10.1785/0120160156> (2016).
- Petersen, M. *et al.* 2017 One-Year Seismic-Hazard Forecast for the Central and Eastern United States from Induced and Natural Earthquakes. *Seismol. Res. Lett.* **88**, 772–783, <https://doi.org/10.1785/0220170005> (2017).
- Schoenball, M. & Ellsworth, W. Waveform-Relocated Earthquake Catalog for Oklahoma and Southern Kansas Illuminates the Regional Fault Network. *Seismol. Res. Lett.* **88**, <https://doi.org/10.1785/0220170083> (2017).
- Schoenball, M. & Ellsworth, W. L. A Systematic Assessment of the Spatiotemporal Evolution of Fault Activation Through Induced Seismicity in Oklahoma and Southern Kansas. *Journal of Geophysical Research: Solid Earth* **122**, 10189–10206, <https://doi.org/10.1002/2017JB014850> (2017).
- Campbell, J. A. & Weber, J. L. Wells drilled to Basement in Oklahoma. *Oklahoma Geological Survey Special Publication* **1** (2006).
- Carder, D. Seismic investigations in the Boulder Dam area, 1940–1944, and the influence of reservoir loading on local earthquake activity. *Bull. Seismol. Soc. Am.* **35**, 175–192 (1945).
- Biot, M. General theory of three-dimensional consolidation. *J. Appl. Phys.* **12**, 155–164 (1941).
- McGarr, A., Simpson, D. & Seeber, L. Case Histories of Induced and Triggered Seismicity. In Lee, W. H., Kanamori, H., Jennings, P. C. & Kisslinger, C. (eds.) *International Handbook of Earthquake and Engineering Seismology, Part A*, vol. 81 of *International Geophysics*, 647–661, [https://doi.org/10.1016/S0074-6142\(02\)80243-1](https://doi.org/10.1016/S0074-6142(02)80243-1) (Academic Press, 2002).
- Chung, W.-Y. & Liu, C. The reservoir-associated earthquakes of April 1983 in western Thailand: Source modeling and implications for induced seismicity. *Pure Appl. Geophys.* **138**, 17–41, <https://doi.org/10.1007/BF00876712> (1992).
- Chandra, U. Focal Mechanism of the Koyna, India Earthquake of 1967, December 10. *Geophys. J. R. Astron. Soc.* **46**, 247–251, <https://doi.org/10.1111/j.1365-246X.1976.tb04156.x> (1976).
- Awad, M. & Mizoue, M. Earthquake activity in the Aswan region, Egypt. *Pure Appl. Geophys.* **145**, 69–86, <https://doi.org/10.1007/BF00879484> (1995).
- Mahdi, S. K. Tarbela Reservoir A Question of Induced Seismicity. In *International Conference on Case Histories in Geotechnical Engineering*, vol. 48 (1988).
- Nelson, P. H., Gianoutsos, N. J. & Drake, D. M. Underpressure in Mesozoic and Paleozoic rock units in the Midcontinent of the United States. *AAPG Bulletin* **99**, 1861–1892, <https://doi.org/10.1306/04171514169> (2015).

40. Pei, S., Peng, Z. & Chen, X. Locations of Injection-Induced Earthquakes in Oklahoma Controlled by Crustal Structures. *Journal of Geophysical Research: Solid Earth* **0**, <https://doi.org/10.1002/2017JB014983> (2018).
41. Chang, K. W. & Segall, P. Injection-induced seismicity on basement faults including poroelastic stressing. *Journal of Geophysical Research: Solid Earth* **121**, 2708–2726, <https://doi.org/10.1002/2015JB012561> (2016).
42. Saltelli, A. et al. *Global Sensitivity Analysis: The Primer* (Wiley, 2008).
43. Rothert, E. & Shapiro, S. A. Statistics of fracture strength and fluid-induced microseismicity. *Journal of Geophysical Research: Solid Earth* **112**, <https://doi.org/10.1029/2005JB003959> (2007).
44. Rothert, E. & Shapiro, S. A. Microseismic monitoring of borehole fluid injections: Data modeling and inversion for hydraulic properties of rocks. *Geophysics* **68**, 685–689, <https://doi.org/10.1190/1.1567239> (2003).
45. Langenbruch, C. & Zoback, M. D. Response to Comment on “How will induced seismicity in Oklahoma respond to decreased saltwater injection rates?”. *Sci. Adv.* **3**, <https://doi.org/10.1126/sciadv.aao2277> (2017).
46. Simpson, D. W. & Narasimhan, N. T. Inhomogeneities in rock properties and their influence on reservoir induced seismicity. *Gerlands Beitr. Geophysik Leipzig* **99** (1990).
47. Jaeger, J. C., Cook, N. G. W. & Zimmermann, R. *Fundamentals of Rock Mechanics* (Wiley-Blackwell, 2007).

Acknowledgements

We thank the PHASE consortium research project which provided the financial support for this study. Furthermore, this work would not have been possible without the catalogue of relocated earthquakes published by Schoenball and Ellsworth²⁹ and injection rates revised by Langenbruch and Zoback³. The authors gratefully thank two anonymous reviewers for their thorough comments which helped to substantially improve the work.

Author Contributions

L.J. carried out the main analyses presented in this study. The concept of the study was developed by S.A.S., who also provided useful supervision and guidance of the work. C.D. additionally supported the research. All authors reviewed the manuscript.

Additional Information

Supplementary information accompanies this paper at <https://doi.org/10.1038/s41598-018-29883-9>.

Competing Interests: The authors declare no competing interests.

Publisher's note: Springer Nature remains neutral with regard to jurisdictional claims in published maps and institutional affiliations.



Open Access This article is licensed under a Creative Commons Attribution 4.0 International License, which permits use, sharing, adaptation, distribution and reproduction in any medium or format, as long as you give appropriate credit to the original author(s) and the source, provide a link to the Creative Commons license, and indicate if changes were made. The images or other third party material in this article are included in the article's Creative Commons license, unless indicated otherwise in a credit line to the material. If material is not included in the article's Creative Commons license and your intended use is not permitted by statutory regulation or exceeds the permitted use, you will need to obtain permission directly from the copyright holder. To view a copy of this license, visit <http://creativecommons.org/licenses/by/4.0/>.

© The Author(s) 2018

The surge of earthquakes in Central Oklahoma has features of reservoir-induced seismicity

Lisa Johann^{1,*}, Serge A. Shapiro¹, and Carsten Dinske¹

¹Freie Universitaet Berlin, Institute of Geophysics, Berlin, 12249, Germany

*lisa.johann@geophysik.fu-berlin.de

+these authors contributed equally to this work

ABSTRACT

This file contains supplementary material for the main article, necessary to comprehend the background of the study and the methods we applied.

Supplementary Material includes

- Supplementary Text
- Fig. S1 – S10
- Table S1
- References

Supplementary Text

S1. Declustering

We use locations and occurrence times of seismic events from a catalogue published by Schoenball and Ellsworth¹.

As demonstrated in previous works, naturally occurring earthquakes are distributed according to a non-homogeneous Poisson process (NHPP) in time, reflecting the existence of fore- and aftershock sequences². In contrast, a sequence of independently occurring events can be statistically described by a homogeneous Poisson process (HPP).

Recently published works revealed that seismicity in Oklahoma shows significant aftershock activity³. Thus, for the work presented here, we removed these dependent events from the original earthquake catalogue¹, neglecting events with a depth error $\delta z > 0.5$ km (Fig. S1). We applied a declustering method by Urhammer⁴ which is based on a moving time and space window. From 7835 events located in our area of interest, 2473 events had a vertical error $\zeta < 0.5$ km. Among these high-precision events, 1263 main shocks were identified by the algorithm (Fig. S2).

As shown in Figure S3, A - B, the main shocks (red line) now follow the expected homogeneous Poisson distribution (HPP), demonstrated by a simulated event distribution (black dashed line). To describe the magnitude-frequency distribution, the Gutenberg-Richter relation⁵ given by $\log_{10} N = a - bM$ is used. Here, N is the number of events with magnitude $\geq M$ and a and b are constants. For the declustered event catalogue, $b = 1.11$ (Fig. S3C). The obtained magnitude of completeness is $M_c = 2.4$.

As can be seen in Fig. S10A, the mean depth of the main shocks with $M > M_c$ increases with time.

S2. Numerics

The COMSOL Multiphysics software applied for the solution of the numerical model is a finite element software. For our purposes we use version 5.2a and the built-in Poroelasticity interface, which couples the Fluid Flow and Solid Mechanics physics

Equations The numerical solutions are based on the quasi-static approximation of poroelasticity. This

approximation is given by the continuity equation:

$$\frac{\partial \Phi}{\partial t} + \nabla \mathbf{u} = 0, \quad (\text{S1})$$

defining the conservation of fluid mass, Darcy's law:

$$\mathbf{u} = -\frac{\kappa}{\eta} \nabla p, \quad (\text{S2})$$

and the equilibrium equation for poroelastic stresses:

$$\nabla \sigma = 0. \quad (\text{S3})$$

Here, κ denotes the permeability and η is the dynamic viscosity of the pore fluid. Equations S1 - S2 are valid for a hydraulically and elastically isotropic, homogeneous medium.

Using the two constitutive equations (1) and (4) with equations S1 - S2, solutions for pore-fluid pressure and stresses can be found. There exist several equivalent forms of pressure and stress equations in literature (see e.g. chapter 2.5 in⁶). Assuming a hydraulically and elastically isotropic, homogeneous medium, pore-fluid pressure can be obtained by the solution of a diffusion equation coupled to isotropic stress terms using the quantity M , the permeability κ and the fluid viscosity η :

$$\frac{1}{M} \frac{\partial p}{\partial t} - \frac{\kappa}{\eta} \nabla^2 p = -\alpha \frac{\partial \varepsilon_{kk}}{\partial t}. \quad (\text{S4})$$

In this equation, the right-hand term can be interpreted as the rate of change of pore space. As increasing $\partial \varepsilon_{kk} / \partial t$ gives rise to a larger volume available for fluid storage, it indicates a fluid sink marked by the negative sign.

Stresses are obtained from the equilibrium equation S3, assuming that the solid is under purely gravitational load:

$$\nabla \sigma = -(\rho_f \Phi + \rho_{dr}) \mathbf{g}. \quad (\text{S5})$$

Even though equation S5 is a stationary expression, it is applicable for time-dependent flow models as in our case. This is because the elastic response of the undrained medium is generally much faster than the fluid flow. Thus, in response to changing flow conditions, a new stress equilibrium is reached immediately and stresses and strains become functions of time. Such an assumption is considered as the quasi-static approximation of poroelasticity.

Geometry

We build our approximate model using a 2D plane strain geometry, assuming that the horizontal length in y -direction is much larger than the other two directions x and z . Thus, perturbations of the normal strain $\Delta\varepsilon_{yy}$ as well as of the shear strains $\Delta\varepsilon_{xy}$ and $\Delta\varepsilon_{zy}$ are zero and the stress perturbations in the horizontal plane are equal: $\Delta\sigma_{yy} = \Delta\sigma_{xx}$.

We define a rectangular geometry with length $x = 1$ m and total depth $z = 30$ km (Fig. S4), representing the subsurface of Oklahoma. The small extension in x -direction is justified by the aim of modelling effectively a 1D problem. We tested the influence of the vertical boundaries to exclude the possibility of distorted results. An additional boundary is inserted at $z = z_0 = 3$ km (Fig. S4.2b, bold line at 3 km). It defines the boundary between the Arbuckle formation and the basement and thus, also the bottom of the reservoir coinciding with the TOB. For the following we assume that the Cartesian coordinate system is oriented such that principal axes align with the x - and z -directions.

Parameter, Boundary and Initial Conditions

For the assessment of seismicity induced in Central Oklahoma, numerical and analytical models are based on hydraulic and elastic parameter from literature, listed in table 1. Note that all parameters are defined for the crystalline basement in Oklahoma except for the porosity of the injection formation Φ_{Ar} . Regarding the Biot's coefficient α , we use a value of 0.3. This is only an estimate as elastic parameters strongly depend on the stress conditions under which they are measured. Also larger values have been reported for granite in literature (see e.g.⁷). The larger α , the stronger the poroelastic coupling. Thus, the comparatively low value can be understood to represent one end member of rather weak poroelastic coupling.

As we consider a poroelastic finite element model, appropriate hydro-mechanical boundary (BC) and initial conditions (IC) have to be set. Regarding mechanical BC, the top of the block defines the

earth's surface and is set to free. The other three boundaries are defined by a so-called roller condition, i.e. no lateral movement. Corresponding hydrological BC are given by no flow at the side and bottom boundary. Regarding the top boundary corresponding to the surface, the pressure is set to $p = 0$ Pa. The TOB-boundary at depth z_0 becomes active for times $t \geq 0$. At this boundary, the pressure is given by the pressure at the bottom of the reservoir due to the overlying water column $p(z_0, t) = p_0$ and by the vertical stress $\sigma_{zz}(z_0, t) = -p_0 \Phi_{Ar}$.

Concerning IC, we include gravity driven stress- and pressure gradients. For this, two stationary model runs are necessary prior to the transient analysis including the TOB-boundary. In step one, initial displacement u and pressure p are set to zero and the solver calculates ambient stress and pressure values due to gravity driven loading (Fig. S4.1). Step two, referring again to a stationary solver, is needed for the model calibration as well as for software intern definition issues. A second poroelasticity physics module is added and pressure and stress solutions derived in step one are defined as IC (Fig. S4.2a). The third step solves the transient poroelastic equations for times $t = [0, t_{max}]$ with $\Delta t = 1$ month. For this, pressure and stress solutions obtained in step two are defined as initial values. Note that the additional boundary defining the bottom of the reservoir only becomes active in this study step (Fig. S4.2b).

Data Analysis

Prior to further analyses, the numerical pressure and stress values obtained for the model geometry of 1 m length and total depth of 30 km were interpolated on a regular two-dimensional grid with a spacing of 0.1 m in x -direction and 1 m in z -direction. Subsequently, we extracted values which lie on a line which extends in z -direction between $[z_0, 10 \text{ km}]$ at $x = 0.5$ m.

S3. The Influence of the Tectonic Setting

As shown above and in earlier studies on RIS^{6,8}, the tectonic setting significantly influences the occurrence of reservoir induced seismic activity. These works demonstrated that RIS is most likely under normal faulting and strike-slip stress orientations. Therefore, the ambient state of stress should be considered also in the case of URIS.

To validate this assumption, we use the analytically derived pressure and stress solutions and calculate values of ΔFCS for three arbitrary stress regimes. The initial values are set such that the differential stress

is equal for all cases and that magnitudes are larger than the calculated perturbations. Further, the type of the background state of stress (faulting regime) remains unaffected by the fluid injection. Note that the numerical models were obtained for plane strain solutions, i.e. stresses changes in the horizontal plane are equal ($\Delta\sigma_x = \Delta\sigma_H = \Delta\sigma_y = \Delta\sigma_h$). Under this limitation, total vertical, maximum horizontal and minimum horizontal stresses are given by

$$\sigma_v = \sigma_{v,ini} + \Delta\sigma_z, \quad (S6)$$

$$\sigma_H = \sigma_{H,ini} + \Delta\sigma_x, \quad (S7)$$

$$\sigma_h = \sigma_{h,ini} + \Delta\sigma_x, \quad (S8)$$

respectively.

Since a pre-existing, optimally oriented fracture is stable as long as ΔFCS is negative but is moved closer to failure if ΔFCS turns positive, the time and location of destabilisation can be determined. We call the location $z(t)$ for which $\Delta FCS = 0$ the *destabilisation front*. Earlier works on induced seismicity use so-called $r - t$ -plots for the analysis of spatio-temporal features of the seismic cloud^{9,10}. In the 1D case considered here, r corresponds to the event depth. Plotting the evolution of the destabilisation front in an $r - t$ -plot, this front envelops the domain that has been brought closer to failure ($\Delta FCS > 0$) due to pressure and stress perturbations.

Figure 3 shows the obtained values of ΔFCS for the different regimes as profiles along the depth for different time steps as well as the corresponding destabilisation front. The components of ΔFCS are depicted in Figure S5. Of course, the individual magnitudes must be considered carefully as they strongly depend on the initial conditions as well as on used model parameters.

Normal Faulting

Let us consider a normal faulting regime with

$$\sigma_{1,ini} = \sigma_{v,ini}$$

$$\sigma_{2,ini} = \sigma_{H,ini} = 0.9\sigma_{v,ini}$$

$$\sigma_{3,ini} = \sigma_{h,ini} = 0.75\sigma_{v,ini}$$

Under the assumption that initial stress magnitudes are larger than the calculated perturbations it follows for the principal stresses with equations S6 - S8: $\sigma_1 = \sigma_{v,ini} + \Delta\sigma_z$, $\sigma_2 = \sigma_{H,ini} + \Delta\sigma_x$, $\sigma_3 = \sigma_{h,ini} + \Delta\sigma_x$. From this it follows that $\Delta\sigma_m = 0.5(\Delta\sigma_z + \Delta\sigma_x)$ and $\Delta\sigma_d = \Delta\sigma_z - \Delta\sigma_x$.

As shown in Figure S5A, the contribution of $-\sin(\varphi)\Delta\sigma_m$ is negative throughout the medium and the model time, indicating positive values of $\Delta\sigma_m$ which leads to a stabilisation of the medium. However, $0.5\Delta\sigma_d$ is smaller than $\sin(\varphi)(\Delta\sigma_m - \Delta p)$ such that ΔFCS is positive at each location and time step (Fig. 3A). This behaviour is also revealed by the domain of destabilisation, which evolves immediately even at the deepest point of our model (Fig. 3B).

Strike-Slip

Now, let us take a strike-slip regime with

$$\sigma_{1,ini} = \sigma_{H,ini} = 1.05\sigma_{v,ini}$$

$$\sigma_{2,ini} = \sigma_{v,ini}$$

$$\sigma_{3,ini} = \sigma_{h,ini} = 0.8\sigma_{v,ini}$$

Following the total stress convention, equations S6 - S8, total principal stresses are given by $\sigma_1 = \sigma_H = \sigma_{H,ini} + \Delta\sigma_x$, $\sigma_2 = \sigma_v = \sigma_{v,ini} + \Delta\sigma_z$, $\sigma_3 = \sigma_h = \sigma_{h,ini} + \Delta\sigma_x$. Thus, $\Delta\sigma_m = \Delta\sigma_x$ and $\Delta\sigma_d = 0$.

In the strike-slip regime (Fig. S5B), pressure perturbations are larger than absolute changes of the mean stress if the pressure diffusion reaches a significant level at the considered location. The change of the differential stress is zero throughout the medium for all time steps, caused by the condition of plane strain with $\Delta\sigma_H = \Delta\sigma_h$. Therefore, ΔFCS is negative as long as $(\Delta\sigma_m - \Delta p) < 0$. As soon as $|\Delta p| > |\Delta\sigma_m|$, ΔFCS turns positive (Fig. 3C). The destabilisation front concept further supports this observation, yielding a front which evolves rapidly with time from the TOB to deeper intervals (Fig. 3D).

Thrust Faulting

Last, we assume a thrust faulting regime with

$$\sigma_{1,ini} = \sigma_{H,ini} = 1.25\sigma_{v,ini}$$

$$\sigma_{2,ini} = \sigma_{h,ini} = 1.05\sigma_{v,ini}$$

$$\sigma_{3,ini} = \sigma_{v,ini}$$

Total principal stresses are given by $\sigma_1 = \sigma_H = \sigma_{H,ini} + \Delta\sigma_x$, $\sigma_2 = \sigma_v = \sigma_{v,ini} + \Delta\sigma_z$, $\sigma_3 = \sigma_h = \sigma_{h,ini} + \Delta\sigma_x$, using the total stress convention, equations S6 - S8. From this it follows that $\Delta\sigma_d = \Delta\sigma_x - \Delta\sigma_z$, i.e. $\Delta\sigma_d < 0$, and $\Delta\sigma_m = \Delta\sigma_x + \Delta\sigma_z$. Generally, decreasing differential stress means a stabilisation of the medium as long as the decline is not compensated by decreasing effective normal stresses.

From this it follows for the thrust faulting setting (Fig. S5C) that the medium destabilises ($\Delta FCS > 0$) if $|0.5\Delta\sigma_d| > |\sin(\varphi)(\Delta\sigma_m - \Delta p)|$ (Fig. 3E). In the scenario of URIS discussed here, the destabilisation is time-dependent, demonstrated also by the destabilisation front (Fig. 3F).

S4. Sensitivity Study

To test the influence of parameters on ΔFCS , we performed a local, one-at-a-time (OAT) sensitivity study. While changing one parameter incrementally, the other parameters are held constant at their base level value. The great advantage of the method is that the influence of each parameter on the output can be determined directly.

For five hydraulic and elastic parameters we increased the parameter value by +10% within the interval [-50%, 50%]. To allow for stronger variations of the hydraulic diffusivity¹¹, the value for D was varied on a logarithmic scale between 1e-03 and 1e+03.

The influence on ΔFCS is also expressed in terms of the destabilisation front (Supplementary Fig. S6). Destabilisation fronts obtained for the base level parameter values are marked by the bold black line. Blue to red lines mark the front for parameter variations between -50% and +50%. As was to be expected, the higher the value of ΔFCS at depth, the further the destabilization front perturbs the medium. As most of the parameters are proportional to ΔFCS (Fig. 4), the fronts evolve faster with increasing variations (Fig. S6, panels A, B, C, E, F). However, as it is inversely proportional to the basement porosity, the destabilised

domain reduces within the model time for higher Φ (Fig. S6D).

To complement the study, we tested the influence of the injection pressure p_0 under various stress regimes. Changing the positive value of p_0 (injection) to negative (discharge), the medium is stabilised in a strike-slip setting (Figs. S7A and S8), red line. Under thrusting conditions (Fig. S8, green line) stabilisation occurs only in vicinity to the injector (e.g. Fig. S8, A and E). At greater depths (Fig. S8, C - D), the medium is destabilised. However, this observation changes with time (Fig. S8, G - H), as soon as the local pore-fluid pressure increases due to diffusion (compare also to Figure S7).

Supplementary Table

Table 1. Hydro-mechanical parameter

Parameter	Value
D	0.05 (m ² /s)
Φ	1 (%)
Φ_{Ar}	20 (%)
ρ_f	940.3 (kg/m ³)*
η	2e-04 (Pas)*
K_f	2 (GPa)*
ρ_{dr}	2740 (kg/m ³) [†]
G_{dr}	25 (GPa) [†]
λ_{dr}	20 (GPa)
α	0.3
μ_f	0.7

*12, †13

Supplementary Figures

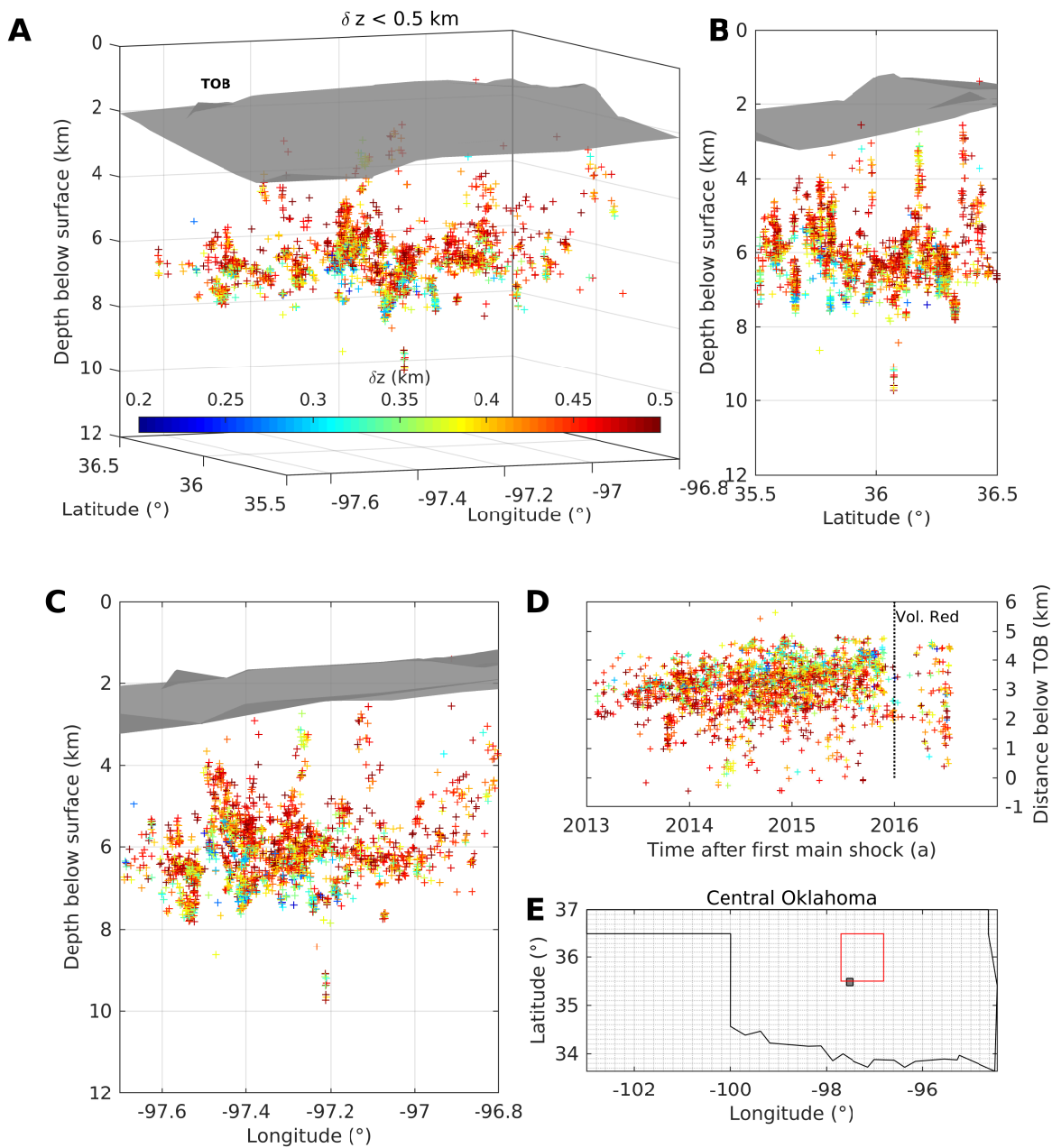


Figure S1. Seismicity in Central Oklahoma from May 2013 to November 2016. The map (E) demonstrates the area of interest in Central Oklahoma, bounded by latitude 35.5° to 36.5° and longitude -97.7° to -96.8°. Panels (A) - (D) show event depths and the top of the basement (TOB) relative to the ground surface elevation. In panel (D), event distances below the TOB are plotted versus their occurrence time. Year 0 denotes the time of the first event included in the catalogue on May 5, 2013. Event locations were published by Schoenball and Ellsworth¹, showing only events with depth errors $\delta z < 0.5$ km as used for the declustering. The depth of the TOB was derived from well data¹⁴.

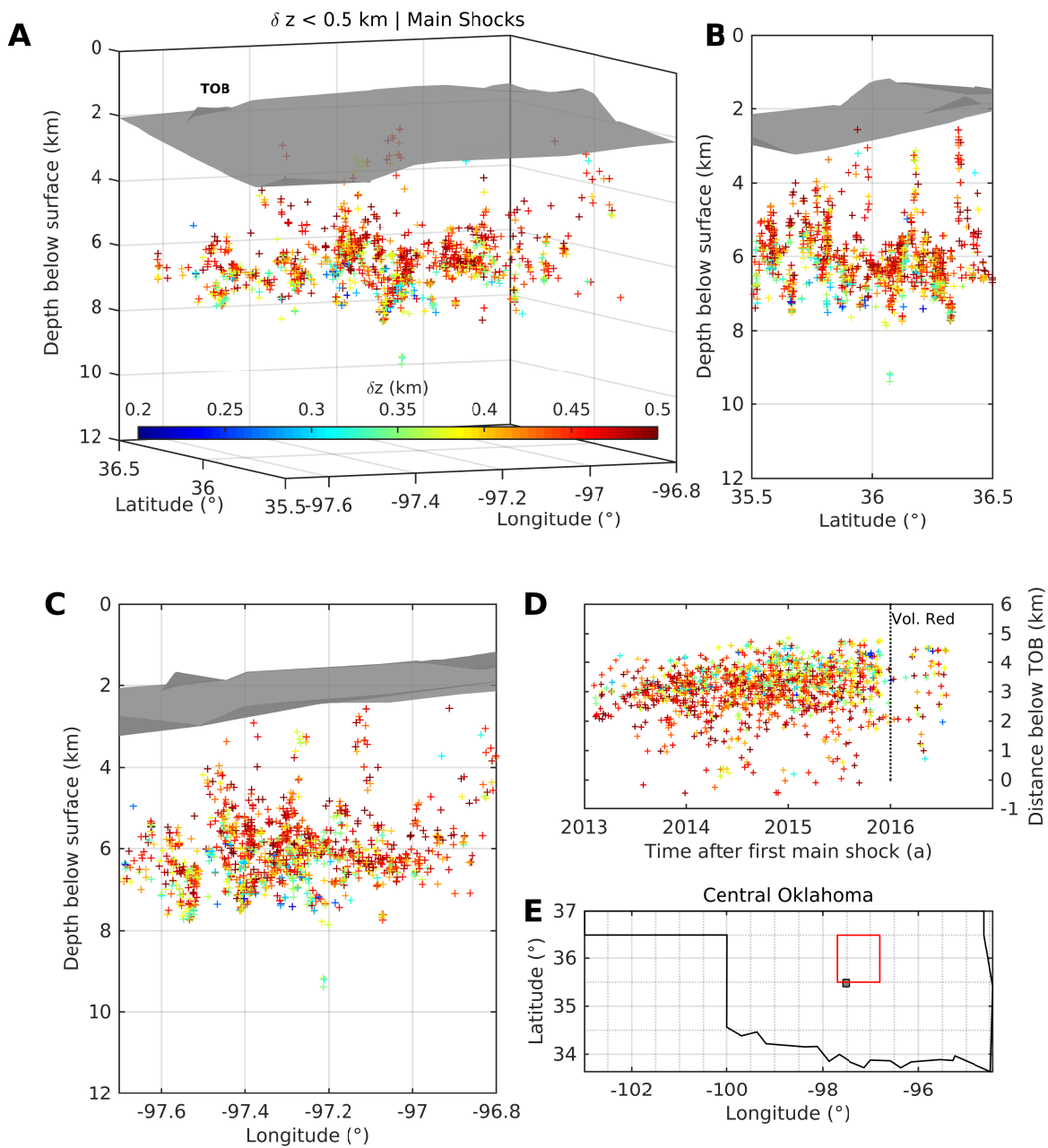


Figure S2. Main shocks of seismicity in Central Oklahoma from May 2013 to November 2016. Same as Figure S1 but showing only the obtained main shocks. Data by¹

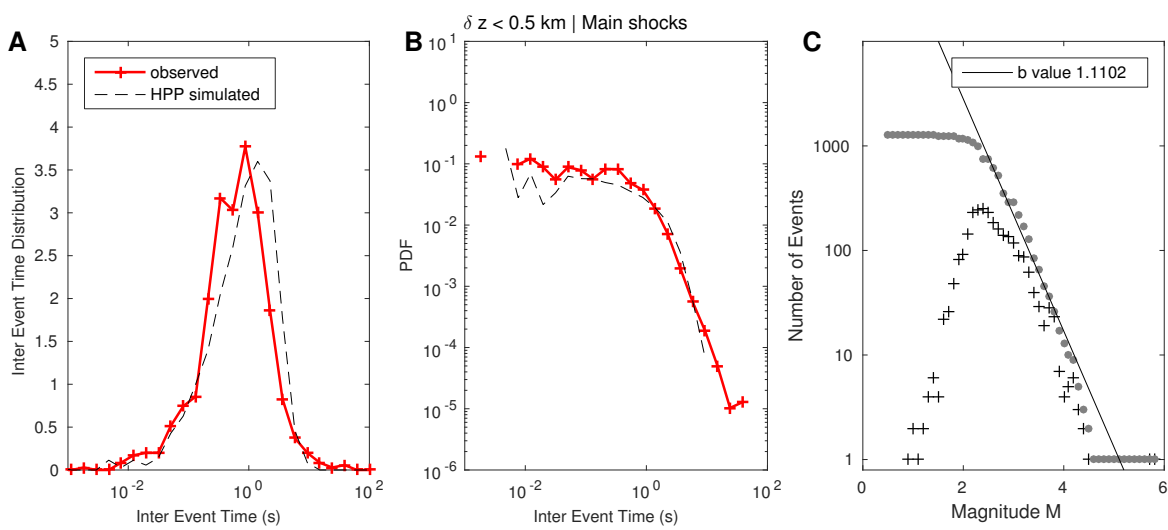


Figure S3. Inter event times and Gutenberg-Richter representation of the identified main shocks. Using a declustering algorithm, dependent events were removed from the catalogue. According to previous works, main shocks should follow a homogeneous Poisson process^{2,15}. As shown in panels (A) - (B), the identified mains shocks are distributed as expected. Panel (C) is a classical Gutenberg-Richter plot.

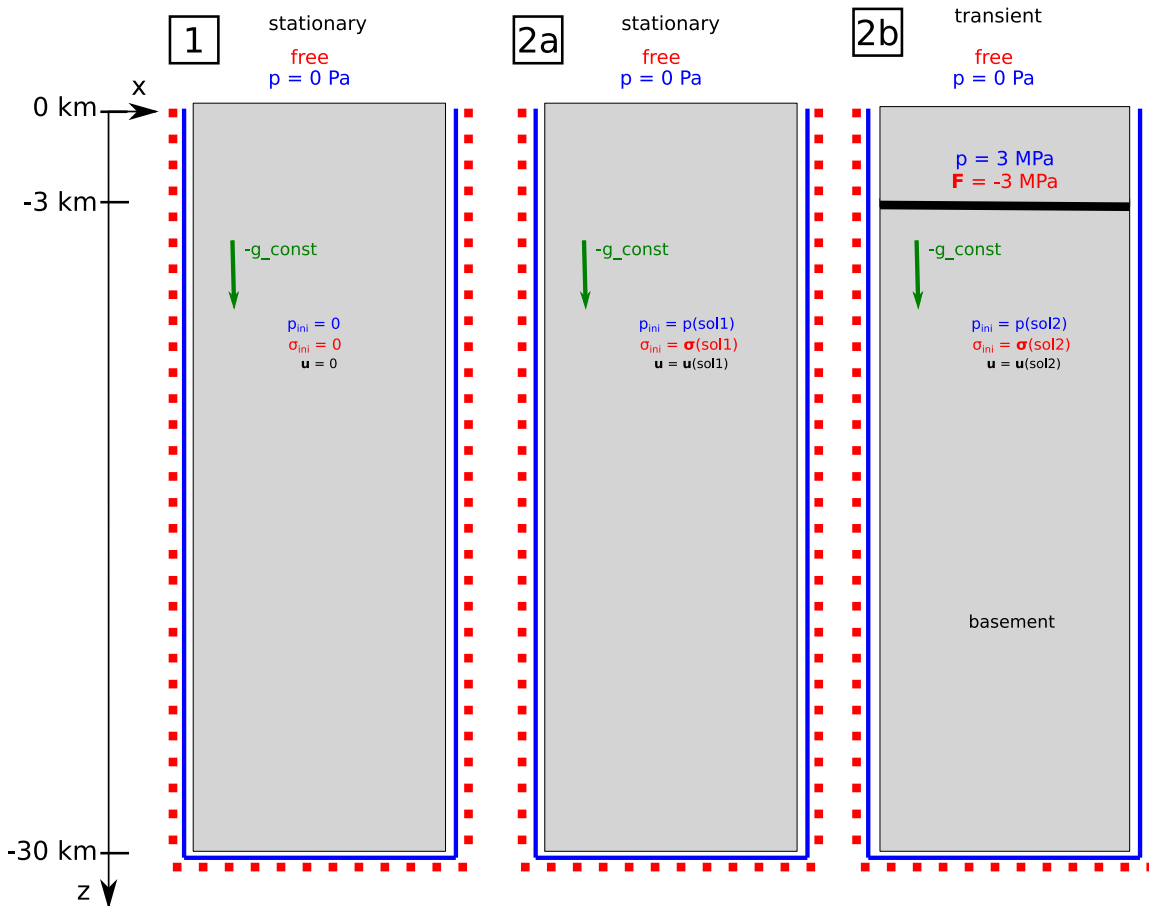


Figure S4. Geometry and boundary conditions (BC) in the numerical model. For the application of 2D plane strain, we define a block that extends in the vertical z -direction. Regarding hydrological BC, The outer boundaries are given by no flow (blue line), whereas the pressure at the top boundary is set to 0 Pa. For the elastic BC, we use so-called roller boundaries (red dotted line), i.e. movement normal to the boundaries is permitted. The top boundary is given by a free surface condition. To compute the transient solution (2b), two stationary solutions (1) and (2a) are necessary which yield the initial conditions for the transient model.

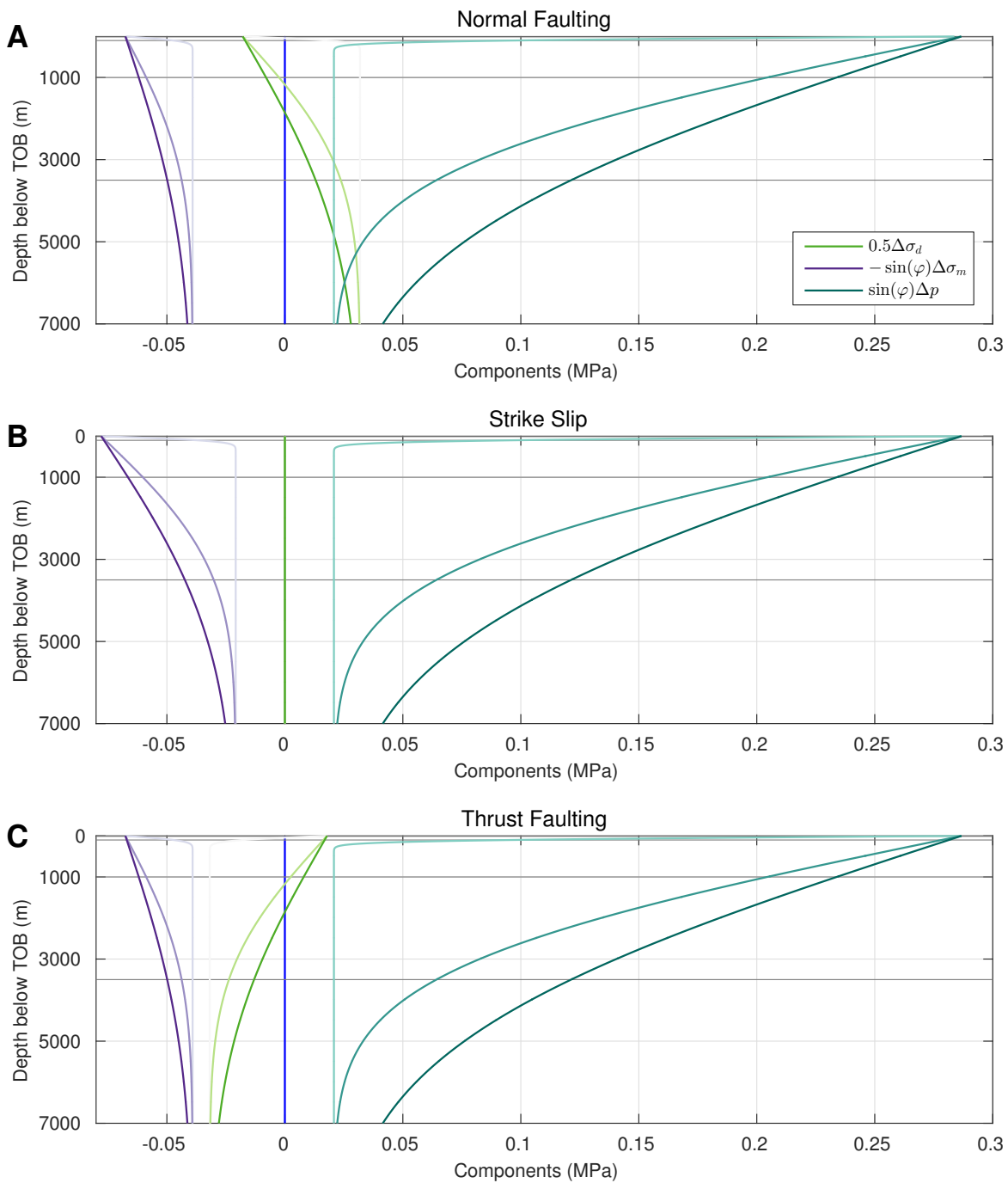


Figure S5. Components of ΔFCS for different tectonic regimes, shown for different time steps (light to dark) as profiles along the depth. While the magnitude of the components $0.5\Delta\sigma_d$ (magenta) and $-\sin(\varphi)\Delta\sigma_m$ (green) is affected by the tectonic setting (see text for discussion), $\sin(\varphi)\Delta p$ (blue) is independent of the stress regime. $0.5\Delta\sigma_d$ is zero throughout the medium in a strike-slip regime (**B**), but its value changes from negative at the TOB (stabilisation) to positive (destabilisation) at depth in a normal faulting environment (**A**). In a thrust faulting regime (**C**) it is vice versa. In contrast, the component $0.5\Delta\sigma_d$ is negative (stabilisation) in all regimes while $\sin(\varphi)\Delta p$ is positive independently of the regime. The sum of all components yields ΔFCS . Compare to Figure 4.

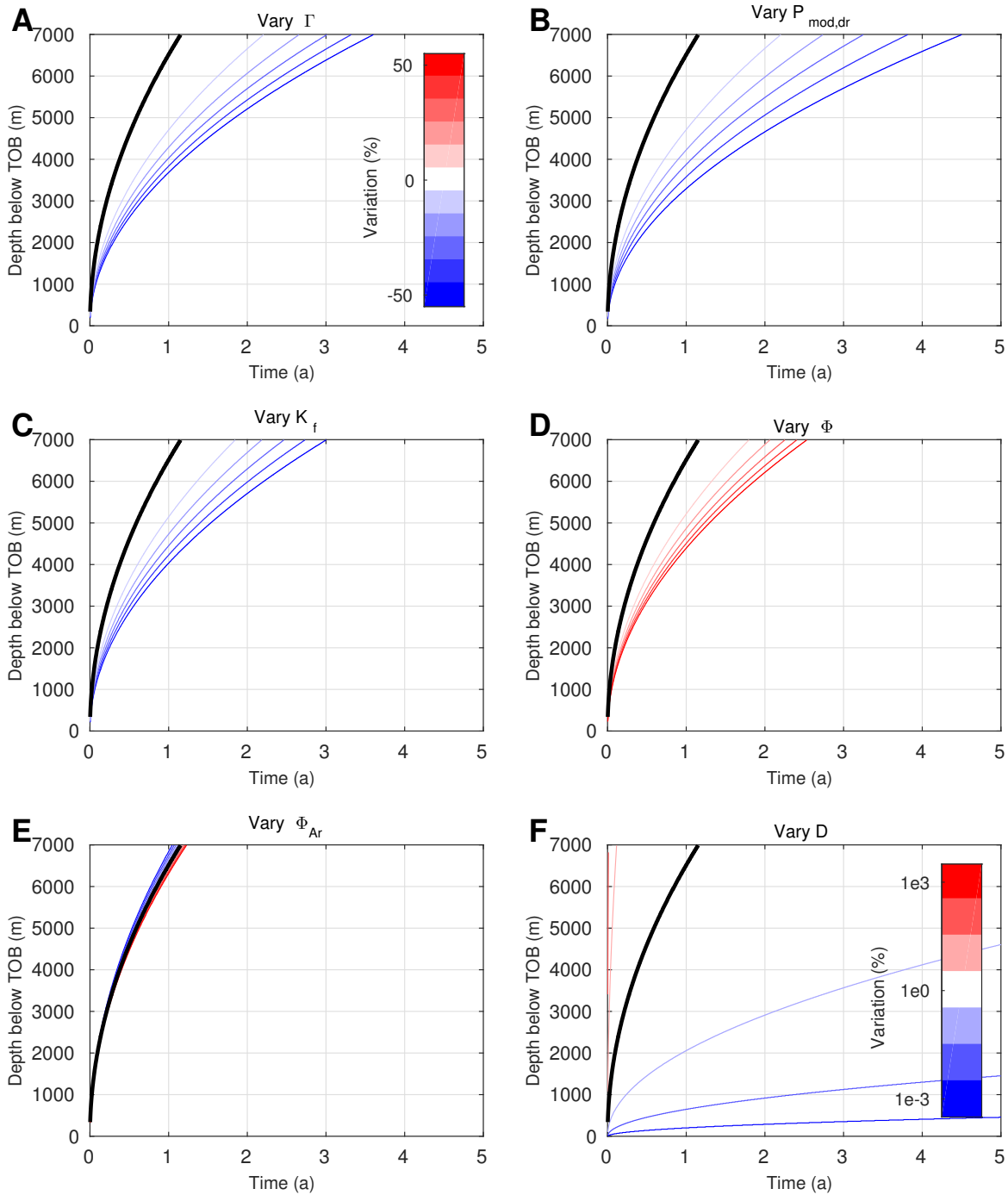


Figure S6. Parameter dependence of the destabilisation front. Blue to red lines mark smaller to higher parameter values. Fronts, obtained for the base level values as used in the modeling are depicted by the solid black line. Parameters Γ (A), $P_{mod,dr}$ (B), K_f (C) and D (F) are positively correlated to the evolution of the destabilisation front. The higher the parameter, the faster the front penetrates the medium. In contrast, increasing Φ (D) and Φ_{Ar} (G) lead to a slower penetration of the front.

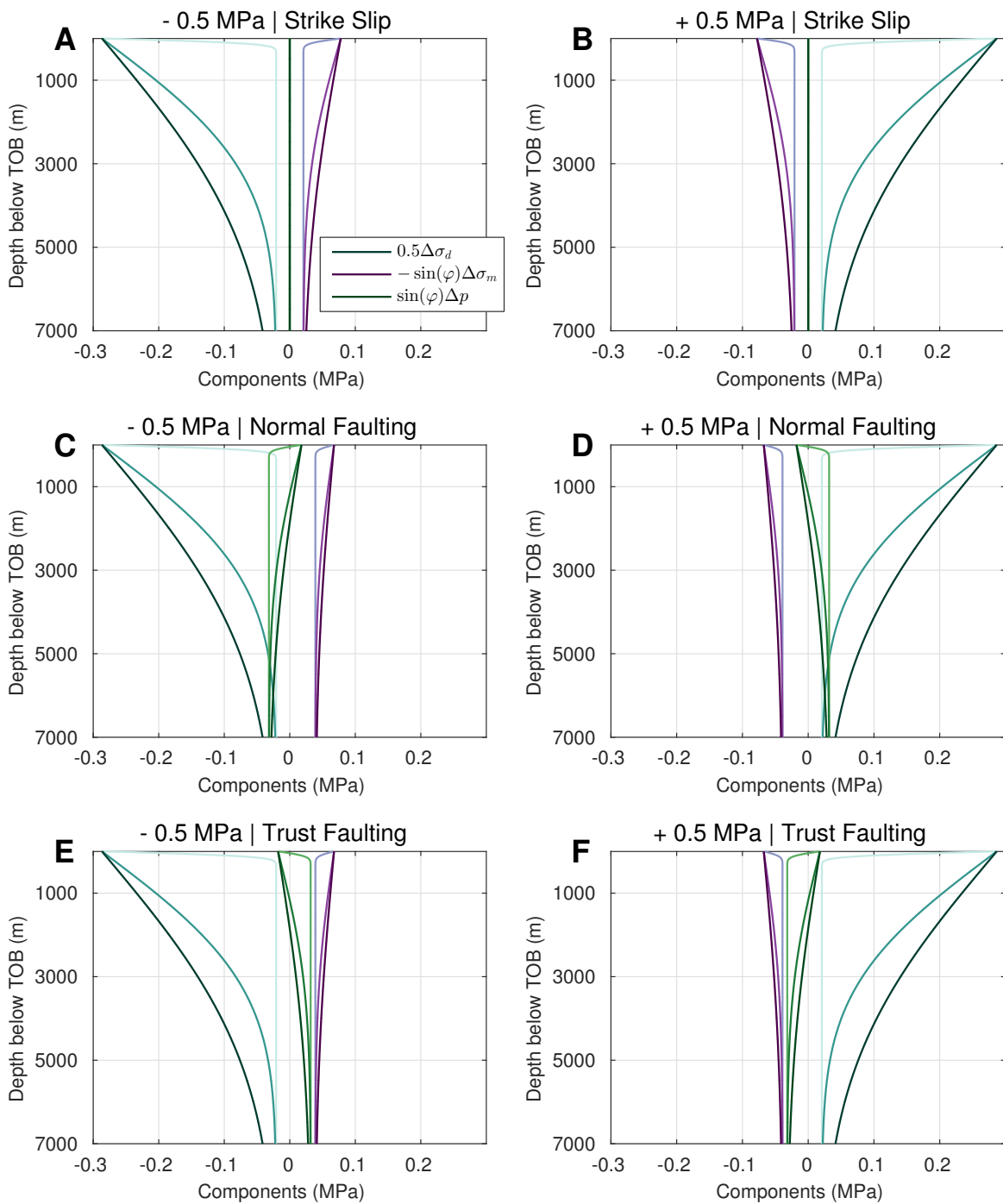


Figure S7. Components of ΔFCS for different tectonic regimes. Same as Fig. S5, but for negative (left) and positive values (right) of p_0 , i.e. fluid reduction and injection, respectively. The figure points to the importance of considering poroelastic coupling in the URIS model. The sum of all three components yields an estimate of ΔFCS , shown in Figure S8.

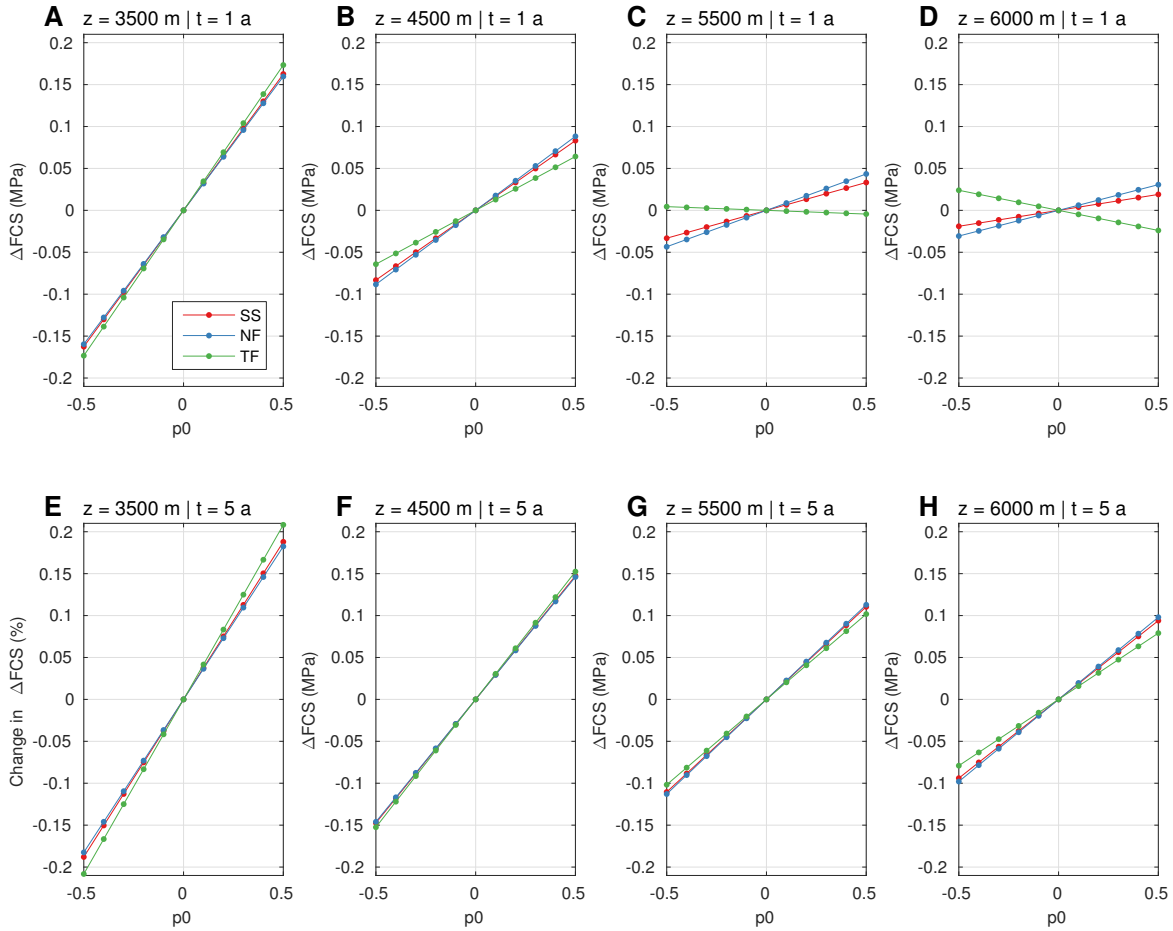


Figure S8. ΔFCS for varying p_0 in different stress regimes. Dependent on the time (top and bottom) and depth (from left to right), the value of ΔFCS is also controlled by the tectonic regime and the assumption of positive or negative p_0 , i.e. fluid injection or reduction, respectively. In case of fluid injection in a strike-slip regime (red), the medium is destabilised most in vicinity to the injection layer (**A**). This effect weakens with distance but intensifies with time (compare **D** and **H**). In a thrust faulting environment (green), even though the medium is also destabilised close to the injection formation (**A**) but significantly stabilised at greater depth **D**. Yet, as soon as the pore pressure rises due to diffusion, destabilisation also occurs far from the injector **H**. In contrast, the situation is different under negative pressures (i.e. fluid production). Whereas locations close to as well as far away from the upper boundary are stabilised under strike-slip conditions (red line in **A** - **D**), locations at greater depth are destabilised in a thrust faulting regime (green line in **D**). Such an effect is attributable to poroelastic coupling as the main controlling factor at greater depth. As soon as pressure diffusion has reached these locations, the medium is also destabilised under thrusting conditions (**H**).

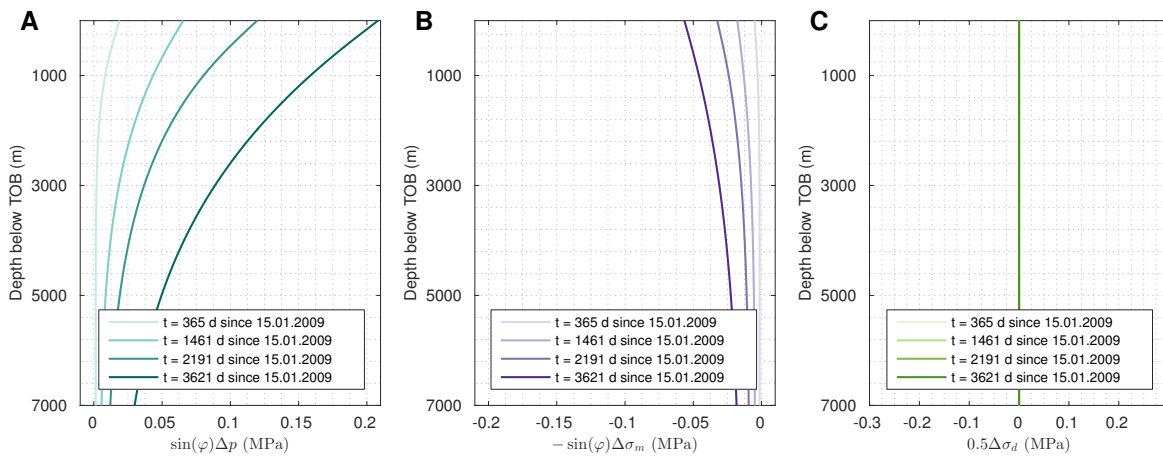


Figure S9. Components of ΔFCS for the time-dependent boundary condition. These are $\sin\varphi\Delta p$ (A), $-\sin\varphi\Delta\sigma_m$ (B) and $0.5\Delta\sigma_d$ (C). Assuming a background strike-slip regime and equal horizontal stress magnitudes $\Delta\sigma_H = \Delta\sigma_h$, the change of the failure stress is given by $\Delta FCS = \sin\varphi(\Delta p - \Delta\sigma_3)$, where $\Delta\sigma_3$ is the change of the minimum principal stress and Δp is the pressure perturbation.

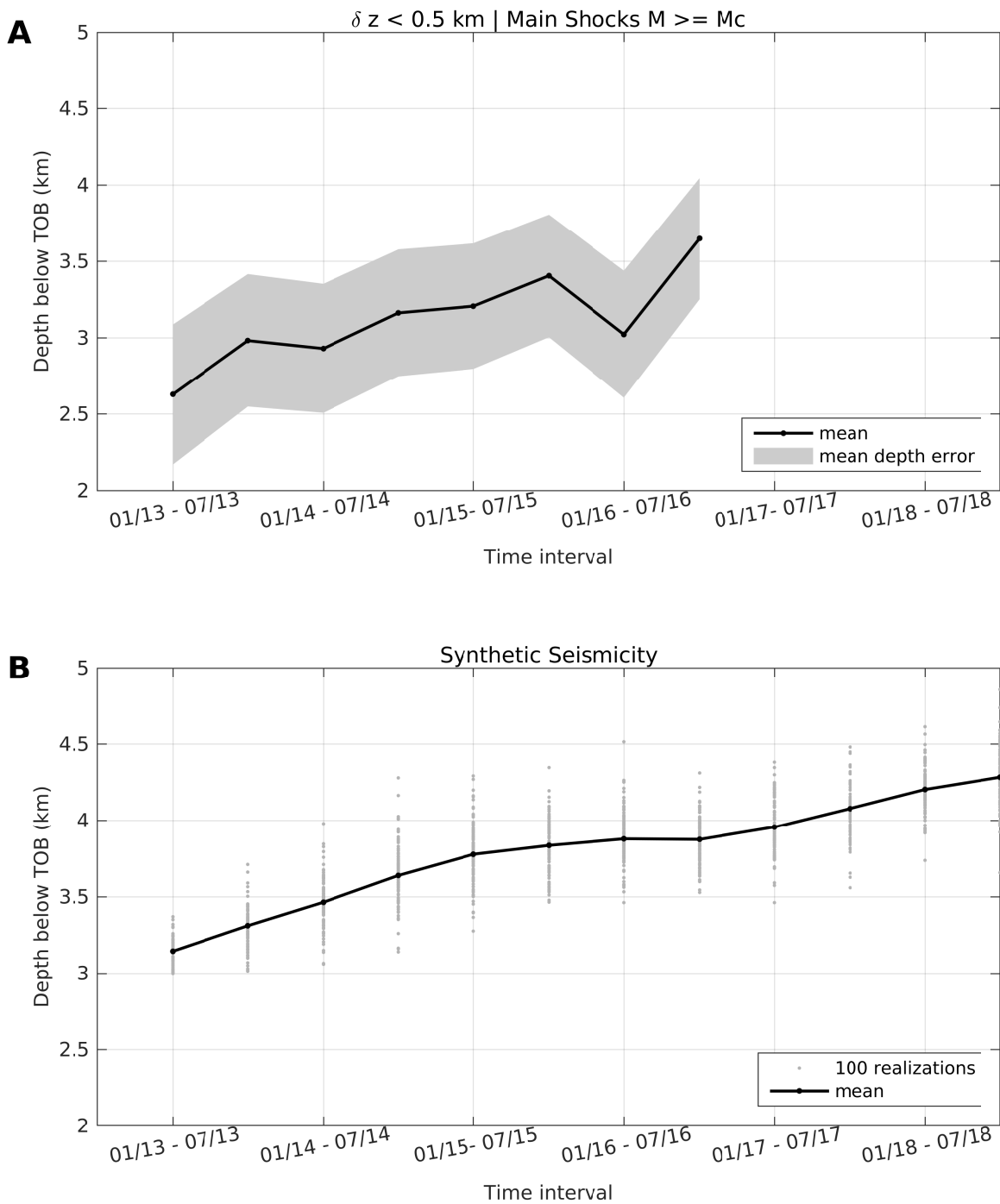


Figure S10. $r-t$ -plots of seismicity, showing the earthquake depth below the top of the basement (TOB) versus their occurrence time. In the study area ((A)), main shocks with a depth error $\delta z < 0.5 \text{ km}$, the seismically active zone shifts to greater depth with time within the margin of depth uncertainty (grey shaded area). Overall, the seismogenic depth is between 2.5 km and 4 km. Synthetic seismicity ((B)), generated using numerical results and implementing a total of 100 realisations of the criticality C (grey dots), follows the same spatio-temporal trend as observed in Central Oklahoma.

References

1. Schoenball, M. & Ellsworth, W. Waveform-Relocated Earthquake Catalog for Oklahoma and Southern Kansas Illuminates the Regional Fault Network. *Seism. Res. Lett.* **88** (2017). DOI 10.1785/0220170083.
2. Ogata, Y. Space-time point-process models for earthquake occurrences. *Annals Inst. Stat. Math.* **50**, 379–402 (1998). DOI 10.1023/A:1003403601725.
3. Schoenball, M. & Ellsworth, W. L. A Systematic Assessment of the Spatiotemporal Evolution of Fault Activation Through Induced Seismicity in Oklahoma and Southern Kansas. *J. Geophys. Res. Solid Earth* **122**, 10189–10206 (2017). DOI 10.1002/2017JB014850.
4. Urhammer, R. A. Characteristics of northern and central california seismicity. *Earthq. Notes* **57**, 21 (1986).
5. Gutenberg, B. & Richter, C. F. Frequency of earthquakes in California. *Bull. Seism. Soc. Am.* **34**, 185–188 (1944).
6. Shapiro, S. *Fluid-Induced Seismicity* (Cambridge Univerisity Press, Cambridge, U.K., 2015).
7. Detournay, E. & Cheng, A. *Fundamentals of Poroelasticity*, vol. 2 (Pergamon Press, 1993).
8. Snow, D. Geodynamics of seismic reservoirs. In *Symposium on Percolation Through Fissured Rock*, T2 – J: 1 – 19 (Deutsche Gesellschaft für Erd- und Grundbau, Germany, 1972).
9. Shapiro, S. A. & Dinske, C. Scaling of seismicity induced by nonlinear fluid-rock interaction. *J. Geophys. Res. Solid Earth* **114**, 14pp (2009). DOI 10.1111/j.1365-2478.2008.00770.x.
10. Hummel, N. & Shapiro, S. A. Microseismic estimates of hydraulic diffusivity in case of non-linear fluid-rock interaction. *Geophys. J. Int.* **188**, 1441–1453 (2012). DOI 10.1111/j.1365-246X.2011.05346.x.
11. Langenbruch, C. & Shapiro, S. Gutenberg-Richter relation originates from Coulomb stress fluctuations caused by elastic rock heterogeneity. *J. Geophys. Res. Solid Earth* **119** (2014). DOI 10.1002/2013JB010282.

12. Norbeck, J. H. & Horne, R. N. Evidence for a transient hydromechanical and frictional faulting response during the 2011 Mw 5.6 Prague, Oklahoma earthquake sequence. *J. Geophys. Res. Solid Earth* **121**, 8688–8705 (2016). DOI 10.1002/2016JB013148.
13. Chang, K. W. & Segall, P. Injection-induced seismicity on basement faults including poroelastic stressing. *J. Geophys. Res. Solid Earth* **121**, 2708 – 2726 (2016). DOI 10.1002/2015JB012561.
14. Campbell, J. A. & Weber, J. L. Wells drilled to Basement in Oklahoma. *Okla. Geol. Surv. Special Publ.* **1** (2006).
15. Langenbruch, C., Dinske, C. & Shapiro, S. A. Inter event times of fluid induced earthquakes suggest their Poisson nature. *Geophys. Res. Lett.* **38** (2011). DOI 10.1029/2011GL049474. L21302.

CHAPTER 5

Understanding Vectorial Migration Patterns of Wastewater-Induced Earthquakes in the United States¹

For copyright reasons, this chapter was removed from the digital version

¹ This article has been published in the Bulletin of the Seismological Society of America: L. Johann and S. A. Shapiro (2020). Understanding vectorial migration patterns of wastewater induced earthquakes in the United States. DOI: <https://doi.org/10.1785/0120200064>. Published by the Seismological Society of America (SSA). All Rights Reserved.

CHAPTER 6

Conclusions and Outlook

Fluid injections into the critically stressed subsurface are understood to have the potential of inducing earthquakes. Due to the injected fluid, the in situ pressure- and stress fields are perturbed. Consequently, these changes, if large enough, may cause slippage along pre-existing faults, resulting in the observed seismic activity. Although it is accepted by the scientific community that fluid-induced seismicity results from pressure- and stress changes, governing parameters and details of physical processes, including site specific effects, are still widely discussed. Therefore, modelling approaches have tended to become increasingly complex over the past years. This introduces more unknowns to the models as well as uncertainties and errors in the results. However, precise and reliable models as well as a sound understanding of the governing mechanisms are fundamental for seismic hazard assessment and risk mitigation.

In this thesis, I presented three works that focus on the analysis of fluid-induced seismicity. I investigated physical processes and governing parameters of earthquakes induced by both the localised effect of single-borehole, high-pressure fluid-injections and the regional impact of wastewater disposal through numerous wells spread over a larger area. The main findings, summarised in the following, may be used to improve future injection operations. Additionally, they form a basis to mitigate the seismic hazard posed by the different fluid operations.

I applied the triggering front approach (Shapiro et al., 1997, 1999; Shapiro and Dinske, 2009) to seismicity induced in the postinjection phase of high-pressure

fluid injections (Parotidis et al., 2004; Hummel and Shapiro, 2016), based on the assumption of non-linear pore-fluid pressure diffusion (Johann et al., 2016). The derived novel scaling relation (equation (2.24)) reveals that postinjection-induced seismicity is mainly controlled by the non-linearity of the pressure diffusion, n , and the Euclidean dimension of pore-fluid pressure diffusion, d . Numerical modelling of two end-member scenarios regarding the behaviour of the hydraulic diffusivity in the postinjection interval was carried out to validate the novel scaling law. Whereas I assumed a reversible *elastic* behaviour in the first model, a *frozen* (fixed) hydraulic diffusivity (Hummel and Shapiro, 2012, 2016) was implemented in the second realisation. The subsequent application of the scaling relation to field data demonstrated that the scaling can be used to obtain estimates of the two seismicity controlling parameters d and n .

Numerical modelling was also used to explain recent earthquakes in the central U.S, induced by wastewater disposal. In this region of the U.S., massive volumes of saline wastewater are injected under gravity feed into a highly porous, underpressured aquifer.

Throughout central Oklahoma, earthquakes preferably occur in the crystalline basement, below large-volume disposal areas. To explain spatio-temporal features of seismicity observed between January 2013 and November 2016 (Schoenball and Ellsworth, 2017b), I developed a new first-principle model, called underground reservoir-induced seismicity (*URIS*, Johann et al., 2018). It is assumed that the large-volume fluid injection causes the filling of the pore space of the underpressured injection formation which adds an effective water layer on top of the underlying basement. The physics of the URIS model are based upon reservoir-induced seismicity (e.g. Talwani, 1997; Gupta, 1992), where the combination of the weight of the added water column (acting as a vertical normal stress on the underlying formation), the pore-fluid pressure below this water column (leading to pore-fluid pressure diffusion in the underlying formation), and poroelastic coupling (provoking pore-fluid pressure- and stress changes), contributes to Coulomb stress changes. If these perturbations are large enough, pre-existing basement faults may be activated, resulting in shear failure along these faults, and thus in seismic activity. In the study area, hypocentre locations seem to shift to greater depth with time, a pattern that is well captured by the URIS model during both constant and declining disposal volumes.

In contrast, earthquake activity in southern Kansas recorded between January 2015 and June 2017 seems to follow a horizontal shift towards the north-east with time, away from high-volume disposal wells (e.g. Peterie et al., 2018). To study the migration patterns, I developed a comprehensive approach, combining results from a time-dependent, spatially two-dimensional cross-correlation between earthquake rates and disposal volumes with two-dimensional numerical modelling of poroelastic pressure- and stress changes (Johann and Shapiro, 2020).

Eventually, failure criterion stress changes could be calculated from the obtained numerical solutions. The analysis indicated that the observed large-scale seismicity patterns are attributable to pressure- and stress changes in the injection formation and in the seismically active crystalline basement. Furthermore, it was shown that the permeability of the basement and its anisotropic character as well as the distribution of critical fault strengths in the basement control seismic features in time and space in this region. The results suggest that the mandated volume reduction plan affects seismicity only locally and that the hazard due to induced earthquakes may remain elevated for many more years.

Although promising results were obtained by the studies presented in this thesis, the work proves once again the importance of optimal microseismic monitoring systems and data availability (Grigoli et al., 2017). Precise event locations as well as the access to earthquake catalogues and operational data are basic tools for research based on fluid-induced seismicity such as reservoir characterisation (e.g. Shapiro et al., 1997, 1999; Fehler et al., 2001) and the investigation of seismicity controlling mechanisms as presented here. The study on the back front of induced seismicity revealed that case studies are frequently limited by a poor data quality after the injection stop. That is, microseismic monitoring systems are often turned off directly after the injection phase due to economic reasons, causing a lack of microseismic event data. In case of wastewater disposal-induced earthquakes, the presented works were restricted by the availability of disposal- and high-precision earthquake data. Making these data publicly available would be a great advantage for possible future studies, some of which proposed below.

Outlook

Based on the analysis of fluid-induced seismicity, Shapiro et al. (2010) introduced the so-called *seismogenic index* (SI, Σ) to quantify the seismogenic reaction of a rock mass to underground fluid injections, which is a valuable tool for seismic risk assessment. The SI expresses a proportionality between the injected volume and the number of induced earthquakes with a magnitude larger than a given one. The larger its value, the higher the probability of large-magnitude events. In its general form, the SI is given by: $\Sigma = a - \log NC_{max}/S$, where N is the bulk volume concentration of pre-existing fractures, C_{max} denotes the maximum critical stress value necessary to cause shear failure on pre-existing faults, and S is the poroelastic uniaxial storage coefficient. The parameter a is a seismogenic constant from the Gutenberg-Richter Law (Shapiro et al., 2010). It has been shown that Σ is a site-specific quantity and remains constant with time (Shapiro et al., 2010; Dinske and Shapiro, 2013; Hajati et al., 2015). Thus, once determined from observed seismicity, it may be used for earthquake hazard estimations. Langenbruch and Zoback (2016); Langenbruch et al. (2018) slightly modified the

expression of the seismogenic index and applied it to the wastewater disposal-induced earthquakes in Oklahoma, assuming the effect of pore-fluid pressure diffusion. Based on Σ , they estimated the seismic hazard throughout Oklahoma and southern Kansas. Shapiro (2018) adopted the SI model to fluid production operations, taking also the effect of poroelastic coupling into account. As has been demonstrated by these recent works, the SI model is applicable to different types of fluid-induced seismicity. Therefore, one future research direction might be a modification of Σ with regard to the proposed URIS model, thus accounting for the loading of the seismogenic basement by an effective water column in the target disposal formation on top of the basement.

Despite the fact that the recent, unprecedented surge in earthquakes throughout Oklahoma and Kansas is indisputably the most striking example of wastewater disposal-induced seismicity, this type of man-made earthquakes has been noted at other sites in the U.S. and worldwide throughout the last decade. Some examples, albeit of much smaller scale, are a sequence of ongoing seismicity in Northern New Mexico/Southern Colorado with one recorded $M5.3$ earthquake (Rubinstein et al., 2014), seismic activity close to disposal wells in Arkansas, U.S., with one $M4.7$ event in 2011 (Horton, 2012), and the Dallas-Fort Worth sequence in Texas which may be responsible for one $M3.4$ earthquake in 2012 (Frohlich et al., 2011; Ogwari et al., 2018). Apart from these cases in the U.S., some European cases of earthquakes linked to wastewater disposal have been discussed in literature. One example is the Val d'Agri Oil Field in south-western Italy where wastewater has been injected since June 2006 through one well at a rate of tens of thousands of cubic meters per month. As a consequence, several thousand small magnitude events ($-0.2 \leq M_L \leq 2.7$) have been recorded (Improta et al., 2015). To study spatio-temporal patterns of these smaller scale cases of wastewater disposal-induced earthquakes, it would be interesting to apply the developed URIS model.

Furthermore, developments of the implemented numerical models would yield a great advantage for future studies. For the Kansas case study, I performed numerical modelling with one axis parallel to the predominant direction of seismicity migration observed in the south of Kansas. A possible next step for this study area would be the set-up of a hydraulically anisotropic numerical model. This could be done in 2D or possibly also in 3D.

Even though the thesis demonstrated that the physics of seismicity induced by various fluid operations remain a complex subject with the necessity of future studies, the work also illustrated that it is the elaborate combination of different scientific methods such as analytical solutions, numerical modelling and mathematical measures (here cross-correlations) that eventually yields promising results.

Bibliography

- Aki, K. and Richards, P. G. (2002). *Quantitative Seismology*. University Science Books, 2 edition.
- Asanuma, H., Soma, N., Kaieda, H., Kumano, Y., Izumi, T., Tezuka, K., Nitsuma, H., and Wyborn, D. (2005). Microseismic Monitoring of Hydraulic Stimulation at the Australian HDR Project in Cooper Basin. In *Proceedings World Geothermal Congress 2005*.
- Atkinson, G. M., Eaton, D. W., and Igonin, N. (2020). Developments in understanding seismicity triggered by hydraulic fracturing. *Nature Reviews Earth & Environment*, 1(5):264–277.
- Baisch, S., Rothert, E., Stang, H., Vörös, R., Koch, C., and McMahon, A. (2015). Continued Geothermal Reservoir Stimulation Experiments in the Cooper Basin (Australia). *Bull. Seismol. Soc. Am.*, 105(1):198–209.
- Baisch, S., Vörös, R., Rothert, E., Stang, H., Jung, R., and Schellschmidt, R. (2010). A numerical model for fluid injection induced seismicity at Soultz-sous-Forêts. *Int. J. Rock Mech. Min. Sci.*, 47(3):405–413.
- Biot, M. A. (1941). General theory of three-dimensional consolidation. *J. Appl. Phys.*, 12:155–164.
- Biot, M. A. (1962). Mechanics of Deformation and Acoustic Propagation in Porous Media. *J. Appl. Phys.*, 33(4):1482–1498.
- Bourne, S. J., Oates, S. J., van Elk, J., and Doornhof, D. (2014). A seismological model for earthquakes induced by fluid extraction from a subsurface reservoir. *Journal of Geophysical Research: Solid Earth*, 119(12):8991–9015.
- Chang, K. W. and Segall, P. (2016). Injection-induced seismicity on basement faults including poroelastic stressing. *Journal of Geophysical Research: Solid Earth*, 121:2708–2726.

- Chen, X., Nakata, N., Pennington, C., Haffener, J., Chang, J. C., He, X., Zhan, Z., Ni, S., and Walter, J. I. (2017). The Pawnee earthquake as a result of the interplay among injection, faults and foreshocks. *Sci. Rep.*, 7(1):4945.
- Cook, N. (1976). Seismicity associated with mining. *Eng. Geol.*, 10(2):99–122.
- Coulomb, C. A. (1773). Essai sur une application des règles de maximis et minimis à quelques problèmes de statique, relatifs à l'architecture. Mémoires De Mathématique Et Physique Présenté À L'Académie Des Sciences Par Savantes Étrangères.
- Coussy, O. (2003). *Poromechanics*. John Wiley & Sons, Ltd.
- Deichmann, N. and Giardini, D. (2009). Earthquakes Induced by the Stimulation of an Enhanced Geothermal System below Basel (Switzerland). *Seismol. Res. Lett.*, 80(5):784–798.
- Detournay, E. and Cheng, A. (1993). *Fundamentals of Poroelasticity*, volume 2. Pergamon Press.
- Dieterich, J. (1994). A constitutive law for rate of earthquake production and its application to earthquake clustering. *Journal of Geophysical Research: Solid Earth*, 99(B2):2601–2618.
- Dinske, C. and Shapiro, S. A. (2013). Seismotectonic state of reservoirs inferred from magnitude distributions of fluid-induced seismicity. *J. Seismolog.*, 17:13–25.
- Dost, B. and Kraaijpoel, D. (2013). The August 16, 2012 earthquake near Huizinge (Groningen). Technical report, KNMI.
- Ellsworth, W. L. (2013). Injection-Induced Earthquakes. *Science*, 341(6142).
- Fehler, M. C. (1989). Stress control of seismicity patterns observed during hydraulic fracturing experiments at the Fenton Hill hot dry rock geothermal energy site, New Mexico. *International Journal of Rock Mechanics and Mining Sciences & Geomechanics Abstracts*, 26(3–4):211–219.
- Fehler, M., Jupe, A., and Asanuma, H. (2001). More Than Cloud: New techniques for characterizing reservoir structure using induced seismicity. *The Leading Edge*, 20(3):324–328.
- Foulger, G. R., Wilson, M. P., Gluyas, J. G., Julian, B. R., and Davies, R. J. (2018). Global review of human-induced earthquakes. *Earth Sci. Rev.*, 178:438–514.
- Frohlich, C., Hayward, C., Stump, B. ., and Potter, E. (2011). The Dallas–Fort Worth Earthquake Sequence: October 2008 through May 2009. *Bull. Seismol. Soc. Am.*, 101(1):327–340.
-

- Gahalaut, K. and Gahalaut, V. (2010). Effect of the Zipingpu reservoir impoundment on the occurrence of the 2008 Wenchuan earthquake and local seismicity. *Geophys. J. Int.*, 183(1):277–285.
- Geertsma, J. (1966). Problems of Rock Mechanics In Petroleum Production Engineering. In *1st Cong. of the Int. Soc. of Rock Mech.*, pages 585–594, Portugal. International Society of Rock Mechanics.
- Gibowicz, S. and Kijko, A. (1994). *An Introduction to Mining Seismology*, volume 55. Academic Press, 1 edition.
- Gischig, V. S. and Wiemer, S. (2013). A stochastic model for induced seismicity based on non-linear pressure diffusion and irreversible permeability enhancement. *Geophys. J. Int.*, 194(2).
- Goebel, T. H., Weingarten, M., Chen, X., Haffner, J., and Brodsky, E. E. (2017). The 2016 Mw5.1 Fairview, Oklahoma earthquakes: Evidence for long-range poroelastic triggering at >40 km from fluid disposal wells. *Earth Planet. Sci. Lett.*, 472:50–61.
- Grigoli, F., Cesca, S., Priolo, E., Rinaldi, A. P., Clinton, J. F., Stabile, T. A., Dost, B., Fernandez, M. G., Wiemer, S., and Dahm, T. (2017). Current challenges in monitoring, discrimination, and management of induced seismicity related to underground industrial activities: A European perspective. *Rev. Geophys.*, 55(2):310–340.
- Gupta, H. K. (2002). A review of recent studies of triggered earthquakes by artificial water reservoirs with special emphasis on earthquakes in Koyna, India. *Earth Sci. Rev.*, 58(3):279–310.
- Gupta, H. K. (1992). *Reservoir Induced Earthquakes*, volume 64. Elsevier Science.
- Hajati, T., Langenbruch, C., and Shapiro, S. A. (2015). A statistical model for seismic hazard assessment of hydraulic-fracturing-induced seismicity. *Geophys. Res. Lett.*, 42(24):10601–10606.
- Häring, M. O., Schanz, U., Ladner, F., and Dyer, B. C. (2008). Characterisation of the Basel 1 enhanced geothermal system. *Geothermics*, 37(5):469–495.
- Healy, J. H., Rubey, W. W., Griggs, D. T., and Raleigh, C. B. (1968). The Denver Earthquakes. *Science*, 161(3848):1301–1310.
- Horton, S. (2012). Disposal of Hydrofracking Waste Fluid by Injection into Sub-surface Aquifers Triggers Earthquake Swarm in Central Arkansas with Potential for Damaging Earthquake. *Seismol. Res. Lett.*, 83(2).
- Hsieh, P. A. and Bredehoeft, J. D. (1981). A Reservoir Analysis of the Denver Earthquakes: A Case of Induced Seismicity. *Journal of Geophysical Research: Solid Earth*, 86:903–920.
-

- Hubbert, M. K. and Willis, D. G. (1957). Mechanics of Hydraulic Fracturing. *Transactions of Society of Petroleum Engineers of AIME*, 210:153–168.
- Hummel, N. (2013). *Pressure dependent hydraulic transport as a model for fluid induced earthquakes*. PhD thesis, Freie Universität Berlin.
- Hummel, N. and Müller, T. M. (2009). Microseismic signatures of non-linear pore-fluid pressure diffusion. *Geophys. J. Int.*, 179:1558–1565.
- Hummel, N. and Shapiro, S. A. (2012). Microseismic estimates of hydraulic diffusivity in case of non-linear fluid-rock interaction. *Geophys. J. Int.*, 188(3):1441–1453.
- Hummel, N. and Shapiro, S. (2016). Back front of seismicity induced by non-linear pore pressure diffusion. *Geophysical Prospecting*, 64(1):170–191.
- Hummel, N. and Shapiro, S. A. (2013). Nonlinear diffusion-based interpretation of induced microseismicity: A Barnett Shale hydraulic fracturing case study. *Geophysics*, 78:B211 – B226.
- Improta, L., Valoroso, L., Piccinini, D., and Chiarabba, C. (2015). A detailed analysis of wastewater-induced seismicity in the Val d’Agri oil field (Italy). *Geophys. Res. Lett.*, 42(8):2682–2690.
- Jaeger, J. C., Cook, N. G., and Zimmermann, R. (2007). *Fundamentals of Rock Mechanics*. Wiley-Blackwell, 4 edition.
- Johann, L., Dinske, C., and Shapiro, S. A. (2016). Scaling of seismicity induced by nonlinear fluid-rock interaction after an injection stop. *Journal Geophysical Research: Solid Earth*, 121(11):8154–8174.
- Johann, L. and Shapiro, S. A. (2020). Understanding vectorial migration patterns of wastewater induced earthquakes in the U.S. *Bull. Seismol. Soc. Am.*
- Johann, L., Shapiro, S. A., and Dinske, C. (2018). The surge of earthquakes in Central Oklahoma has features of reservoir-induced seismicity. *Sci. Rep.*, 11505(8).
- Keranen, K. M., Savage, H. M., Abers, G. A., and Cochran, E. S. (2013). Potentially induced earthquakes in Oklahoma, USA: Links between wastewater injection and the 2011 Mw 5.7 earthquake sequence. *Geology*, 41(6):699–702.
- Keranen, K. M., Weingarten, M., Abers, G. A., Bekins, B. A., and Ge, S. (2014). Sharp increase in central Oklahoma seismicity since 2008 induced by massive wastewater injection. *Science*, 345(6195):448–451.
- Klose, C. D. (2011). Evidence for Anthropogenic Surface Loading as Trigger Mechanism of the 2008 Wenchuan Earthquake. *Environmental Earth Sciences*.
-

- Langenbruch, C. and Shapiro, S. (2010). Decay rate of fluid-induced seismicity after termination of reservoir stimulations. *Geophysics*, 75.
- Langenbruch, C., Weingarten, M., and Zoback, M. D. (2018). Physics-based forecasting of man-made earthquake hazards in Oklahoma and Kansas. *Nat. Commun.*, 9.
- Langenbruch, C. and Zoback, M. D. (2016). How will induced seismicity in Oklahoma respond to decreased saltwater injection rates? *Sci. Adv.*, 2(11).
- Lay, T. and Wallace, T. (1995). *Modern Global Seimology*, volume 58. Academic Press.
- Lei, X., Wang, Z., and Su, J. (2019). The December 2018 ML 5.7 and January 2019 ML 5.3 Earthquakes in South Sichuan Basin Induced by Shale Gas Hydraulic Fracturing. *Seismol. Res. Lett.*, 90(3):1099–1110.
- Lei, X.-L., Ma, S.-L., Wen, X.-Z., Su, J., and Du, F. (2008). Integrated analysis of stress and regional seismicity by surface loading - a case study of Zipingpu reservoir. *Seismology and Geology*, 30(4):1046–1064.
- McGarr, A., Simpson, D., and Seeber, L. (2002). Case Histories of Induced and Triggered Seismicity. In *International Handbook of Earthquake and Engineering Seismology, Part A*, volume 81, pages 647–661. Academic Press.
- Miller, S. A. (2015). Modeling enhanced geothermal systems and the essential nature of large-scale changes in permeability at the onset of slip. *Geofluids*, 15(1-2):338–349.
- Montgomery, C. and Smith, M. (2010). Hydraulic Fracturing: History of an Enduring Technology. *Journal of Petroleum Technology*.
- National Research Council (2013). *Induced Seismicity Potential in Energy Technologies*. The National Academies Press, Washington D. C.
- Nur, A. and Booker, J. R. (1972). Aftershocks Caused by Pore Fluid Flow? *Science*, 175(4024):885–887.
- Nur, A., Walls, J., Winkler, K., and Devilbiss, J. (1980). Effects of Fluid Saturation on Waves in Porous Rock and Relations to Hydraulic Permeability. *Society of Petroleum Engineers*.
- Ogwari, P. O., DeShon, H. R., and Hornbach, M. J. (2018). The Dallas-Fort Worth Airport Earthquake Sequence: Seismicity Beyond Injection Period. *Journal of Geophysical Research: Solid Earth*, 123(1):553–563.
- Parotidis, M., Shapiro, S. A., and Rothert, E. (2004). Back front of seismicity induced after termination of borehole fluid injection. *Geophys. Res. Lett.*, 31.
-

- Peterie, S. L., Miller, R. D., Intfen, J. W., and Gonzales, J. B. (2018). Earthquakes in Kansas Induced by Extremely Far-Field Pressure Diffusion. *Geophys. Res. Lett.*, 45(3):1395–1401.
- Rice, J. R. and Cleary, M. P. (1976). Some basic stress diffusion solutions for fluid-saturated elastic porous media with compressible constituents. *Rev. Geophys.*, 14(2):227–241.
- Rothert, E. and Shapiro, S. A. (2003). Microseismic monitoring of borehole fluid injections: Data modeling and inversion for hydraulic properties of rocks. *Geophysics*, 68:685–689.
- Rothert, E. and Shapiro, S. A. (2007). Statistics of fracture strength and fluid-induced microseismicity. *Journal of Geophysical Research: Solid Earth*, 112.
- Rubey, W. W. and Hubbert, M. K. (1959). Role of Fluid Pressure in Mechanics of Overthrust Faulting. *Geol. Soc. Am. Bull.*, 70(2):167–206.
- Rubinstein, J. L., Ellsworth, W. L., McGarr, A., and Benz, H. M. (2014). The 2001–Present Induced Earthquake Sequence in the Raton Basin of Northern New Mexico and Southern Colorado. *Bull. Seismol. Soc. Am.*, 104(5).
- Rudnicki, J. W. (1986). Fluid Mass Sources and Point Forces in Linear Elastic Diffusive Solids. *Mechanics of Materials*, 5:383–393.
- Schoenball, M. and Ellsworth, W. L. (2017a). A Systematic Assessment of the Spatiotemporal Evolution of Fault Activation Through Induced Seismicity in Oklahoma and Southern Kansas. *Journal of Geophysical Research: Solid Earth*, 122(12):10189–10206.
- Schoenball, M. and Ellsworth, W. L. (2017b). Waveform-Relocated Earthquake Catalog for Oklahoma and Southern Kansas Illuminates the Regional Fault Network. *Seismol. Res. Lett.*, 88(4).
- Schoenball, M., Müller, T. M., Müller, B. I., and Heidbach, O. (2010). Fluid-induced microseismicity in pre-stressed rock masses. *Geophys. J. Int.*, 180(2):813–819.
- Segall, P. (2010). *Earthquake and Volcano Deformation*. Princeton University Press.
- Segall, P. and Lu, S. (2015). Injection-induced seismicity: Poroelastic and earthquake nucleation effects. *Journal of Geophysical Research: Solid Earth*, 120:5082–5103.
- Shapiro, S. A. (2015). *Fluid-Induced Seismicity*. Cambridge University Press, Cambridge, U.K.
-

- Shapiro, S. A. (2018). Seismogenic Index of Underground Fluid Injections and Productions. *Journal of Geophysical Research: Solid Earth*, 123(9):7983–7997.
- Shapiro, S. A., Audigane, P., and Royer, J.-J. (1999). Large-scale in situ permeability tensor of rocks from induced microseismicity. *Geophys. J. Int.*, 137:207–213.
- Shapiro, S. A. and Dinske, C. (2009). Scaling of seismicity induced by nonlinear fluid-rock interaction. *Journal of Geophysical Research: Solid Earth*, 114:14.
- Shapiro, S. A., Dinske, C., Langenbruch, C., and Wenzel, F. (2010). Seismogenic index and magnitude probability of earthquakes induced during reservoir fluid stimulations. *The Leading Edge*, 29(3):304–309.
- Shapiro, S. A., Huenges, E., and Borm, G. (1997). Estimating the permeability from fluid-injection induced seismic emission at the KTB site. *Geophys. J. Int.*, 131:F15–F18.
- Shapiro, S. A., Rothert, E., Rath, V., and Rindschwentner, J. (2002). Characterization of fluid transport properties of reservoirs using induced microseismicity. *Geophysics*, 67:212–220.
- Shearer, P. M. (2009). *Introduction to Seismology*. Cambridge University Press, 2 edition.
- Simpson, D. W. (1976). Seismicity changes associated with reservoir loading. *Eng. Geol.*, 10(2):123–150.
- Simpson, D. W., Leith, W. S., and Scholz, C. H. (1988). Two types of reservoir-induced seismicity. *Bull. Seismol. Soc. Am.*, 78(6):2025–2040.
- Suckale, J. (2009). Induced seismicity in hydrocarbon fields. In Dmowska, R., editor, *Advances in Geophysics*, volume 51 of *Advances in Geophysics*, chapter 2, pages 55–106. Elsevier, USA.
- Talwani, P. (1995). Speculation on the causes of continuing seismicity near Koyna reservoir, India. *Pure Appl. Geophys.*, 145(1):167–174.
- Talwani, P. (1997). On the Nature of Reservoir-induced Seismicity. *Pure Appl. Geophys.*, 150:473–492.
- Talwani, P. and Acree, S. (1984). Pore pressure diffusion and the mechanism of reservoir-induced seismicity. *Pure Appl. Geophys.*, 122(6):947–965.
- Tao, W., Masterlark, T., Shen, Z.-K., and Ronchin, E. (2015). Impoundment of the Zipingpu reservoir and triggering of the 2008 Mw 7.9 Wenchuan earthquake, China. *Journal of Geophysical Research: Solid Earth*, 120(10):7033–7047.
-

- Terzaghi, K. (1936). The shearing resistance of saturated soils and the angle between planes of shear. In *International Conference on Soil Mechanics and Foundation Engineering*, volume 1, pages 54–56. Harvard University Press, Cambridge, MA.
- Todd, D. K. (1964). *Groundwater Hydrology*. Wiley, New York, 4 edition.
- van Eck, T., Goutbeek, F., Haak, H., and Dost, B. (2006). Seismic hazard due to small-magnitude, shallow-source, induced earthquakes in The Netherlands. *Eng. Geol.*, 87(1):105–121.
- Van Wees, J. D., Buijze, L., Van Thienen-Visser, K., Nepveu, M., Wassing, B. B., Orlic, B., and Fokker, P. A. (2014). Geomechanics response and induced seismicity during gas field depletion in the Netherlands. *Geothermics*, 52:206–219.
- Walsh, F. R. and Zoback, M. D. (2015). Oklahoma’s recent earthquakes and saltwater disposal. *Sci. Adv.*, 1(5).
- Wang, H. F. (2000). *Theory of Linear Poroelasticity with Applications to Geomechanics and Hydrogeology*. Princeton University Press.
- Warpinski, N., Du, J., and Zimmer, U. (2012). Measurements of Hydraulic-Fracture-Induced Seismicity in Gas Shales. *SPE Production & Operations*, 27(3).
- Weingarten, M., Ge, S., Godt, J. W., Bekins, B. A., and Rubinstein, J. L. (2015). High-rate injection is associated with the increase in U.S. mid-continent seismicity. *Science*, 348(6241):1336–1340.
- Yeck, W. L., Hayes, G. P., McNamara, D. E., Rubinstein, J. L., Barnhart, W. D., Earle, P. S., and Benz, H. M. (2017). Oklahoma experiences largest earthquake during ongoing regional wastewater injection hazard mitigation efforts. *Geophys. Res. Lett.*, 44(2):711–717.
- Zbinden, D., Rinaldi, A. P., and Diehl, T. and Wiemer, S. (2020). Hydromechanical Modeling of Fault Reactivation in the St. Gallen Deep Geothermal Project (Switzerland): Poroelasticity or Hydraulic Connection? *Geophys. Res. Lett.*, 47(3).
-

Curriculum Vitae

For privacy reasons, the CV was removed in the digital version.

Publications and Conference Abstracts

Johann, L. and Shapiro, S. A. (2020). Understanding vectorial migration patterns of wastewater induced earthquakes in the U.S. *Bull. Seismol. Soc. Am.*. doi:10.1785/0120200064

Johann, L., Shapiro, S. A. and Dinske, C. (2018). The surge of earthquakes in Central Oklahoma has features of reservoir-induced seismicity. *Sci. Rep.*, 8. doi:10.1038/s41598-018-29883-9

Carcione, J. M., Currenti, G., **Johann, L.** and Shapiro, S. A. (2018). Modeling fluid injection induced microseismicity in shales. *J. Geophys. Eng.*, 15(1):234–248. doi:10.1088/1742-2140/aa8a27

Johann, L., Dinske, C. and Shapiro, S. A. (2016). Scaling of seismicity induced by nonlinear fluid-rock interaction after an injection stop. *Journal of Geophysical Research: Solid Earth*, 121(11):8154–8174. doi:10.1002/2016JB012949

Abakumov, I., **Johann, L.**, Shapiro, S. A., Pasternak, E., and Dyskin, A. V. (2020). Towards integrated modeling of deformations, time-lapse seismic changes, and failure stresses caused by massive underground fluid operations. In *SEG Technical Program Expanded Abstracts 2020*.

Johann, L. and Shapiro, S. A. (2020). Large-Scale Migration Patterns of Wastewater-Induced Earthquakes in the Central U.S.. In *EGU General Assembly Conference Abstracts*, volume 22.

Johann, L., Shapiro, S. A., and Dinske, C. (2019). Seismicity in Central Oklahoma shows spatio-temporal signatures of reservoir-induced seismicity. In *EGU General Assembly Conference Abstracts*, volume 21.

- Johann, L.**, Dinske, C., and Shapiro, S. A. (2018). Reservoir-induced seismicity: A review. In *EGU General Assembly Conference Abstracts*, volume 20.
- Johann, L.**, Shapiro, S. A., and Dinske, C. (2018). Seismicity in Central Oklahoma shows signatures of reservoir-induced seismicity. In *AGU Fall Meeting (Washington D.C.)*.
- Johann, L.**, Dinske, C., and Shapiro, S. A. (2017). Linear diffusion of pore-fluid pressure in hydraulically heterogeneous media: An approach to explain spatio-temporal features of fluid-induced seismicity. In *77. Jahrestagung der Deutschen Geophysikalischen Gesellschaft (Potsdam)*.
- Johann, L.**, Dinske, C., and Shapiro, S. A. (2017). Scaling of postinjection-induced seismicity: An approach to assess hydraulic fracturing related processes. In *EGU General Assembly Conference Abstracts*, volume 19.
- Johann, L.**, Dinske, C., and Shapiro, S. A. (2016). Asymptotic scaling of the back front of injection-induced seismicity. In *76. Jahrestagung der Deutschen Geophysikalischen Gesellschaft (Münster)*.
-

Acknowledgements

Danksagung

An erster Stelle gilt mein großer Dank Prof. S. A. Shapiro, der diese Arbeit betreut hat. Umfassende Gespräche, zahlreiche Ideen, inspirierende Diskussionen sowie seine Unterstützung haben maßgeblich zu dieser Arbeit beigetragen.

Vielen Dank Prof. Marco Bohnhoff für die Übernahme des Zweitgutachtens.

Ich bedanke mich bei Carsten, der nicht nur Co-Autor von zwei der hier präsentierten Arbeiten ist, sondern mit dem ich auch einige spannende Dienstreisen erleben durfte.

Danke Jonas, für die gemeinsame Doktorandenzeit, für die Stunden beim Buddeln im GeoGarten und als Kletterpartner.

Einen Dank auch meinen anderen Kollegen; Jörn für die fachlichen Gespräche und für die gemeinsamen Espressopausen, Nepomuk für unsere Lehrprojekte und die Leidenschaft für Bruno, Aurelian als langjähriger Büronachbar, die gemeinsamen Lehrerfahrungen und als PHASE-Planungspartner. Und natürlich Stine, Nastasja, Slava, Cornelius, Henry und Wasja, die meine Zeit in Lankwitz begleitet haben.

Ich danke meinen Freunden; insbesondere Eva, Margherita, Anja, Maria und den Utrechtern. Ihr habt mich die letzten Jahre abgelenkt, mir Glücksmomente geschenkt und mein Leben bereichert.

Einen ganz besonderen Dank an meine Eltern und an meine Familie; in Deutschland und in den Niederlanden. Danke für Eure Unterstützung bei meinen Vorhaben und Ideen. Ihr seid wundervoll.

Und zuletzt danke ich Rens. Für die Zeit in Lankwitz und für unsere Abenteuer; in der Natur, in den Bergen und am Kletterseil. Danke für Deine Unterstützung, Dein unermüdliches Zuhörvermögen, Deine Inspiration und Deine Wertschätzung. Ich freue mich auf unsere Zukunft.

